

AFRL-IF-RS-TR-2006-317
Final Technical Report
October 2006



**QUANTITATIVE DEVELOPMENT OF
BIOMOLECULAR DATABASES, MEASUREMENT
METHODOLOGY, AND COMPREHENSIVE
TRANSPORT MODELS FOR BIOANALYTICAL
MICROFLUIDICS**

Leland Stanford Junior University

**Sponsored by
Defense Advanced Research Projects Agency
DARPA Order No. J406**

APPROVED FOR PUBLIC RELEASE; DISTRIBUTION UNLIMITED.

STINFO FINAL REPORT

The views and conclusions contained in this document are those of the authors and should not be interpreted as necessarily representing the official policies, either expressed or implied, of the Defense Advanced Research Projects Agency or the U.S. Government.

**AIR FORCE RESEARCH LABORATORY
INFORMATION DIRECTORATE
ROME RESEARCH SITE
ROME, NEW YORK**

NOTICE AND SIGNATURE PAGE

Using Government drawings, specifications, or other data included in this document for any purpose other than Government procurement does not in any way obligate the U.S. Government. The fact that the Government formulated or supplied the drawings, specifications, or other data does not license the holder or any other person or corporation; or convey any rights or permission to manufacture, use, or sell any patented invention that may relate to them.

This report was cleared for public release by the Air Force Research Laboratory Rome Research Site Public Affairs Office and is available to the general public, including foreign nationals. Copies may be obtained from the Defense Technical Information Center (DTIC) (<http://www.dtic.mil>).

AFRL-IF-RS-TR-2006-317 HAS BEEN REVIEWED AND IS APPROVED FOR PUBLICATION IN ACCORDANCE WITH ASSIGNED DISTRIBUTION STATEMENT.

FOR THE DIRECTOR:

/s/

CLARE D. THIEM
Work Unit Manager

/s/

JAMES A. COLLINS
Deputy Chief, Advanced Computing Division
Information Directorate

This report is published in the interest of scientific and technical information exchange, and its publication does not constitute the Government's approval or disapproval of its ideas or findings.

REPORT DOCUMENTATION PAGE*Form Approved*
OMB No. 0704-0188

Public reporting burden for this collection of information is estimated to average 1 hour per response, including the time for reviewing instructions, searching data sources, gathering and maintaining the data needed, and completing and reviewing the collection of information. Send comments regarding this burden estimate or any other aspect of this collection of information, including suggestions for reducing this burden to Washington Headquarters Service, Directorate for Information Operations and Reports, 1215 Jefferson Davis Highway, Suite 1204, Arlington, VA 22202-4302, and to the Office of Management and Budget, Paperwork Reduction Project (0704-0188) Washington, DC 20503.

PLEASE DO NOT RETURN YOUR FORM TO THE ABOVE ADDRESS.

1. REPORT DATE (DD-MM-YYYY) OCT 06		2. REPORT TYPE Final		3. DATES COVERED (From - To) Sep 00 – Mar 06	
4. TITLE AND SUBTITLE MODELING, ANALYSIS, SIMULATION, AND SYNTHESIS OF BIOMOLECULAR NETWORKS				5a. CONTRACT NUMBER F30602-00-2-0609	
				5b. GRANT NUMBER	
				5c. PROGRAM ELEMENT NUMBER 61101E	
6. AUTHOR(S) Juan G. Santiago, Shankar Sundaram, S. Krishnamoorthy, Andrzej J. Przekwas, Carl Meinhart, David G. Myszka, Antonio Ricco, Travis Boone, Omar Knio, Habib Najm, Bert Debusschere				5d. PROJECT NUMBER E117	
				5e. TASK NUMBER 00	
				5f. WORK UNIT NUMBER 61	
7. PERFORMING ORGANIZATION NAME(S) AND ADDRESS(ES) Leland Stanford Junior University 651 Serra Street Stanford California 94305-6215				8. PERFORMING ORGANIZATION REPORT NUMBER N/A	
9. SPONSORING/MONITORING AGENCY NAME(S) AND ADDRESS(ES) Defense Advanced Research Projects Agency AFRL/IFTC 3701 North Fairfax Drive 525 Brooks Road Arlington Virginia 22203-1714 Rome New York 13441-4505				10. SPONSOR/MONITOR'S ACRONYM(S)	
				11. SPONSORING/MONITORING AGENCY REPORT NUMBER AFRL-IF-RS-TR-2006-317	
12. DISTRIBUTION AVAILABILITY STATEMENT APPROVED FOR PUBLIC RELEASE; DISTRIBUTION UNLIMITED. PA#06-732					
13. SUPPLEMENTARY NOTES					
14. ABSTRACT The goal of this project was the development of novel on-chip assay devices and modeling capabilities to enable optimized design processes and create new methods to realize robust, field-portable microfluidic devices. The team developed, validated and commercialized new multiphysics models to the Bio-electro-mechanical systems (MEMS) community (over 50 organizations) through CFD-ACE+. The team further developed rapid (e.g., 1000x faster) biokinetics data extraction methods for antibody assays; and discovered and created models for an electrokinetic instability and used it to create 1000x faster a micromixer. The team developed a novel on-chip assay device that combines isoelectric focusing and electrophoresis to achieve a 2D assay in 1/30th of the time of a traditional system. Lastly, the team developed a method that achieved 1100x fold on-chip electrophoretic sample pre-concentration which lead to an additional task focused on developing rapid sample pre-concentration methods to improve on-chip assay. The team developed new codes for eletrokinetic convective-diffusion assays with fast reaction kinetics capability. The team experimentally demonstrated million-fold sample concentration increase (three orders of magnitude improvement), using optimized isotachophoresis. .					
15. SUBJECT TERMS Microfluidics, Bio-MEMS, electrokinetics, sample stacking, preconcentration; proteomics, numerical modeling, fluid mechanics, microarrays, micromixing					
16. SECURITY CLASSIFICATION OF:			17. LIMITATION OF ABSTRACT UL	18. NUMBER OF PAGES 156	19a. NAME OF RESPONSIBLE PERSON Clare D. Thiem
a. REPORT U	b. ABSTRACT U	c. THIS PAGE U			19b. TELEPHONE NUMBER (Include area code)

TABLE OF CONTENTS

Executive Summary	1
1.0 Introduction.....	3
2.0 Quantitative Development of Biomolecular Databases, Measurement Methodology, and Comprehensive Transport Models for Bioanalytical Microfluidics	3
3.0 MICROFLUIDIC SYSTEMS FOR HIGH SAMPLE STACKING ASSAYS.....	103
4.0 MODELING OF HIGH SAMPLE STACKING ASSAYS.....	112
5.0 SUMMARY OF PROJECT IMPACT.....	125
6.0 REFERENCES	144

LIST OF FIGURES

Figure 2.1: Coplanar electrode used in the validation study.....	8
Figure 2.2: Comparison of numerical results (lines) with analytical data (circles).....	9
Figure 2.3: Clausius-Mossotti spectrum for a microparticle with $\epsilon_p = 40$, $\epsilon_m = 80$, $\sigma_p = 1$ (S/m) and $\sigma_m = 0.001$ (S/m).....	11
Figure 2.4: Illustration of various forces acting on a particle kept near an array of electrodes in a channel.	11
Figure 2.5: Comparison of analytical and numerical results for the normalized potential, x-component electrical field and DEP forces on a sphere.	13
Figure 2.6: Schematic of numerical treatment of the slip condition on surface.	15
Figure 2.7: Comparison of normalized velocity across the channel and the slip velocity on top channel wall.	16
Figure 2.8: Particle position at various instants in time throughout the first 40 ms of the DEP process.....	18
Figure 2.9: Computed potential, temperature, and velocity field data for the $\phi = 5$ Vrms case....	19
Figure 2.10: A closer view of velocity field near the binding site (same conditions as Figure 2.9).	20
Figure 2.11: Comparison of surface concentration of antigen-antibody for (a) Sshort and (b) long time periods.....	20
Figure 2.12: Illustration of FASS in a microfluidic channel.	22

Figure 2.13: Schematic of single-step stacking device.....	24
Figure 2.14: Comparison of experimental observation and simulation of sample stacking with EOF induced dispersion.....	25
Figure 2.15: Comparison of simulated (dash curves) and experimental results (solid curves) of the normalized concentration at the centerline of the channel.....	26
Figure 2.16: A semi-implicit scheme for Poisson equation coupled with species transport.	29
Figure 2.17: Schematic of the sandwich immunoassay.....	30
Figure 2.18: (a) Static incubation assay with microsphere.....	31
Figure 2.19: Schematic of multi-step microsphere assay demonstration/validation study.....	32
Figure 2.20: (a) Primary antibody binding. (b) Secondary antibody binding.....	32
Figure 2.21: T junction at time = 15 seconds following injection.....	34
Figure 2.22: T junction at time = 15 seconds following injection.....	34
Figure 2.23: T junction at time = 18 seconds following injection.....	34
Figure 2.24: T junction at time = 25 seconds following injection (<i>IL-2 has been washed out of the channel at this time</i>).....	35
Figure 2.25: Analyte concentrations and bead coverages for a flow ratio of 5(An):5(B).	35
Figure 2.26: Analyte concentrations and bead coverage for a flow ratio of 5(An):1(B).....	36
Figure 2.27: Signal (sensorgrams) evolution with time.....	37
Figure 2.28a: Concentration contours of IL2 at time $t = 0$	38
Figure 2.28b: Contours of electric field squared at time $t = 0$	38
Figure 2.29: Location of microspheres shown at different time levels.....	39
Figure 2.30: Developed architecture for surface biokinetics manager.	40
Figure 2.31: Parameter space for training ANN	42
Figure 2.32: Comparison of ACE+ and ANN rate constants, along with the time taken.....	43
Figure 2.33: Illustration of the adjusted flux balance boundary condition accounting for the presence of the dextran layer.	45
Figure 2.34: Change in the coverage curve with the ratio of analyte radius (R_a) to initial vertical cylindrical pore radius (R_p).....	46
Figure 2.35: Illustration of the differing rates of adsorption on various monoclonal antibody systems and surfaces.....	47
Figure 2.36: (a) Flow cell with notch. (b) IL-2 surface concentration in new flow cell.....	48
Figure 2.37: Test device used to measure 2D flow created by an inhomogeneous AC electric field.	54
Figure 2.38: Fluid velocity field measured in the device shown in Figure 2.37.....	54
Figure 2.39: Simulation of electrothermally-driven fluid motion with an applied voltage of 5 V_{rms}	56
Figure 2.40: Numerical simulation of temperature distribution created by Joule heating.....	56
Figure 2.41: Simulation of concentration in a microcavity after 100 sec, subject to binding on the functionalized surface at the wall.....	57
Figure 2.42 : Normalized binding curves for non-enhanced ($0 V_{rms}$) and electrothermally enhanced ($6 V_{rms}$, $12 V_{rms}$) transport.....	59
Figure 2.43 : Velocity field in microchannel showing effect of electrothermal force on channel flow.	60

Figure 2.44: Concentration plots of electrothermally modified channel flow at $t = 5$ sec with applied voltages of (a) $0 V_{\text{rms}}$ and (b) $6 V_{\text{rms}}$.	61
Figure 2.45: Simulation results show binding enhancement factor, Be , increases with increasing Damköhler number Da as in the static case, but decreases with increasing Peclet number, that is, faster pressure-driven flow.	62
Figure 2.46: <u>Left</u> : SEM image showing reactive ion etched silicon master for point-concentrator device (close-up of a channel intersection).	64
Figure 2.47: <u>Left</u> : Separation performance of point concentrator, compared to control chip without this feature, using fluorescein.	65
Figure 2.48: Electroform (left) and molded plastic part (right) from a reactive ion etched silicon master, showing rounded channel corners and point concentrator features.	67
Figure 2.49: Triangular point concentration feature across full photomask line width.	67
Figure 2.50: Scanning electron micrograph (SEM) showing features created with isotropic glass etching techniques.	68
Figure 2.51: Channel and reservoir configuration utilized for point concentrator studies.	72
Figure 2.52: Channel geometry/layout for point-concentrator simulations, showing the $20 \times 31 \mu\text{m}$ triangular asperity used to create local distortion of the electric field during the loading/injection process.	72
Figure 2.53: Comparison of single-species electropherogram using the geometrical configuration shown in Figure 5.3 (“triangle”) with a floating/stacking voltage/timing configuration; the same voltage/timing without the triangular asperity (“float”); and the use of the asperity with the “pinch-and-pullback” configuration.	73
Figure 2.54: <u>Left panel</u> shows CFD-ACE+ simulation of three-dimensional flow, diffusion, and binding reaction within a single flow cell.	74
Figure 2.55: Example data sets for six validated molecular systems.	75
Figure 2.56: <u>Left panel</u> shows kinetic titration data for PSA/mAb interaction.	76
Figure 2.57: Concentration dependent binding profiles for the NIST bivalent Barnase/Barstar system.	77
Figure 2.58: Schematic of the microchannel setup.	80
82	
Figure 2.59: Sample images from the experiment, shown for applied fields of 25,000, 50,000, and 75,000 V/m, corresponding to the first, second, and third column.	82
Figure 2.60: Electrokinetic instability during electrokinetic “pinching” at an X-intersection.	83
85	
Figure 2.61: Contour plot of growth rates (s) versus wave number and Rayleigh number.	85
86	
Figure 2.62: Snapshots of the simulated dye field at various instances in time for different driving electric fields.	86
88	
Figure 2.63: Comparison of growth rates of disturbances as predicted by three models.	88
89	
Figure 2.64: Nonlinear simulation of the depth-averaged equation system.	89
Figure 2.65: Velocity profiles for water flow through a hydrophilic (squares, no-slip) and a hydrophobic (triangles, slip) microchannel.	91

Figure 2.66: Solutions of Eq. (2), showing air gap thickness as a function of plate separation to produce a given slip length.	93
Figure 2.67: Velocity profiles along the microchannel wall. The various profiles show regions of slip and no-slip.	94
Figure 2.68 Separation algorithm for the 2D IEF-CE separation.	95
Figure 2.69: CCD images during species sampling.	96
Figure 2.70: Gel-like plots of an IEF-CE separation at CE analysis times of 3 s, 5 s and 7 s.	97
Figure 2.71: Schematic of FASS/CE protocol.	101
Figure 2.72: Electropherograms of fluorescein and bodipy separation.	102
Figure 3.1: (a) Narrow-channel stacking chip geometry.	103
Figure 3.2: Plot of signal peaks for sample stacking of AlexaFluor analyte.	104
Figure 3.3: Schematic of FASS assay protocol.	105
Figure 3.4: Schematic of ITP/CE assay protocol.	106
Figure 3.5: Isotachophoretic stacking and detection of Alexa Fluor 488.	108
Figure 3.6: Detection of Alexa Fluor 488 at an initial concentration of 100 fM, greater than million-fold concentration increase.	109
Figure 3.7: Detection techniques for capillary electrophoresis (adapted from the CRC Handbook of Capillary Electrophoresis [85], with permission).	110
Figure 4.1: The state and equations used to advance the simulation in time for an RK2 integrator.	117
Figure 4.2: The experimental apparatus, with the portion modeled by the simulation shown in green.	118
Figure 4.3: Titration curve for a 20 mM HEPES buffer.	119
Figure 4.4: Evolution of the Na ⁺ concentration.	120
Figure 4.5: Evolution of the Cl ⁻ concentration.	120
Figure 4.6: Evolution of the total buffer molarity.	121
Figure 4.7: Evolution of the L ⁻ concentration.	121
Figure 4.8: Evolution of the H ⁺ concentration.	121
Figure 4.9: Evolution of the pH.	121
Figure 4.10: Evolution of the conductivity.	122
Figure 4.11: Evolution of the electric field strength.	122
Figure 4.12: Evolution of the dye (D ⁻) concentration.	123
Figure 4.13: Evolution of the field strength.	124
Figure 4.14: Evolution of the dye concentration.	124

LIST OF TABLES

Table 2.1: Physical parameters used in the UCSB TLC Sensor study.	17
Table 2.2: Parameters used in single-step stacking simulation.....	24
Table 2.3: Physical and electrical properties of the medium (DI water) and microspheres (by UCSB)	37
Table 2.4: Binding rate constants determined from SPR analysis of PSA/antibody interactions	48
Table 2.5: Physical phenomena, their models and examples of the application of the models...	50
Table 2.6: Microfluidic card deliveries.....	69
Table 2.7: Injection voltage setup and timing for floating/stacking.	70
Table 2.8: “Pinch-and-pullback” voltage and timing setup.....	70
Table 2.9: Comparison of areas of electrophoretic peaks resulting from pinch-&-pullback and floating/stacking injection and separation of 12 different eTag™ reporters.....	71
Table 2.10: Timing/voltage conditions for floating/stacking operation of channel with triangular asperity in the region of the injector.....	73
Table 2.11: Timing/voltage conditions for pinch-and-pullback operation of channel with triangular asperity in the region of the injector.....	73
Table 2.12: Multi-dimensional system performance comparison.....	99

Executive Summary

The project consisted of an initial three-year effort by Stanford, ACLARA, CFD Research Corp., University of Utah, and the University of California at Santa Barbara; and an additional task by Stanford, Sandia National Labs, and The Johns Hopkins University. The overall effort was led by Stanford University, funded by Dr. Anantha Krishnan of the Defense Advanced Research Projects Agency (DARPA), and monitored by Clare Thiem of the Air Force Research Laboratory (AFRL).

The goal of the first three-years of the project was the development of novel on-chip assay devices and modeling capabilities which will enable optimized design processes and create new methods to realize robust, field-portable microfluidic devices for the detection. First, the team developed, validated and commercialized new multiphysics models to the Bio-Micro-electro-mechanical systems (MEMS) community (over 50 organizations) through CFD-ACE+. These included codes on dielectrophoresis, electrothermal flow, microbead assays, and surface plasmon detection devices for antigen/antibody assays. Second, the team developed rapid, automated biokinetics data extraction methods for antibody assays (including 1000x reduction in time in a Biacore Corp. unit as an example, from days to minutes). Third, the team discovered, formulated, and created models of a new electrokinetic instability. This instability was leveraged in creating a rapid micromixer with 1000x mixing rate over diffusion in a typical simple binding assay. Fourth, the team experimentally quantified and developed slip velocity models for hydrophobic channels. Fifth, the team developed a novel on-chip assay device that combines isoelectric focusing and zone electrophoresis to achieve a 2D assay in 1/30th of the time of a traditional system (and with 10,000x less sample). Lastly, the team developed methods for on-chip sample stacking to improve sensitivity. This effort produced a fast field amplified sample stacking method achieving 1100x increase in concentration in less than 10 sec. The latter effort was so successful that Dr. Anantha Krishnan of DARPA provided funding to extend the project for an additional task to explore sample stacking further.

The additional task focused on developing rapid sample pre-concentration methods to improve the sensitivity of on-chip assays (with a target figure of merit of 10,000 fold increase by project end). The team developed high fidelity, computational codes for full electrokinetic, convective-diffusion assays with multiple species and fast reaction kinetics capability. Experimentally, the team developed stacking methods using field amplified sample stacking, thermal gradient focusing, and isotachophoresis. By project end, the team experimentally demonstrated million-fold sample concentration increase (approximately three orders of magnitude better than the second best ever demonstrated on or off chip). This was accomplished using optimized (and novel control methods for) isotachophoresis. The team demonstrated and were able to inject, stack, separate, and detect analytes with 100 attomolar initial concentrations in less than two minutes, the highest sensitivity ever reported.

The activities of the project can be categorized into the areas of Multiphysics Models for Microfluidic Systems, Novel Electrokinetic Devices and Models, and Sample Preconcentration Devices and Methods for High Sensitivity Assays. The accomplishments are summarized here as follows:

1. Multiphysics Models for Microfluidic Systems: Developments being used by over 50 organizations include:
 - a. Experimentally validated and commercialized tools for coupled convective-diffusion, thermal, concentration and electric fields.
 - b. Models and theory for dielectrophoresis and electrothermal flows.
 - c. Models and theory for sample stacking via field amplified sample stacking and isotachopheresis.
 - d. High-fidelity models for Biacore-type biosensors and bimolecular reactions. These include Biacore sensors, particle-based assays, biokinetics data extraction, and design for faster, more sensitive assays.
2. Novel Electrokinetic Devices and Models Research:
 - a. Discovered and identified a new electrohydrodynamic instability that occurs in the electrokinetic flow regime and can couple with electroosmotic flow.
 - b. Proposed mechanism and model for this electrokinetic instability (EKI) including linear stability analyses and non-linear simulation. Models can predict critical conditions, mixing rate.
 - c. Demonstrated robust micromixing devices based on EKI.
 - d. Demonstrated a novel miniaturized 2D assay combining (for the first time on-chip) isoelectric focusing and capillary electrophoresis. Assay uses 10 ng sample, has 800 peak capacity, and can be performed in ~60 min.
3. Sample Preconcentration Devices and Methods for High Sensitivity Assays Research:
 - a. Developed thermal gradient focusing techniques, demonstrating 10,000-fold stacking and showing dependence of stacking on temperature gradient, electric field, and other critical parameters.
 - b. Developed On-chip capillary electrophoresis (CE) with field amplified sample stacking (FASS). Demonstrated 12,000-fold concentration increase (171x greater than any other on-chip FASS). Can stack and separate in <20 s.
 - c. As an additional task, developed optimized isotachopheresis assays. ---- Demonstrated sample preconcentration of over million-fold in less than 2 min. Demonstrated injection, stacking, and detection of 100 attomolar concentrations—to the knowledge of the team, the highest ever reported sensitivity of any electrophoretic or chromatographic assay.

The project had a very significant impact on the microfluidics, lab-on-a-chip and biosensor communities as a whole. In addition to these technical achievements, the project resulted in over 168 journal and conference papers, three inventions and patents and patent applications, and trained 10 PhD's, three MS graduates, and six postdocs. The work led to six awards from conferences, national organizations, and the US government. In addition, this project funding and, more importantly, the associated technical accomplishments from this project contributed to

the successful promotion to Associate Professor with tenure for two of the co-PIs involved in the effort (Myszka and Santiago). Three of these PhDs and postdocs are now faculty members at major universities and building a career on microfluidics research. Nine others are engineers, researchers, and/or managers concentrating on microfluidics research and development at either companies or national laboratories.

1.0 Introduction

This final technical report describes the major achievements of the multi-year, multi-center, research contract entitled, “Quantitative Development of Biomolecular Databases, Measurement Methodology, and Comprehensive Transport Models for Bioanalytical Microfluidics,” funded by Defense Advanced Research Projects Agency’s (DARPA’s) Simulation of Biological Systems (SIMBIOSYS) Program (Contract No. F30602-00-2-0609). The goal of the first project was the development of novel on-chip assay devices and modeling capabilities to enable optimized design processes and create new methods to realize robust, field-portable microfluidic devices. Naturally this work involved a combination of modeling and simulation, experimentation, and prototyping. Due to success of research in the area of on-chip electrophoretic sample preconcentration an additional task was added to pursue the work further. The body of the report is basically divided into three sections. The first section corresponds roughly to the original project, while the second and third sections describe the experimental and modeling elements of the extension.

2.0 Quantitative Development of Biomolecular Databases, Measurement Methodology, and Comprehensive Transport Models for Bioanalytical Microfluidics

The goal of the original project was the development of novel on-chip assay devices and modeling capabilities which could enable optimized design processes and create new methods to realize robust, field-portable microfluidic devices for a variety of applications. The project incorporated an interactive approach that leveraged experiments, simulation, and fabrication so that each step of the experiment data acquisition, flow experiment interrogations, and ligand-receptor/flow characterization were modeled in detail as the data was obtained. The goal of the project was successfully accomplished over the course of the project, with devices being developed across a wide range of applications and modeling tools developed for CFD-ACE+ to both model device performance and provide guidance for future design and development. This section briefly reviews some of the project team’s accomplishments in this area.

2.1 Development of Multiphysics Models (CFD Research Corporation, U. of Utah, UCSB, Stanford)

The role of CFD Research Corporation (CFDRC) was to provide tools to model the new devices and techniques developed by the experimental investigators. CFDRC's involvement in the effort would also provide a means to transition new tools and newly found physics resulting from this project to a broad range of researchers and device designers when incorporated into their CFD-ACE+ modeling software tools. CFDRC developed models to simulate dielectrophoresis (DEP) and electrothermal flow. Both of these models have been used extensively in the design and development of tunable laser cavity (TLC) sensor (in collaboration with UCSB), design of sample stacking system (Stanford) and design of microfluidic devices by ACLARA. The summary of the models developed and their validation are reported below.

2.1.1 Simulation of Electrothermal flow (CFDRC and UCSB)

Use of microfluidic devices in biological sample preparation and assays has received increasing attention in recent years. These devices often rely on the fast and thorough mixing of different analytes in a buffer medium. Normally, diffusion is the mechanism through which uniform concentrations are achieved. Although the typical characteristic length scale associated with microfluidic devices is small, diffusion alone cannot provide adequate mixing because of inappropriate device dimensions, operational times, and complex mixing protocols. To reduce the diffusion length scale, external forcing is required to induce repeated stretching and folding of the material interface[2] leading to both short-term and long-term chaotic behavior. In large-scale fluid dynamic systems, turbulence plays a critical role in facilitating mixing. In microfluidic devices, however, small feature size and lack of nonlinearity make use of turbulence impossible. To introduce nonlinearities in the flow, passive and active means of introducing forcing functions have been reported in the literature. For example, rapid changes in flow directions through use of tortuous flow paths[3] or grooved surfaces [4] has been tried to reduce diffusion distances. Stroock, et. al.[5], Ajdari[6], and Johnson, et. al.[7], have demonstrated a circulating cellular flow generated via inhomogeneous surface charge as a means to facilitate the mixing process using Electroosmosis. Oddy, et. al.[8] used conductivity gradients in the bulk fluid as a method to induce chaos and mixing when an alternating electric field is applied. Magnetic fields [9] have also been used to facilitate mixing. Other active means include use of bubbles (thermally actuated [10] and more recently gaseous slugs [11]) and acoustic stirring[12]. Recently it has been shown that use of a motile bacterium can enhance mixing in microfluidic flow[13]. A comprehensive review of mixing in microfluidic devices can be found in reference [14].

When an AC electric field is applied to an electrolyte solution, several modes of AC electrokinetic phenomena can occur, all of which primarily depend on the applied voltage and frequency. When the applied voltage is low and the frequency is sufficiently high, electrothermal flow dominates the electrolysis and AC electroosmosis[15]. Ramos et. al.[16]

formulated and discussed in detail the electrothermal flow induced in the proximity of an electrode that is under the influence of the AC electric field. When it is applied to an electrolyte solution, the solution is subjected to coulombic and dielectric forces due to variations in the dielectric properties (electrical permittivity and conductivity) as a function of temperature. Though joule effect is often the primary mechanism for heating the solution, other external sources, such as laser illumination, can induce thermal gradients, and hence, electrothermal flows. Electrothermally induced flow depends on a variety of parameters such as electrical conductivity and permittivity, the voltage and frequency of the applied electric field, and electrode configuration and channel dimensions.

Mathematical formulation

Let's consider a microfluidic channel consisting of a pair of co-planar electrodes or electrode arrays kept at the bottom floor of the channel as shown in Figure 2.1. The electrodes have a width of d_2 and a gap of $2d_1$ between adjacent electrodes. They are energized by an electric potential of $-V_0$ and V_0 , respectively. The force density due to application of the electric field is given by[17]:

$$\mathbf{f} = \rho_q \mathbf{E} - \frac{1}{2} \mathbf{E}^2 \nabla \varepsilon + \frac{1}{2} \nabla \left[\rho_m \left(\frac{\partial \varepsilon}{\partial \rho_m} \right)_T \mathbf{E}^2 \right] \quad (2.1)$$

Where ρ_e is the charge density, \mathbf{E} is the electric field, ε is the permittivity of the buffer, and ρ_m is the buffer density. The first, second, and third terms on the right side of the above equation represents the Coulomb force, the dielectrophoretic force, and the electrostriction force, respectively. If the applied electric field is an alternating one, then the averaged force density can be expressed as[16]:

$$\langle \mathbf{f} \rangle = \frac{1}{2} \text{Re} \left[\frac{\sigma \varepsilon (\alpha - \beta)}{\sigma + i\omega \varepsilon} (\nabla T \cdot \mathbf{E}_0) \mathbf{E}_0^* - \frac{1}{2} \varepsilon \alpha |\mathbf{E}_0|^2 \nabla T \right] \quad (2.2)$$

Linear variations of the electric properties are assumed in deriving the above equation. In Equation 2, σ is electrical conductivity, T is the temperature, and α and β are the coefficients of variations of the electrical properties with respect to the temperature. The coefficients α and β are expressed as:

$$\alpha = \frac{1}{\varepsilon} \frac{\partial \varepsilon}{\partial T}, \quad \beta = \frac{1}{\sigma} \frac{\partial \sigma}{\partial T} \quad (2.3)$$

This report focuses only on joule heating ($j = \sigma \mathbf{E}^2$) as a source of introducing thermal gradients. The conservation equation for thermal field is expressed as:

$$\rho_m c_p \frac{\partial T}{\partial t} + \rho_m c_p (\mathbf{u} \cdot \nabla) T = k \nabla^2 T + \sigma \mathbf{E}^2 \quad (2.4)$$

Where c_p is the specific heat capacity, \mathbf{u} is the velocity vector, and k is the thermal conductivity. The fluid flow is governed by Navier-Stokes and continuity equations:

$$\rho_m \left[\frac{\partial \mathbf{u}}{\partial t} + (\mathbf{u} \cdot \nabla) \mathbf{u} \right] = -\nabla p + \mu \nabla^2 \mathbf{u} + \langle \mathbf{f} \rangle \quad (2.5)$$

$$\nabla \cdot \mathbf{u} = 0$$

Where p is pressure and $\langle \mathbf{f} \rangle$ is the momentum source induced due to the electrothermal flow. The electric field satisfies the following relations:

$$\mathbf{E} = -\nabla V, \frac{\partial \rho_e}{\partial t} + \nabla \cdot \mathbf{j} = 0 \quad (2.6)$$

$$\nabla \cdot \mathbf{D} = 0, \mathbf{D} = \varepsilon \mathbf{E}, \mathbf{j} = \sigma \mathbf{E}$$

Where v is the electric potential, \mathbf{j} is the current density, \mathbf{D} is the displacement vector, and σ is the electrical conductivity of the buffer. The solution to the coupled Equations (4) through (6), subjected to appropriate boundary conditions, describe the thermal, electric, and flow fields. Two modeling approaches are used to characterize the mixing of analytes in microfluidic devices. When the size of the analyte is very small (sub-micron) and the inertial acceleration relative to the fluid can be neglected, a continuum-based advection/diffusion equation for the analyte concentration is solved. When the analyte molecules are larger (micron-sized) and the inertial acceleration is important, a kinematic equation describes the motion of the particles[2]

Exact solution

Equations (2.4) through (2.6) are coupled, non-linear, PDEs that usually preclude analytical solution. However, this description follows the procedure used by Ramos, et. al. [16], and rewrites the equations for low Reynolds number ($\ll 1$) steady-state flow commonly seen in microfluidic devices. The resulting linear equations admit an analytical solution for simplified geometries. In this section, the analytical solutions for a co-planar electrode structure as shown in Figure 2.1 are briefly presented. The normalized electric potential ϕ (normalized by V_0) distribution is given by the Fourier integral:

$$\phi(x, y) = \int_0^\infty A(\lambda) \lambda^{-1} e^{-\lambda y} \sin(\lambda x) d\lambda \quad (2.7)$$

where,

$$A(\lambda) = \frac{2}{K(a/b)} \sum_{n=1}^{\infty} (-1)^{n-1} P_{n-1}(\cos v) J_{2n-1}(\lambda b) \quad (2.8)$$

and

$$v = 2 \cos^{-1} a/b, a = d_1, b = d_1 + d_2 \quad (2.9)$$

Here P_n and J_n are the Legendre and Bessel functions of order n , K is the complete elliptic function of the second kind. The general solution to temperature is expressed as:

$$T = -\frac{\sigma\phi^2}{2k} + Ax + By + C \quad (2.10)$$

where A , B , and C are constants determined from thermal boundary conditions. By assuming an isothermal condition on the electrode surface, and solving heat conduction equation, it becomes:

$$T = T_0 - \frac{\sigma V_0^2 \phi^2}{2k} \quad (2.11)$$

The solution for the electrothermal force is calculated from the Equation (2.2) by the Green's function method

$$u_i(x, y) = \iint_{S_0} G_{ij}(x_1, x_2, x_{0,1}, y_{0,2}) f_j(x_{0,1}, y_{0,2}) dS_0 \quad (2.12)$$

Where G_{ij} is green's function or Stokeslet in the presence of a planar boundary. The above methodology can be extend to a periodic array of electrodes and calculate the electric potential in terms of Fourier series:

$$\phi(x, y) = \sum_{n=1}^{\infty} \frac{A_n}{\lambda_n} \cos \lambda_n e^{-\lambda_n y}, \lambda_n = n - \frac{1}{2} \quad (2.13)$$

Where,

$$A_n = \frac{P_{n-1}(\cos c)}{K(\cos \frac{c}{2})} \quad (2.14)$$

Similarly, the flow field is calculated by (2.12) in which the two-dimensional singly periodic Stokeslet in the presence of a planar boundary. The above analytical solutions are used to validate the numerical method.

Numerical method

Microfluidic devices usually have complex electrode patterns, which renders use of the analytical solutions derived based on the linearization assumption invalid. In this scenario, the full-set of governing equations needs to be solved using numerical methods. A finite-volume method-based solver available in the commercial software CFD-ACE+[18] is used to solve the Equations (2.4) through (2.6) in a coupled manner. Analyte mixing is studied using an advection-diffusion equation or kinematic equations. The basic flow, electric, and thermal solvers are available in CFD-ACE+. The source term to the momentum equations corresponding to the electrothermal flow has been added. The numerical method has been validated with the help of the analytical solution described in the previous section.

Model validation

A schematic of the co-planar electrode array design is shown in Figure 2.1. Analytical solutions of this configuration were used to validate the full-scale numerical simulation. The electrode width and the gap used in the study are $50\mu\text{m}$. A DC signal of $\pm 2\text{V}$ is applied to the adjacent electrodes. The ambient temperature is assumed to be 300K . In all the simulations, the KCl solution is used as the buffer. It has a density of 1000 kg/m^3 , viscosity of $10^{-6}\text{ m}^2/\text{s}$, thermal conductivity of 0.6 W/m-K , heat capacity of 4100 J/kg-K , electrical conductivity of $0.056/\text{Ohm-m}$, relative permittivity of 78 , α value of $-0.004/\text{K}$ and β value of $0.02/\text{K}$. Comparison between numerical and analytical solution in terms of velocity and temperature along a plane at an elevation of $5\mu\text{m}$ and $25\mu\text{m}$ from electrode surface is shown in Figure 2.2. In numerical simulation, the grid used is 400 by 200 , and further increase of grid numbers does not improve the results. The numerical and analytical results agree with the error less than 0.1% . A pair of circulating vortices is observed very close to the electrode edges. The maximum velocity in this region is approximately $4\mu\text{m/s}$. The maximum temperature difference is very small (0.2 K).

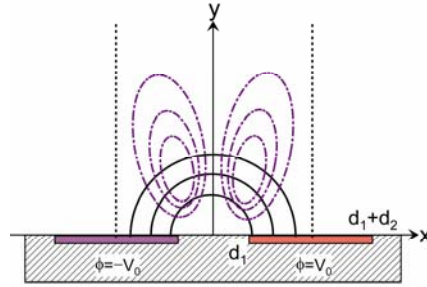


Figure 2.1: Coplanar electrode used in the validation study.

Solid lines illustrate electric field; dashed lines illustrate streamlines.

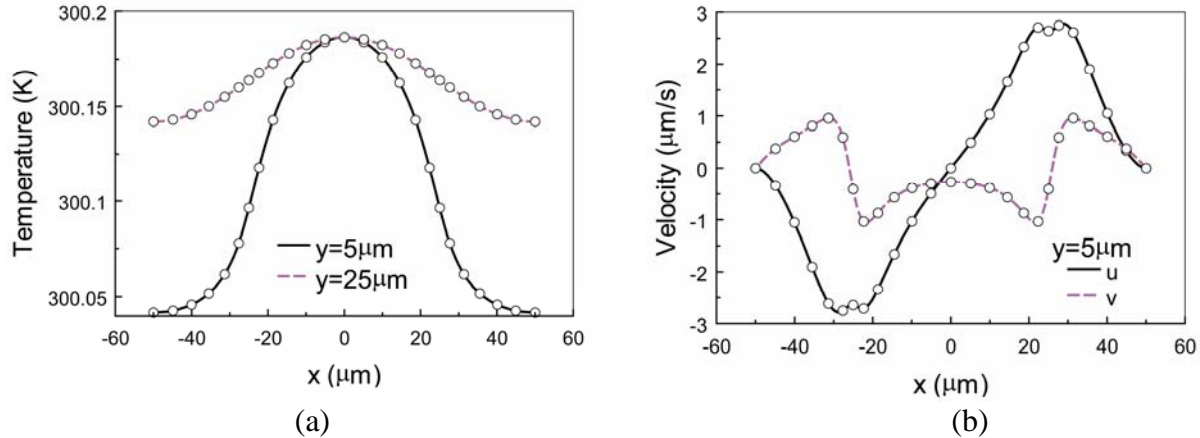


Figure 2.2: Comparison of numerical results (lines) with analytical data (circles).

(a) Temperature field over electrode design of Figure 2.1. (b) Velocity field in the same region.

2.1.2 Model for Dielectrophoresis

The team has accomplished following in this task:

- Models to simulate conventional and traveling wave DEP have been implemented. For this purpose, effective complex permittivity has been used.
- The “electrical module” in CFD-ACE+ has been enhanced to predict high frequency AC electrical fields accurately.
- The module was first tested and validated by comparing numerical solution with analytical results for a simple DEP configuration. Following this, simulations of UCSB Tunable Laser Sensor was performed for design optimization studies.

DEP phenomenon, in contrast to electrophoresis of charged particles in electric field, describes the motion of polarizable particles under the influence of a non-uniform electric field [19]. It varies significantly with applied electric potential and frequency, as well as dielectrical properties of the particles/cells and the medium. Under the action of an externally imposed AC electric field, the in-phase component of the dipole moment induces conventional DEP (c-DEP) forces while the out-of-phase component induces traveling-wave DEP (tw-DEP) forces [20, 21]. The c-DEP and tw-DEP microchips show great potential for characterizing and sorting cells and microorganisms [22-24]. Standard microfabrication techniques and materials are used in fabrication of DEP devices. Compared with electrophoretic (or electroosmotic) separation systems, DEP devices operate using low voltage AC rather than high direct current (DC) voltage.

Furthermore, DEP devices can be integrated with other microfluidic components to provide an efficient, rapid, and automatic analysis system.

Design of DEP devices poses several challenges because DEP forces are a complex function of applied electric field and dielectric properties of the buffer and particles. The study of electric fields generated by the electrode structure becomes essential, particularly in guiding the design of microelectrode array. Existing analytical and numerical models focused on establishing the significance of microelectrode on the equilibrium position and transient motion of particle mixture under various experimental conditions. They illustrate spatial variations of DEP forces within a device, but are limited to specific geometries or approximate boundary conditions [25, 26]. As the complexity of the devices increases, practical applications of these models are limited to predicting levitation height, particle velocity, and selected particle trajectories [27]. On the other hand, high fidelity simulations provide deeper insight into various competing forces and facilitate the selection of optimal geometry and process parameters for maximum performance.

For thorough elaboration of DEP theory, see Pohl [19]; this section offers a necessarily brief account of theoretical fundamentals relevant in the context of this work. The particles or cells experience DEP force from the non-uniform electric field arising due to geometry or electric field non-uniformity. The DEP force can be derived by either the effective dipole moment method or the Maxwell stress tensor method. In general, the time-averaged DEP force for a spherical particle in AC electric field is given as follows [28]:

$$f = \frac{1}{2} (m \cdot \nabla) \mathbf{E} \quad (2.15)$$

where m is the dipole moment and \mathbf{E} is the electric field. For an isotropic, homogeneous dielectric spherical particle, the DEP force in general is expressed as [29]:

$$\bar{f}_{\text{DEP}} = 2\pi a^3 \varepsilon_m \varepsilon_0 \left[0.5 \text{Re}(K) \nabla (E_{x_0}^2 + E_{y_0}^2 + E_{z_0}^2) + \text{Im}(K) (E_{x_0}^2 \nabla \varphi_x + E_{y_0}^2 \nabla \varphi_y + E_{z_0}^2 \nabla \varphi_z) \right] \quad (2.16)$$

where a is the radius of the particle, ε is the permittivity; subscript m represents the media, ε_0 is the permittivity of free space, $(E_{x_0}, E_{y_0}, E_{z_0})$ and $(\varphi_x, \varphi_y, \varphi_z)$ are the magnitudes and phases of x , y , and z components of the electric field; ∇ is the gradient operator; and K is Clausius-Mossotti factor. Equation (2.16) shows two terms to the DEP force vector: a real part related to the in-phase component of the induced dipole moment and an imaginary part related to the out-of-phase component. The in-phase component directs the particles to the regions of electric field maxima ($\text{Re}(K) > 0$) or minima ($\text{Re}(K) < 0$). The motion of the particles due to this component is termed conventional DEP (c-DEP). The out-of-phase component directs the particles to the regions where the phases of the field component are larger ($\text{Im}(K) > 0$) or smaller ($\text{Im}(K) < 0$). The linear motion of the particles due to this component is termed traveling-wave DEP (tw-DEP). The Clausius-Mossotti factor (K) is expressed as:

$$K(\omega) = \frac{\epsilon_p^* - \epsilon_m^*}{\epsilon_p^* + 2\epsilon_m^*} \quad (2.17)$$

where $\epsilon^* = \epsilon - i\sigma/\omega$, is the complex permittivity; $i = \sqrt{-1}$, σ is the conductivity, and ω is the angular frequency of the applied field. A typical Clausius-Mossotti spectrum for a microbead suspended in an aqueous buffer with $\epsilon_p = 40$, $\epsilon_m = 80$, $\sigma_p = 1$ (S/m) and $\sigma_m = 0.001$ (S/m) is shown in Figure 2.3. At low frequencies, these beads are generally more polarizable than the suspending medium and experience positive c-DEP. As the electric field frequency increases, the c-DEP force acting on the particles changes from positive to negative. At the crossover frequency, when the real part of Clausius-Mossotti factor is zero, beads experience no DEP force. This frequency critically depends on the dielectric properties of the particle and the medium. The c-DEP force has two components: a normal component that levitates (attracts) the particle in a direction normal to the electrode surfaces and a horizontal component that pushes (pulls) the particle away from (toward) electrodes. Both components of c-DEP forces decrease significantly as particles move away from the electrode. On the other hand, the tw-DEP spectrum exhibits a unique behavior. The imaginary part vanishes at small and high values of frequencies. For a given particle-buffer pair, the imaginary part is maximum only at one critical frequency. In the case of biological cells, one may assume cell as an ohmic spherical particle and neglect the trans-membrane conductance and surface conductivity. This assumption is particularly good for mammalian cells that do not have a cell wall and have a membrane thickness at least three orders of magnitude smaller than the cell radius.

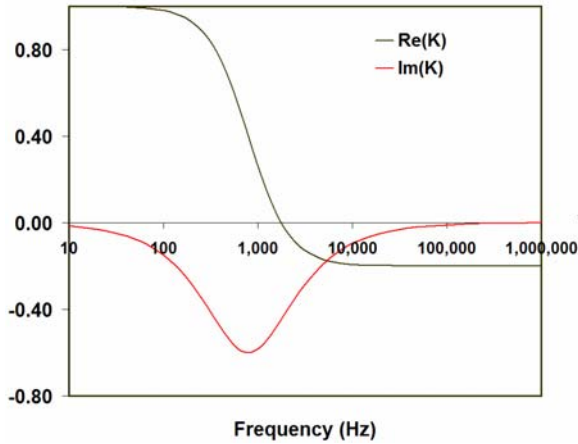


Figure 2.3: Clausius-Mossotti spectrum for a microparticle with $\epsilon_p = 40$, $\epsilon_m = 80$, $\sigma_p = 1$ (S/m) and $\sigma_m = 0.001$ (S/m).

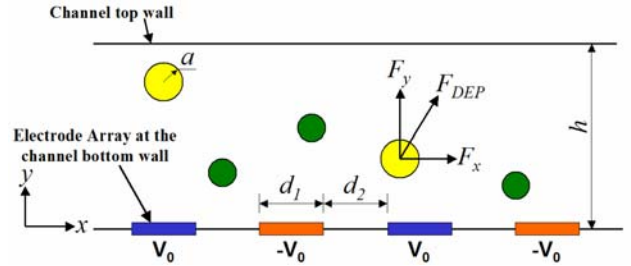


Figure 2.4: Illustration of various forces acting on a particle kept near an array of electrodes in a channel.

Comparison of Force Calculation with Analytical Solution in an Interdigitated Electrode Structure

Figure 2.4 illustrates various forces acting on a particle in a microchannel device. The channel has an array of interdigitated electrodes at the bottom. An AC electric field is applied with 180 degrees shifted in phase between consecutive electrodes. The polarizable particles levitate above the electrode under a negative DEP force F_y . This force is balanced by a gravitational force F_g , which, for a spherical particle of radius a , is $F_g = 3/4 \pi a^3 \Delta \rho g$, where $\Delta \rho$ is the difference between the density of the particle and the suspending solution, and g is the gravitational acceleration. In a traveling electric field, the levitated particles can also move horizontally along the electrode array. Particles of different polarizability move along the electrode with different velocities. Under steady-state conditions, this force is balanced by Stokes drag: $F_{Stoke} = 6\pi\eta a v$, so that $F_x + F_{Stoke} = 0$ where v is the traveling wave velocity and η is the viscosity of the suspending medium. Simulation of dynamic motion of a particle involves balancing these forces and computing the location of the particle. The channel height is sufficiently large when compared to electrode width and spacing, so that the boundary condition at infinity is used at the top channel wall. The peak-to-peak potential is $2V_0$. An assumption is that the thermal conductivity of the metal electrode is much larger than that of the fluid so that the temperature deviates very little from the electrode temperature T_s . The temperature deviation in the fluid due to heating of electrical current is of interest. Both electrical and thermal field are analytically solved and the detailed are published elsewhere[27].

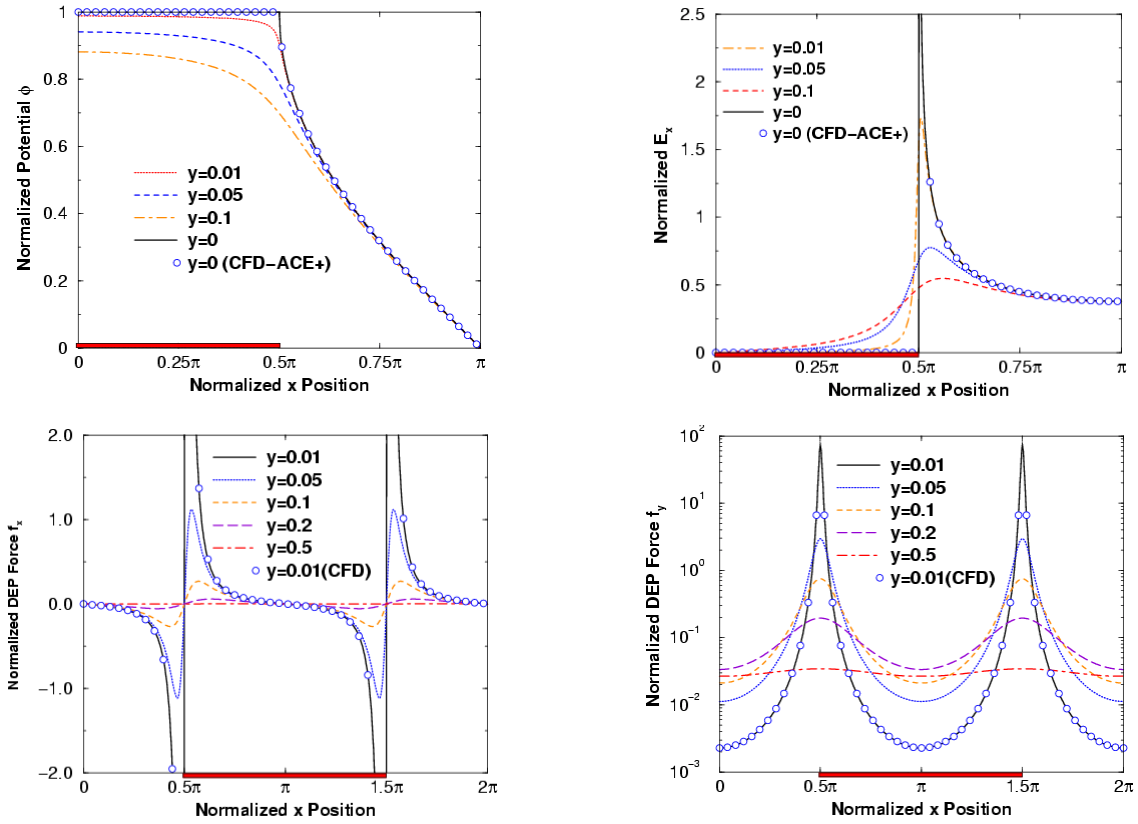


Figure 2.5: Comparison of analytical and numerical results for the normalized potential, x-component electrical field and DEP forces on a sphere.

Figure 2.5 shows comparison of analytical and CFD-ACE+ (numerical) results and they agree very well. It is also observed that the CFD-ACE+ is able to capture the singular behavior of the electrical field and the DEP force near the electrode edge, where they usually tend to go to infinity. The simulation also predicted the levitation force f_y to be symmetric while the lateral force f_x to be anti-symmetric, with respect to the edge and the center of the electrode when the electrode width is equal to that of the spacing. This behavior has not been predicted by approximate solutions reported earlier by other investigators.

2.1.3 Model and Investigation of Slip Condition on Hydrophobic Surface

Nano-bubbles have recently been observed experimentally on smooth hydrophobic surfaces, cracks on a surface can likewise be the site of bubbles when partially wetting fluids are used. Because these bubbles may provide reduced stress boundary condition and modify considerably the friction generated by the solid boundary, it is of interest to quantify their influence on fluid

flows over these slip boundaries. This nano-bubble theory has recently been adopted to interpret experiments of flow over a hydrophobic channel [30].

A schematic of the numerical treatment of the slip problem is shown in Figure 2.6. Because of the flow surface interaction, Stokes slip boundary condition is used to replace the traditional no-slip condition on the surface modified walls, particularly for flow in micro-sized channels [31].

$$\mathbf{u}_s^r = \lambda \frac{d\mathbf{u}_\tau^r}{dn} \quad (2.18)$$

Here the coefficient λ is termed as slip length. Normal to the surface, the non-penetration condition still applies, i.e.

$$\mathbf{u}_n^i = 0 \quad (2.19)$$

Boundary conditions can be converted into a discrete form at the boundary cell center by finite difference. Writing \mathbf{n} as the normal vector, τ_1 and τ_2 as two principal tangential vectors on the surface, the two components of slip condition becomes:

$$\begin{aligned} \mathbf{u}_s^r \cdot \tau_1 &= \lambda \frac{\mathbf{u}_c^i - \mathbf{u}_w^i}{\delta} \cdot \tau_1 \\ \mathbf{u}_s^r \cdot \tau_2 &= \lambda \frac{\mathbf{u}_c^r - \mathbf{u}_w^r}{\delta} \cdot \tau_2 \end{aligned} \quad (2.20)$$

where the subscript c represents for cell center and w for wall. These equations along with

$$\mathbf{u}_w^i \cdot \mathbf{n} = 0 \quad (2.21)$$

determine the wall velocity components in terms of those at the cell center.

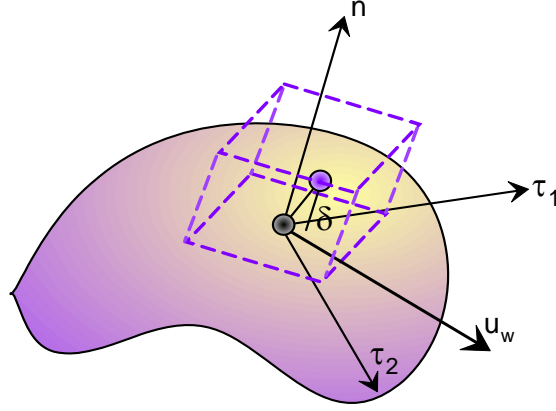


Figure 2.6: Schematic of numerical treatment of the slip condition on surface.

For 2D flow, the relation is:

$$u_w = \frac{-\lambda n_y (-n_y u_c + n_x v_c)}{\lambda + \delta}, \quad v_w = \frac{\lambda n_x (-n_y u_c + n_x v_c)}{\lambda + \delta} \quad (2.22)$$

Validation Case:

A simple channel flow is considered, in which slip occurs on top of the channel wall. This problem admits analytic solution:

$$u = -\frac{1}{2\mu} \frac{dp}{dx} \left[\frac{h+2\lambda}{h+\lambda} hy - y^2 \right] \quad (2.23)$$

Simulation results of dimensionless velocity distribution agree excellently with analytic solution. The slip velocity on the top wall is given by:

$$u_s = -\frac{h^2}{2\mu} \frac{dp}{dx} \left[\frac{\lambda}{h+\lambda} \right] \quad (2.24)$$

For small slip length, the linear and quadratic approximation gives:

$$u_s = -\frac{\lambda h}{2\mu} \frac{dp}{dx}, \quad u_s = -\frac{\lambda h}{2\mu} \frac{dp}{dx} \left[1 - \frac{\lambda}{h} \right] \quad (2.25)$$

These results are plotted in Figure 2.7.

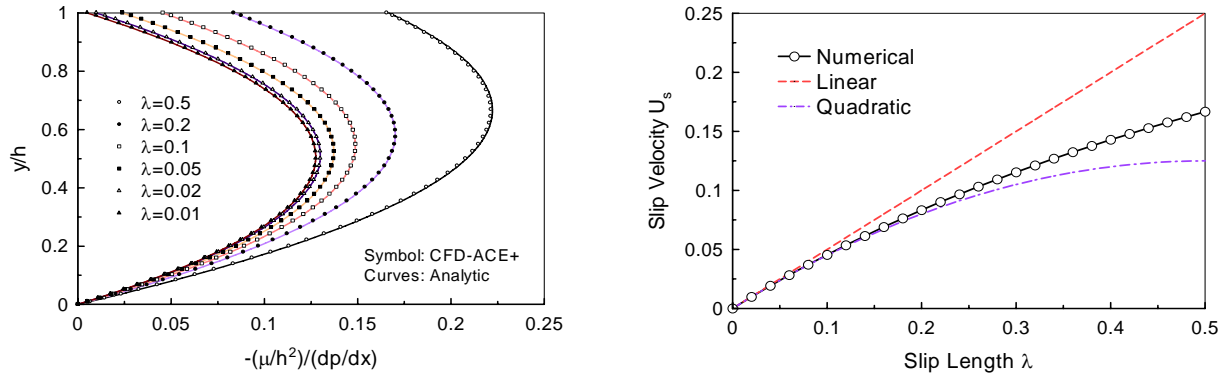


Figure 2.7: Comparison of normalized velocity across the channel and the slip velocity on top channel wall.

2.1.4 Simulation of Tunable Laser Cavity Sensor (CFDRC and UCSB)

Problem Description

Immunoassays, which rely on specific antigen-antibody binding for identification of proteins in a sample, have applications in both clinical laboratories for medical diagnostics and treatment monitoring, and in research laboratories for highly multiplexed testing, such as for biomarker identification. In these cases, throughput is a key consideration. One factor limiting throughput is diffusion of analyte to the reporter. An incubation step of minutes to hours allows diffusion-limited binding to reach detectable levels. These tests are usually performed at centralized labs where high throughput is achieved through robotics and highly parallel assays. However, if the assay could be moved from the centralized lab to the point of care – realizing immunoassay-based diagnostics “on demand” – the test must be faster, as well as smaller, while maintaining high sensitivity.

In response to this need, Microfluidic assays for diagnostics have developed dramatically in recent years, allowing the realization of the lab-on-a-chip concepts for point-of-care diagnosis and high throughput screening for molecular diagnostics. The tunable laser cavity (TLC) sensor, being developed at UC Santa Barbara, uses a semiconductor laser coated with a layer of capture antibodies to detect the presence of antigen in the flow. When the antigen antibody complex is formed, the laser frequency changes with respect to the reference frequency. In order to enhance the sensitivity of the sensor, it is desired to increase the concentration of antigen near the binding site where antibody is coated. In this regard, CFDRC modeled UCSB system to understand the effect of DEP and electrothermal forces on the assay performance.

This report presents the simulation results using DEP model. The simulation parameters are listed below. In the first set of simulation, velocity field and particle trajectories are computed for an idealized system that consists of an expansion-contraction nozzle. A peak-to-peak voltage of 20 volts at the frequency of 10kHz is applied. Other parameters are listed in Table 2.1. The team randomly injects hundred particles close to the throat of the channel and solve for their location as time evolves. The induced fluid flow is calculated by solving the Navier-Stokes equation.

Table 2.1: Physical parameters used in the UCSB TLC Sensor study.

ρ_s	a	μ	σ_m	σ_p	α_0	ϵ_m	ϵ_p
1000	1.5E-6	1E-3	0.056	1E-18	$\pi/8$	80	2.61

Results for particle configuration at four different time instants are shown in Figure 2.8. The induced flow pattern is also shown. Since the particle conductivity is smaller than that of the media, the DEP force alone will drive particles to regions of smaller electrical field (negative DEP), as indicated in Figure 2.8. The magnitude of fluid flow is about 50 $\mu\text{m/s}$.

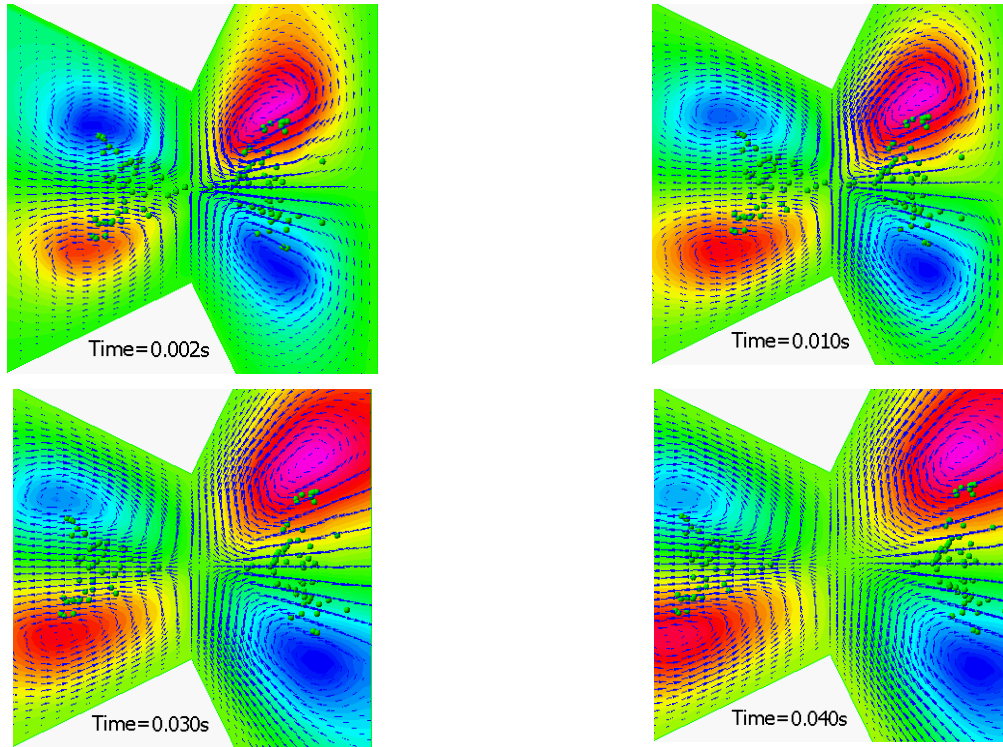


Figure 2.8: Particle position at various instants in time throughout the first 40 ms of the DEP process.

The maximum velocity is approximately $50 \mu\text{m/s}$.

These results have been validated by UCSB whose Particle Image Velocimetry (PIV) measurements predicted a fluid velocity of approximately $60 \mu\text{m/s}$ (However, it was pointed out that the numerical simulation of by UCSB computed a fluid velocity of $70 \mu\text{m/s}$ if electrothermal effects were included, and hence the velocity due to particle dielectrophoresis was therefore estimated as $10 \mu\text{m/s}$ [2]). In literature, similar experiment by Prof Green's group (2000), calculated that the electrothermal effects due to light illumination, resulted in velocities of approximately $10 \mu\text{m/s}$. Because the variation in the estimated velocities was significant, it was decided that the team include models for electrothermal effect in the simulation and this is explained in the next section.

2.1.5 Analysis and Modeling of UCSB System for Electrothermal Flow Effects

This section presents the results from the electrothermal flow simulations in Figure 2.9, where the electric potential and temperature distributions and the velocity vector have been plotted. The AC frequency of 10^5 Hz and the RMS voltage of 5V , which corresponds to a 7.07 V peak voltage, were used in the simulation.

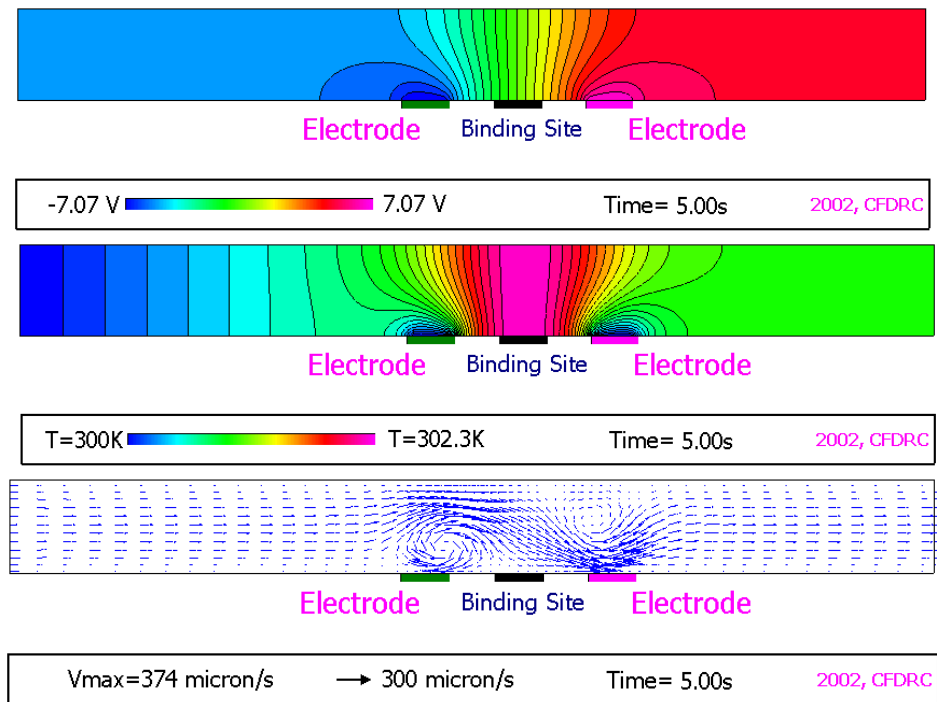


Figure 2.9: Computed potential, temperature, and velocity field data for the $\phi = 5$ V_{rms} case.

The velocity and electric field of the electrothermal flow result in increased binding rate.

It is noted that the velocity field near the electrodes is diverted toward the binding site where the antibody is coated. As a result, enhanced surface binding occurs when compared to (cross-stream) diffusion driven binding in a static/uni-direction flow environment. A closer view of the velocity field is shown in Figure 2.10 to illustrate the bending of the streamlines. Since the channel flow is superimposed on the electrothermal flow, the team recommended that the binding site may be moved the downstream where flow convection was more pronounced (thereby reducing mass transport limitations).

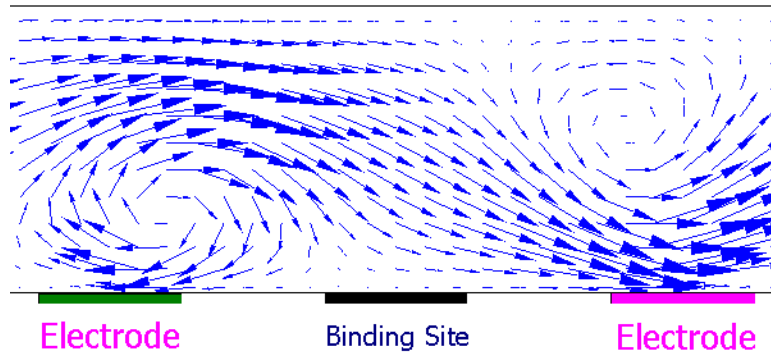


Figure 2.10: A closer view of velocity field near the binding site (same conditions as Figure 2.9).

The time evolution of surface concentration of antigen-antibody complex is plotted in Figure 2.11 and compared to the case where no electrothermal flow is involved. For small periods, the increase of surface concentration is very significant. The electrothermal flow enhances binding significantly. For example, the time required to achieve 90% of maximum surface concentration in the presence of electrothermal flow is 25% shorter than that without electrothermal flow.

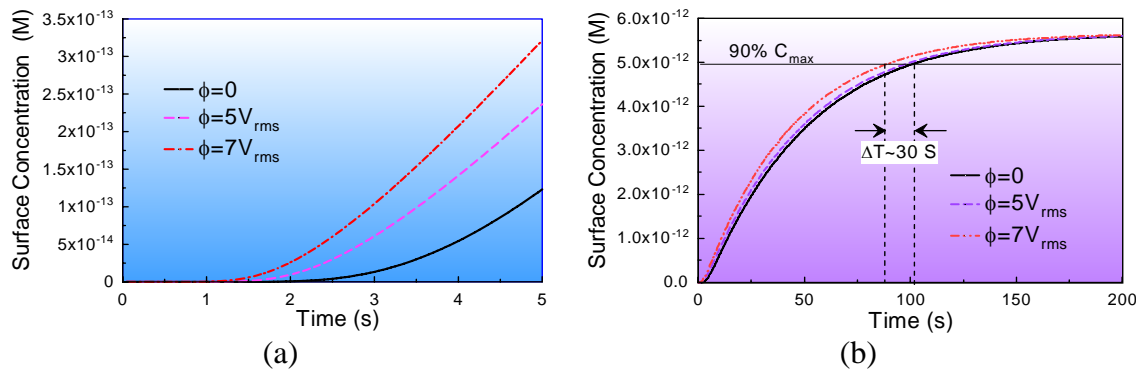


Figure 2.11: Comparison of surface concentration of antigen-antibody for (a) short and (b) long time periods.

The surface concentration of antibody is $1.7E-3$ nM/cm.

Figure 2.11 shows the concentration contour of the antigen in the channel. Note that the antigen flows toward the binding site because of the electrothermal effect. This is in sharp contrast to how the antigen is transported in the case when there is no electrothermal flow. The local mixing enhancement helps to eliminate mass transport limitations leading to increased surface coverage. The higher the electrical potential is, the more pronounced is the surface binding.

From the numerical simulation studies, the team concluded that the electrothermal flow is more effective in enhancing surface binding in a TLC sensor. The net effect is reduced detection time. By increasing the applied voltage, it is possible to accelerate the binding further. The current simulations clearly indicate that the DEP forces are not significant in this sensor due to the size of the antigen molecules.

2.1.6 Simulation of Field Amplified Sample Stacking

Field amplified sample stacking (FASS) is an important technique in analytical chemistry, especially in modern microfluidic technology. Recent development in biochip industry focuses on manipulation of extremely small amount of sample in integrated microfluidic devices. One of the challenges concerning this technology is how to obtain a measurable signal from such very low concentration of sample. To enhance the sensitivity of the assay, it is crucial to preconcentrate the sample before conducting the experiments. FASS is one such technique widely used on the microfluidic platform.

The physical mechanism for the FASS lies in variations in the electrical field in the different regions of the microchannel. The process is shown schematically in Figure 2.12. The channel contains two types of buffer with a large difference in electrical conductivity. The buffer in the middle of the channel has lower conductivity and the sample is injected in this region, while the buffer in other parts of the channel has a higher electrical conductivity. Once the electrical potential is applied across the channel, the electrical field inside the channel varies significantly due to variations in the electrical conductivity. The electrical field is high in the sample region and therefore, the sample moves faster toward the boundary between the sample and the running buffer of higher conductivity. As the sample accumulates at the interface, the electrical field decreases and the sample migration slows down. Moreover, the electroosmotic flow, which is directly proportional to the electrical field will also become weak, causing further slowing down of the sample migration. As a result, the sample will stack into a thin band near the interface between the buffer and sample region. The exact location (forward or rear interface) depends on the sample charge. The concentration of sample in this thin band is much higher compared to that before the electrical field is applied.

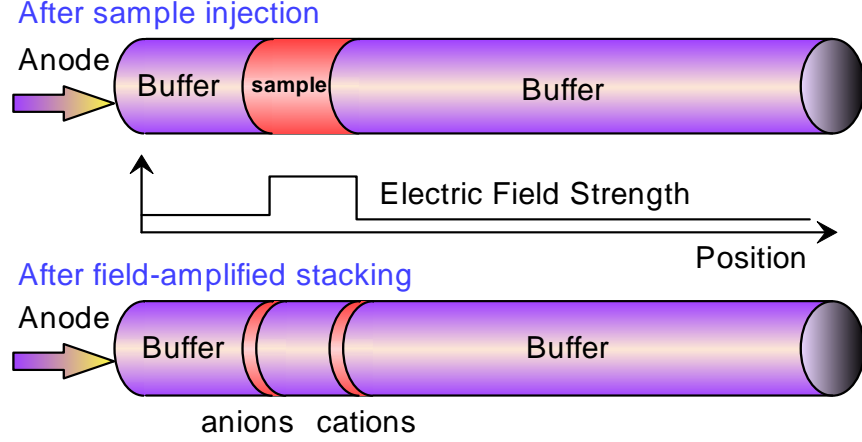


Figure 2.12: Illustration of FASS in a microfluidic channel.

Governing Equations Relevant to Stacking Phenomenon

The FASS can be described by the electrokinetic theory. The transport of the sample and running buffers obeys mass conservation laws:

$$\frac{\partial}{\partial t} c_i + \frac{\partial}{\partial x_i} J_{ij} = 0 \quad (2.26)$$

where the flux (J_{ij}) of species i is given by Nernst-Planck equation:

$$J_{ij} = u_j c_i - z_i c_i \omega_i \frac{\partial \phi}{\partial x_i} - D_i \frac{\partial c_i}{\partial x_j} \quad (2.27)$$

Here c_i , D_i , and ω_i are the concentration, diffusivity and electrophoretic mobility of the specie i , respectively, \vec{u} is the fluid velocity and ϕ is the electrical potential. In the above equation, it is assumed that the double layer at the particle-electrolyte surface is thin, the electrolyte is fully ionized and the solution is dilute. Consequently, the introduction of charged species will not alter the properties such as density, viscosity etc.

The motion of background electrolyte is described by the Navier-Stokes equation for the incompressible Newtonian fluid flow:

$$\frac{\partial}{\partial t} \rho u_i + \frac{\partial}{\partial x_j} \rho u_j u_i = -\frac{\partial p}{\partial x_i} + \frac{\partial}{\partial x_i} \mu \left[\frac{\partial u_i}{\partial x_j} + \frac{\partial u_j}{\partial x_i} \right] + \epsilon \kappa^2 \zeta \frac{\partial \phi}{\partial x_i} \quad (2.28)$$

where ρ is the density, p is the hydrodynamic pressure, κ^{-1} is the Debye-Huckel thickness, ε is the dielectrical constant of the medium and ζ is the zeta potential. The last term on the right hand of equation is the electroosmotic volumetric source term arises due to the interaction of charged wall and the ions in the solution. Two different approaches to simulate FASS have been used.

Approach 1 (Electroneutrality Assumed)

In the first approach, electroneutrality assumption has been used and solved for the current conservation equation or conduction equation. The governing equations are:

$$\nabla \cdot \vec{i} = 0 \quad (2.29)$$

where i is the electrical current density, described as:

$$i_i = \sigma \frac{\partial \phi}{\partial x_i} + \sum_{j=1}^N F z_j \frac{\partial D c_j}{\partial x_j} \quad (2.30)$$

Here σ is the electrical conductivity and F is the Faraday constant. The electrical conductivity is calculated as:

$$\sigma = \sum_{j=1}^N F z_j^2 c_j \omega_j \quad (2.31)$$

It is noted that in the solution methodology, the electroneutrality is not explicitly applied. Instead, transport equation is solved for each species independently, using the electrical drift term obtained by solving current conservation, which is obtained using electroneutrality assumption.

Approach 2 (Electroneutrality not Assumed)

In this approach, the electrical potential is obtained by solving Poisson equation:

$$\frac{\partial}{\partial x_i} \varepsilon \frac{\partial \phi}{\partial x_i} = F \sum_{j=1}^N z_j c_j \quad (2.32)$$

where ε is the dielectrical constant of the medium. With this formulation, when the source terms on the right side dominate, problems appear in obtaining the converged solution. This issue will be addressed in future.

Model validation

In order to verify the current numerical approach, the code is validated with experimental data of Bharadwaj (private communication). The schematic of the system is shown in Figure 2.13. The system used consists of an elliptical shaped geometry. The sample is prepared in low conductivity buffer (shown in gray) and the high conductivity buffer is then electrokinetically driven from the buffer well, on left, towards the sample well, on the right and the sample stacks at the interface between the two electrolytes. It is anticipated that the sample will stack at the interface between the two electrolytes. Three species can be used in this model problem and the parameters used are listed below in Table 2.2.

Table 2.2: Parameters used in single-step stacking simulation.

Species name	Diffusivity	Mobility	Charge
A+	1E-9	5.38E-13	1
B-	7E-10	3.174E-12	-1
C--	5E-10	3.12E-13	-2

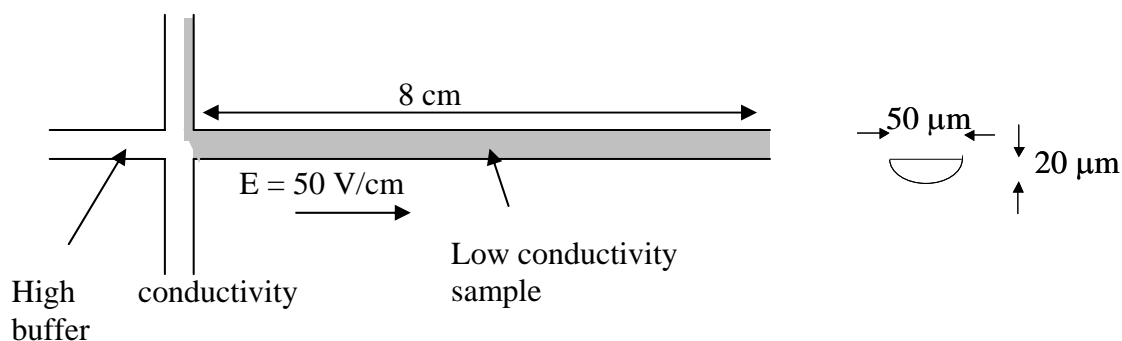


Figure 2.13: Schematic of single-step stacking device.

The hydrodynamic properties of the electrolyte are those of water. The EOF mobility is set to $7E-10 \text{ m}^2/(\text{V s})$. The initial concentration is set to:

$$C_A = 0.5C_{A0}(\gamma + 1 - (\gamma - 1)\text{erf}(a(x - s)))$$

$$C_C = C_{C0}(1 + \text{erf}(a(x - s)))$$

where $\gamma=4$ is the ratio of buffer concentration in the background high conductivity and to that in the low conductivity sample. In the simulation the following parameters are chosen:

$$s = 1E-4, a = 5E4, C_{A0} = 1E-3, C_{C0} = 1E-6$$

The concentration of species B⁻ is determined from the electroneutrality condition. A 50V/cm electrical field is applied along the channel and simulates the evolution of sample transport.

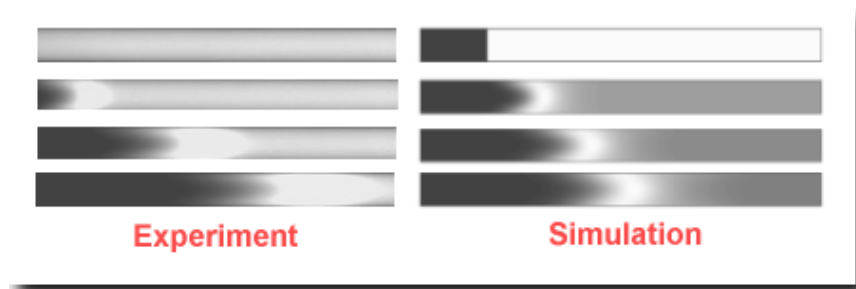


Figure 2.14: Comparison of experimental observation and simulation of sample stacking with EOF induced dispersion.

The snapshots are taken at $t=0$, 278, 558 and 834ms. The channel width is $50\mu\text{m}$.

A 2D analysis that compares the images (Figure 2.14) shows a good qualitative agreement. The team then simulates with an assumption of an infinite supply of the sample and the interface moves across the horizontal channel. The first set of simulation was performed using 1D analysis code. The results from this simulation, shown in Figure 2.15, clearly demonstrate the stacking of specie C at the interface. The peak value is almost linear as observed before by the Stanford Group. The following is observed:

- The stacking ratio of simulated results is considerably higher than that of experiments;
- The translation of the sample peak is slower than that of the experiment.

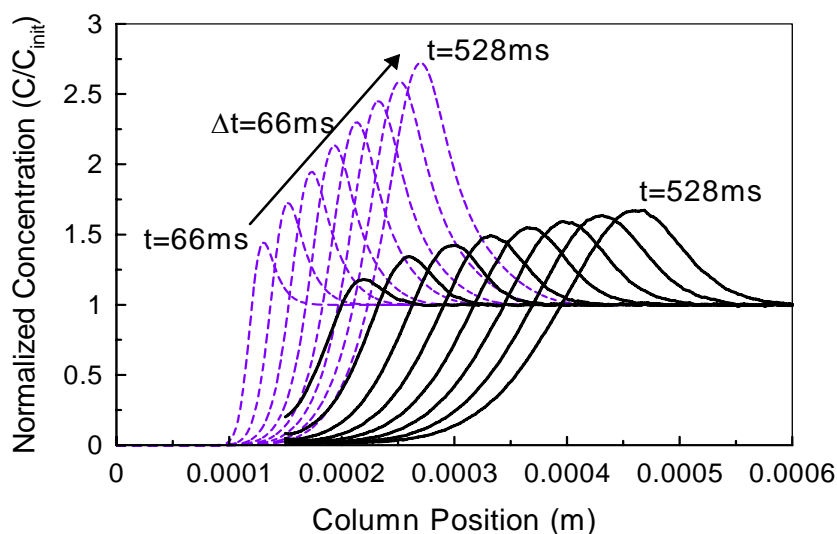


Figure 2.15: Comparison of simulated (dash curves) and experimental results (solid curves) of the normalized concentration at the centerline of the channel.

This discrepancy may possibly arise from:

1. The electrostatic interaction between analyte molecules, neglected in the present simulation, may reduce peak height.
2. The translation speed of the peak is a function of the electroosmotic mobility, which may exhibit more complex dependency on local ionic strength and pH.

From extensive simulations it is observed that the:

- Net neutrality assumption under-predicts electrical field near the electrodes and subsequently reduced sample stacking.
- Non-net neutrality assumption predicts a higher electrical field strength leading to enhanced stacking.

To address above issues, the team developed models for concentrated ionic solutions and variable zeta potential models.

(a) *Model for Concentrated Ionic Solutions:*

During sample stacking, it is normal to stack up analytes as high as 1000 times their initial concentration. At that instant, the solution becomes highly concentrated and analyte particle-

particle interaction becomes significant. This results in deviations in the values of electrical and physical properties from their respective values when the solution is dilute. To address this issue, the team has developed “unit-cell” based highly concentrated solution models to simulate sample stacking.

(b) *Model for Variation of Zeta Potential With Respect to Ionic Concentration:*

The team implemented a model that describes variation of zeta potential as a function of ionic concentration based on the work by Scales, et. al. ("Electrokinetics of the Silica-Solution Interface: A Flat Plate Streaming Potential Study. "The ACS Journal of Langmuir Surfaces and Colloids 8(3): 965-974). The accumulation of oppositely charged species on surface will neutralize the surface charge it carries and hence reduce the zeta potential ζ . Such a coupled model will exhibit different behavior from non-coupled model, where zeta potential is assumed to be constant. The non-uniformity of zeta potential will introduce the internal pressure gradient in a fashion similar to that seen in field amplified sample stacking. Such internal pressure gradient will induce Taylor dispersion that may reduce stacking efficiency.

(c) *Numerical Simulation of Full Poisson Equation:*

Numerical simulation of fully coupled Poisson equation is extremely challenging when there is a large charge accumulation leading to very large source terms and causing a numerical stiffness problem. In this regard the team has implemented a full Poisson equation solver that uses a SUPER LU scheme to solve stiff equation (due to high source term that rises from charge accumulation) that describes electric field distribution.

2.1.7 Model for EK Phenomena in Concentrated Electrolyte Solutions

During several electrochemical processes prevalent in the biotech industry (e.g., sample stacking) sample concentration increases and the solution may become highly concentrated. When this happens, the dilute approximation, based on which current ACE+ models are formulated, may become unstable/invalid. Hence, the team has developed methodologies for solving highly concentrated solution based on a semi-implicit coupled approach. This is discussed next.

Stability of the concentration and potential solutions is first sought to be improved by strengthening the coupling during numerical solution. CFD-ACE+ solves charged analyte transport equations under electrostatic field as following:

$$\begin{aligned} \nabla \varepsilon \nabla \phi &= F \sum z_i c_i \\ \frac{\partial c_i}{\partial t} + \nabla \cdot (\mathbf{v} c_i) + \nabla \cdot (z_i \omega_i \mathbf{E} c_i) &= \nabla \cdot (D_i \nabla c_i) \\ \mathbf{E} &= -\nabla \phi \end{aligned} \tag{2.33}$$

The original implementation will face convergence problem if the electro non-neutrality term dominates. The previous equations are manipulated multiplying the valance and Faraday constant and summing through all analytes:

$$\frac{\partial(F \sum z_i c_i)}{\partial t} + F \sum z_i \nabla \cdot (\vec{v} c_i) + \nabla \cdot (F \sum z_i^2 \omega_i \vec{E} c_i) = F \sum z_i \nabla \cdot (D_i \nabla c_i) \quad (2.34)$$

This equation gives the charge density at next time step in terms of ion concentration at old time step:

$$(F \sum z_i c_i)^n = (F \sum z_i c_i)^o - \nabla \cdot (\Delta t \cdot F \sum z_i^2 \omega_i \vec{E} c_i) + \Delta t \cdot F \left\{ \sum z_i [\nabla \cdot (D_i \nabla c_i) - \nabla \cdot (\vec{v} c_i)] \right\} \quad (2.35)$$

The modified electrostatic equation for new time step is therefore,

$$\nabla \cdot (\epsilon + \Delta t \cdot F \sum z_i^2 \omega_i c_i) \nabla \phi = (F \sum z_i c_i)^o + \Delta t \cdot F \left\{ \sum z_i [\nabla \cdot (D_i \nabla c_i) - \nabla \cdot (\vec{v} c_i)] \right\} \quad (2.36)$$

For steady state simulations, the time step can be simply set a large number. This methodology has been developed (by CFDRC under a different contract) and has been used in this project to simulate FASS. The numerical scheme is summarized in Figure 2.16.

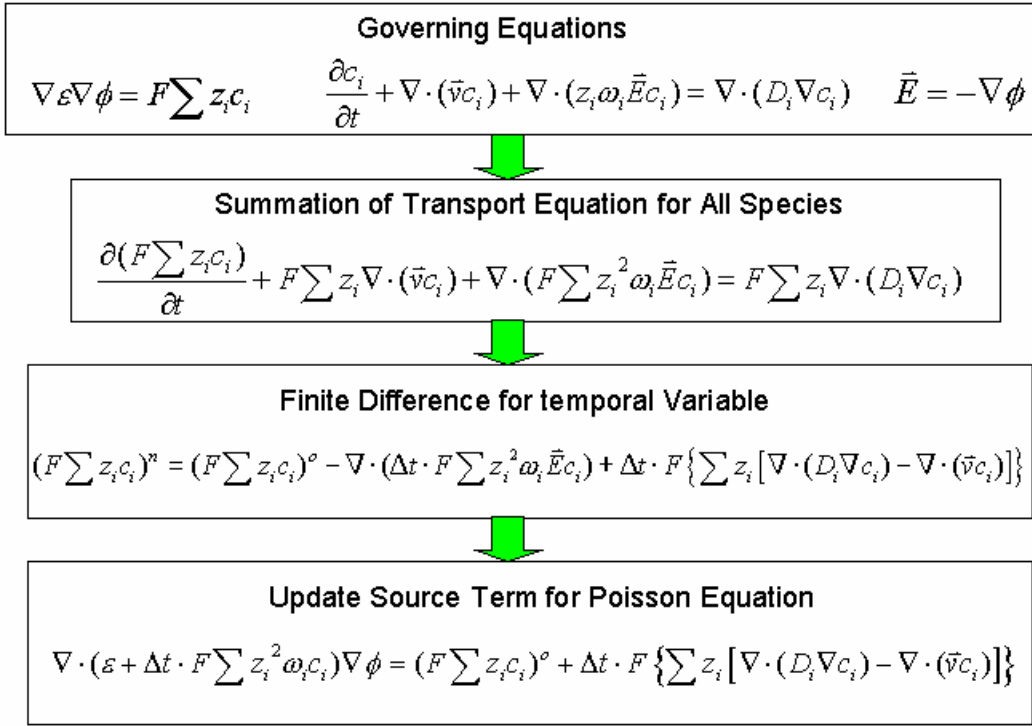


Figure 2.16: A semi-implicit scheme for Poisson equation coupled with species transport.

2.1.8 Microsphere-Based Sandwich Immunoassay Modeling Capability

The basic concept of tagged antibodies (primary antibody) anchored to the microbead surface and then exposed to target analytes in the flow system is well known. In order to quantify the antigen bound and also to increase the sensitivity of the signals and accuracy of measurement, “sandwich immunoassays” is used. Here, one more step is added to the immunoassay, which is known as the “Reporter Step”. These types of assays have found wide application in biotechnology. Figure 2.17 below explains the basic concept involved in sandwich immunoassays.

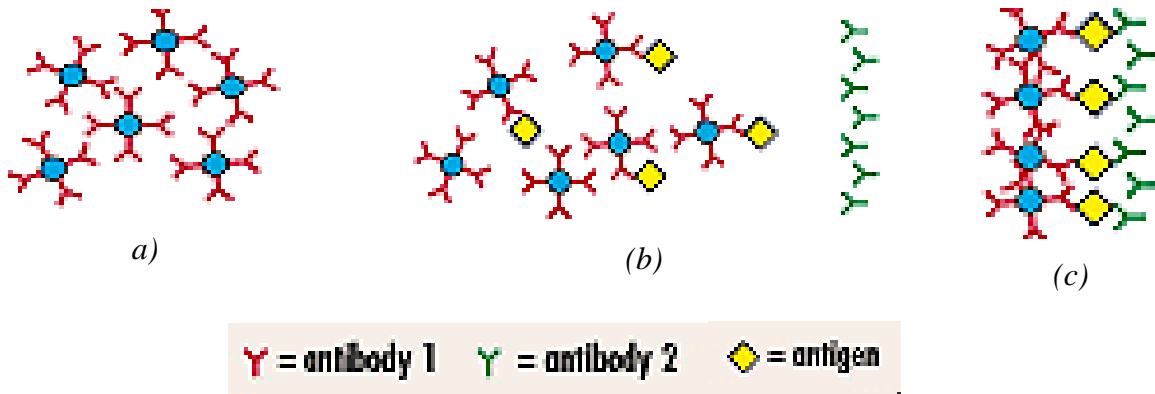


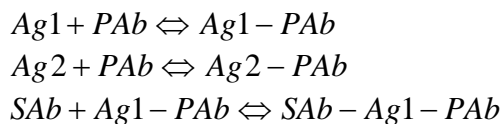
Figure 2.17: Schematic of the sandwich immunoassay.

(a) Primary antibody coated microsphere, (b) antigen bound to primary antibody on microsphere, and (c) reporter step.

In this case the primary antibody is immobilized on the microsphere. Buffer containing antigen is added and allowed to react with the bound primary antibody as shown in Figure 2.17b. After sufficient mixing and binding, excess buffer and antigen are washed off. After this step, the secondary antibody (specific for the distinct epitope on the antigen) is added and allowed to react with the bound antigen. Again, after sufficient mixing and binding, the excess secondary antibody sample is washed off and the beads are sent to a cytometer, where the bead fluorescence (on excitation of laser) is measured. The intensity of fluorescence on the microsphere surface is proportional to the concentration of secondary antibody in each sample.

Model Validation for Sandwich Assay

The sandwich immunoassay is easily modeled using the existing generalized surface chemistry solver implemented in the CFD-ACE+ multiphysics engine. During a simulation, diffusional mass transfer to the bead surface, and the surface reactions are balanced for all surface reactions simultaneously. The model was validated first against semi-analytic expressions possible for a static incubation assay. Here Primary Antibody (PAb) coated microspheres are incubated (no flow) with excess of Antigens 1 & 2 (100 nM). The set of reactions are:



Model equations reduce to a system of linear ODEs for this static incubation case, which were solved with using the ordinary differential equation solver (ode45) available in MATLAB[®] and the results are compared with CFD-ACE+ results for the static case. The time evolutions of all

three surface species are identical (Figure 2.18), validating the integration of multi-step kinetic models.

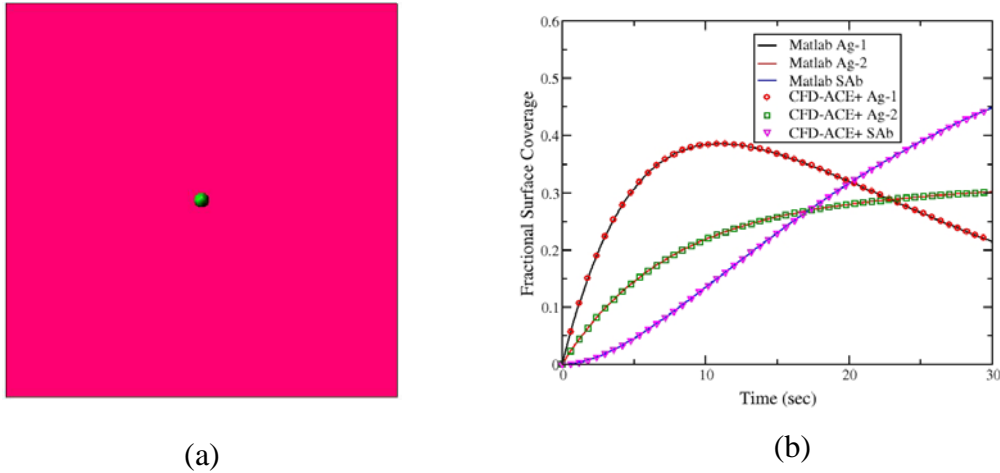


Figure 2.18: (a) Static incubation assay with microsphere.

(b) ACE+ binding results compared with the numerical solution of the underlying ODE's.

Demonstration of the Microsphere-Based Immunoassay Model

A demonstration of the multi-step bead assay model in a typical lab-on-a-chip as illustrated in Figure 2.19. Primary antibody coated beads are injected from Inlet 1. A mixture of antigens is injected from Inlet 2. The antigen mixes with antibody coated antibodies in the vertical channel. The excess antigens are washed out via Outlet 1. Next, fluorescence tagged secondary antibodies are injected via Inlet 3. The secondary antibody complexes only with the antigen that is already captured on the beads. Excess secondary antibody is washed out. Finally, the amount of fluorescence detected on the beads (via the bound secondary antibody) serves to quantify the presence of the original antigen.

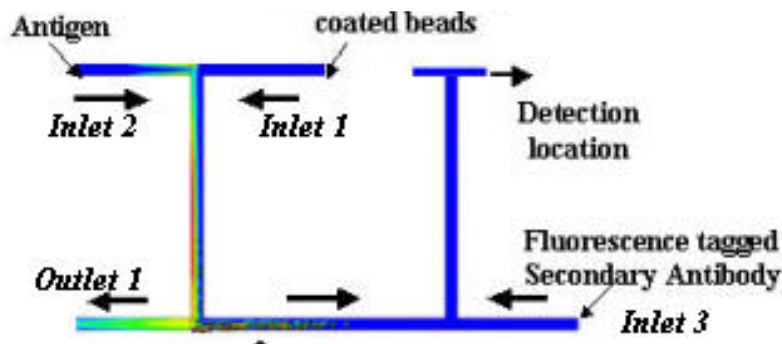


Figure 2.19: Schematic of multi-step microsphere assay demonstration/validation study

A demonstration assay was carried out using values based on the Interleukin – receptor system. Figure 2.20a shows a snapshot of beads, covered with the primary antibody entering the turn (leading to Outlet 1). While a small amount of beads are lost to the outlet, the vast majority make it into the continuing channel. Peak coverage of about 40% is seen indicating that the length, while sufficient, is not enough to saturate the beads. The secondary binding is shown in Figure 2.20b. Once again, very few beads are lost in the turn. Interestingly, less than a third of the primary covered antibody is bound to the secondary, signal-generating, antibody indicating that this particular assay can indeed be further optimized using the existing simulation models.

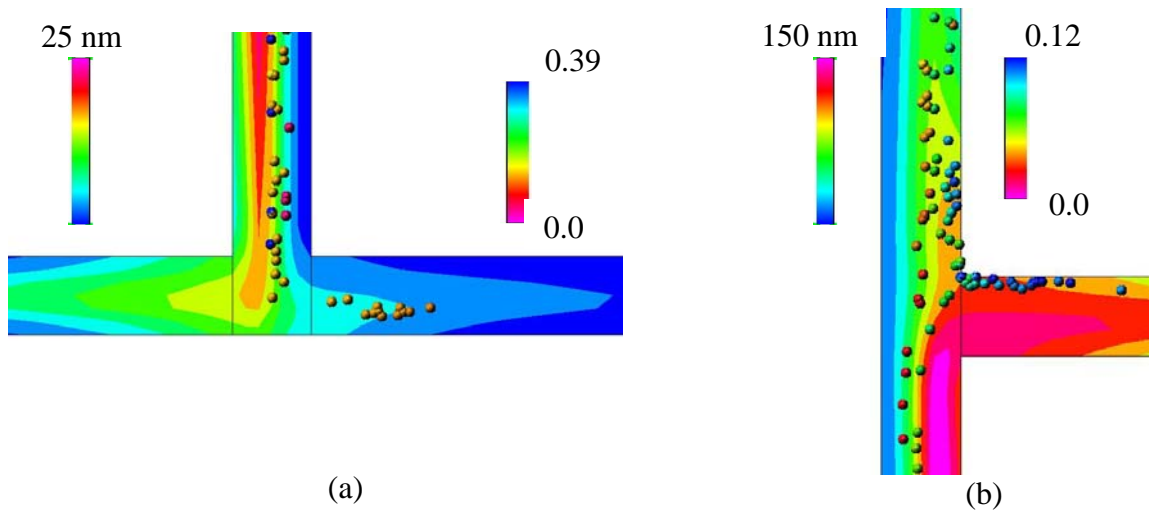


Figure 2.20: (a) Primary antibody binding. (b) Secondary antibody binding.

Demonstration of a Multiplexed Bead Assay Application

The multiplexed bead assay is demonstrated on a T-junction (commonly found in many microfluidic lab-on-a-chip systems) to mix microbead solutions with sample solutions (Figure 2.21). The horizontal channel was 100 μm wide and 2200 μm long, while the vertical channel was 100 μm wide and 500 μm long. Two different analytes of the cytokine family, IL-2 and IL-4 were used for these simulations. The diffusivity of both the analytes was set at $10^{-11} \text{ m}^2/\text{s}$. 10 μm beads coated with the respective antibody against IL-2 and IL-4 were used. The adsorption constant (K_a) for the interaction between IL-2 and its antibody was $8 \times 10^6 \text{ M}^{-1} \text{ s}^{-1}$ and between IL-4 with its corresponding antibody was $5 \times 10^7 \text{ M}^{-1} \text{ s}^{-1}$. The total available site for binding was $10^{-6} \text{ moles/m}^2$. IL-2 and IL-4 plugs were injected for 3 seconds each, in the horizontal channel at a velocity of 0.001 m/sec with the concentration of 10^{-6} M . IL-2 was injected first followed by IL-4 with an interval of 6 seconds between the injections. The beads coated with the respective antibodies were injected from the vertical channel in a buffer solution at the same velocity. The beads were injected 3.5 seconds after the introduction of IL-2, timed so that both beads and the cytokines arrive at the junction at the same time. The total time of the assay was 30 seconds.

Figure 2.21 shows the channel at 5 seconds with the first analyte (IL-2) and bead plugs (coated with antibodies to both IL-2 and IL-4) entering the respective channels. As expected the IL-2 is diffusing across the channel and the beads show no coverage as they have not yet encountered the cytokine. At 15 seconds (Figure 2.22), IL-4 has entered the channel, while the beads are mixing with the IL-2 plug. Note that only some of the beads in contact with the IL-2 are changing color, indicating the presence of IL-2 specific antibody while the IL-4 antibody coated beads remain colored blue.

Figure 2.23 shows the channel at 18 seconds when IL-2 is exiting the channel and IL-4 has reached the center of the channel. Notice that some of the beads (now the ones coated with IL-4 specific antibody) are detecting the presence of IL-4 while no change is seen in the IL-2 antibody coated beads. At a much later time (Figure 2.24) IL-2 has exited the channel and the IL-4 antibody coated beads are seen to have detected the presence of IL-4. This study can be readily extrapolated to include an arbitrary number of analytes and beads.

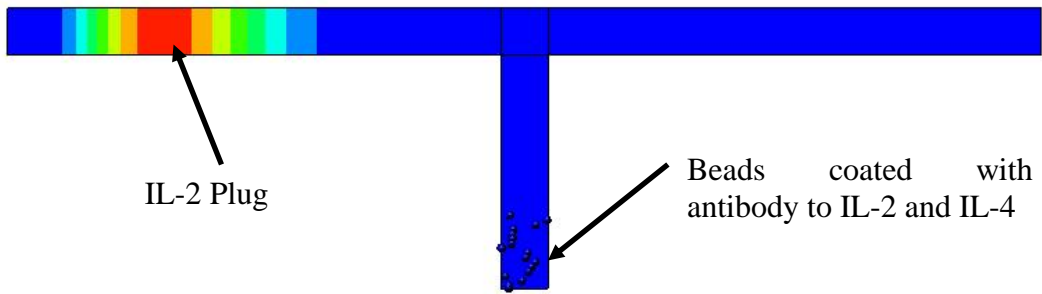


Figure 2.21: T junction at time = 15 seconds following injection.

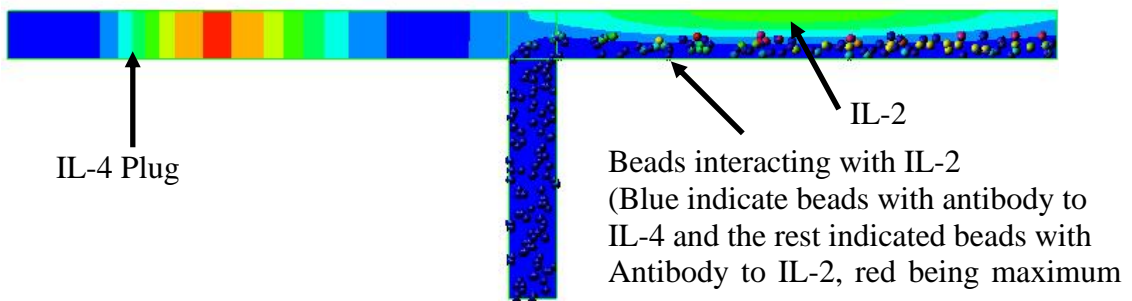


Figure 2.22: T junction at time = 15 seconds following injection.

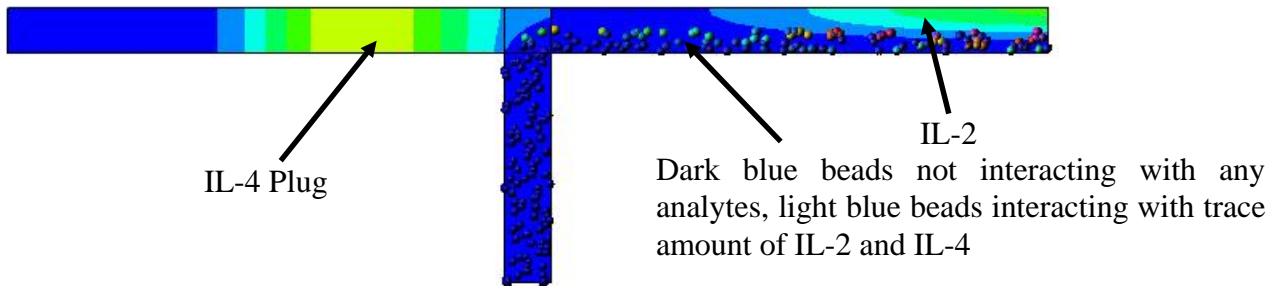


Figure 2.23: T junction at time = 18 seconds following injection

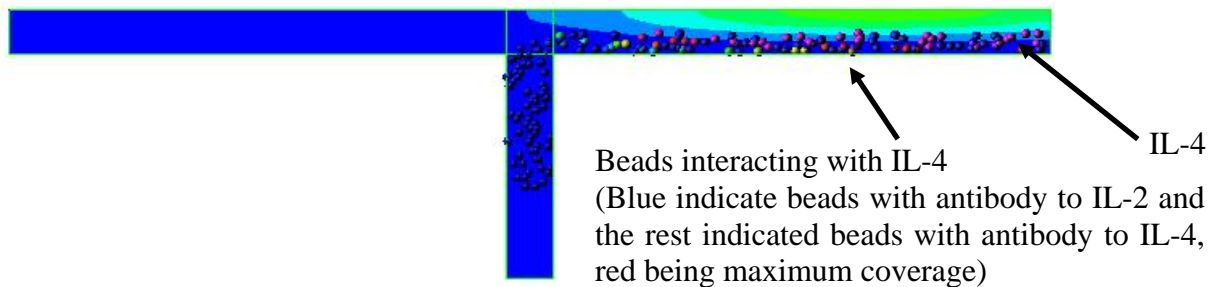


Figure 2.24: T junction at time = 25 seconds following injection (*IL-2 has been washed out of the channel at this time*)

Effect of Analyte/Bead Flow Rates on Detection

The goal of all biochemical assays is to yield the maximum signal in the shortest time possible. The signal, however, depend upon a multitude of variables such as geometry, flow rates, concentrations etc. in a very complex and intertwined manner. Here, the team has chosen to study the effect of one of the most important and easily controllable parameters i.e. antigen and bead flow rates. The geometry considered is a Y-junction employed in many microfluidic systems. The length of the arm of channel is 0.5 mm and its width is 0.05 mm. The length of the straight channel is 2 mm and its width is 0.1 mm. The sample analyte (plug) and buffer enters from upper arm of the channel and beads in a buffer solution enter from lower arm of channel. The diffusivity of the analyte is set at $5 \times 10^{-10} \text{ m}^2/\text{s}$. The bead fluorescence (coverage) is measured at the exit of the channel (at outlet). The analyte concentration used in all the cases is 10^{-6} M . $5 \mu\text{m}$ beads, coated with receptors, are released in the lower arm. An adsorption constant of 10^6 is prescribed, for the purposes of this calculation.

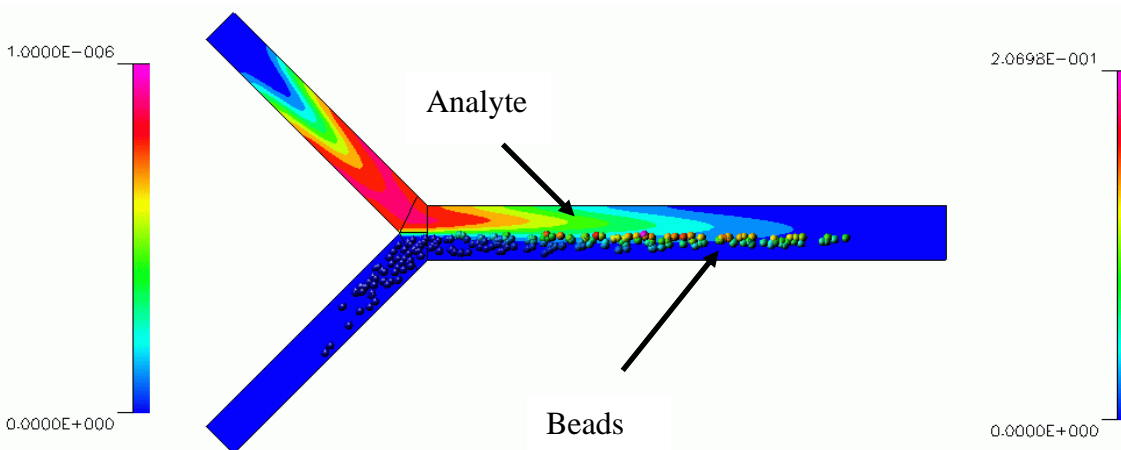


Figure 2.25: Analyte concentrations and bead coverages for a flow ratio of 5(An):5(B).

For the baseline case, equal flow rates of analyte and bead entering the channel are considered (Figure 2.25). Note that the analyte and bead each occupy half the channel with very little mixing. The suboptimal mixing and presentation of sample to the bead, causes a low level of surface coverage. Considering that the threshold of detection in many cases requires around 30% coverage and the present protocol shows substantially less coverage than that, it can safely be concluded that the test as presently conducted has a high probability of yielding a false negative.

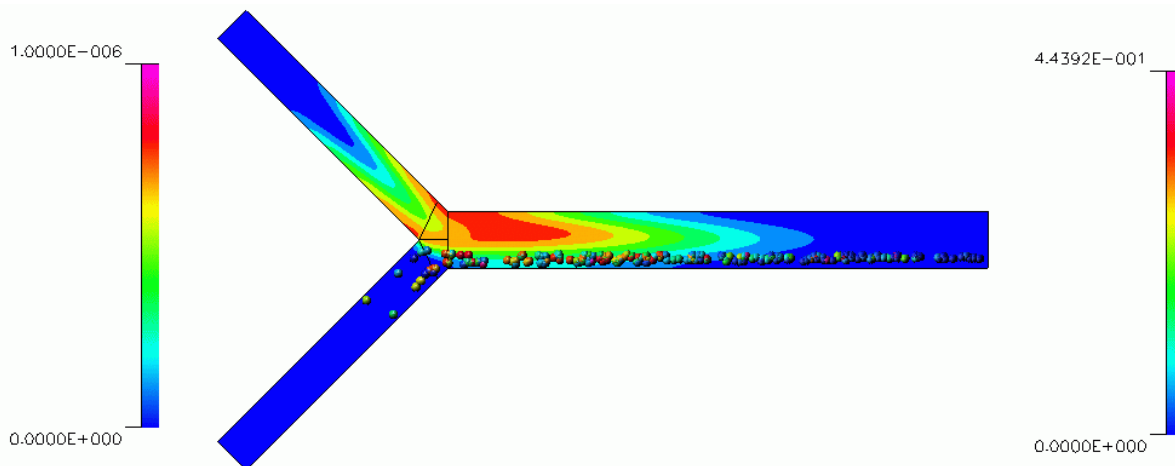


Figure 2.26: Analyte concentrations and bead coverage for a flow ratio of 5(An):1(B)

Decreasing the bead flow rate can be intuitively expected to increase the residence/contact times between the sample and antibody (on the surface of the beads) and thereby increase coverage/detection. This is indeed seen to happen as seen in Figure 2.26. Moreover, the hydrodynamic effect of focusing the beads in the low-speed fluid near the wall, also enhances the signal via increased diffusive transport of analyte to the surface of the beads

The overall signal evolution with time at the detection point (at the exit of the channel) is shown in Figure 2.27. Firstly, as expected, the time to detect is shortest in the 5:5 case, as the beads travel fastest through the system and reach the detection point. However, as seen earlier, the coverage levels are low with the possibilities of false negatives, high. The 5:1 case, where the beads travel slowly, on the other hand exhibits a higher coverage that is also sustained for longer times. Hence it is concluded that flowing the beads in slowly is the preferred mode of operation in this assay.

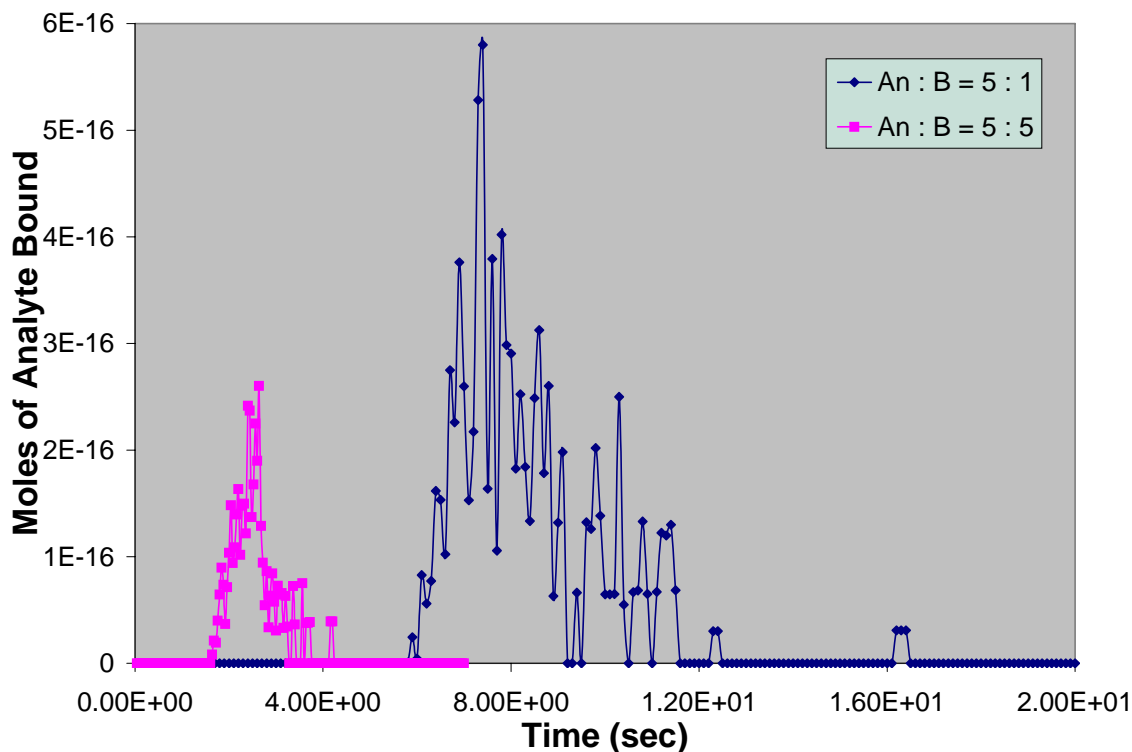


Figure 2.27: Signal (sensorgrams) evolution with time.

2.1.9 Simulation of Combined DEP and Microbead Assay

The DEP and the microbead assay models were successfully coupled to simulate analyte binding on a microbead cluster while they were being transported across a microchannel to due AC electric field. For this simulation, fluid flow is solved, AC electric field, DEP-induced bead motion and analyte-antibody binding.

A total of 100 microspheres were introduced randomly at the intersection of a cross-channel configuration that is $100 \times 100 \mu\text{m}$ in dimension. Water is considered as the fluid medium occupying the cross channel initially. The physical and electrical properties of the medium and spheres, provided by UC Santa Barbara, are listed in table 2.3.

Table 2.3: Physical and electrical properties of the medium (DI water) and microspheres (by UCSB)

Frequency (Hz)	100 Hz	Fluid Density	1000 Kg/m ³
Particle Radius	0.1 μm	Particle Density	1000 Kg/m ³
Conductivity of Particle	1.0E-14 1/Ohm-m	Conductivity of the Fluid	0.56 1/Ohm-m
Relative Permittivity of Particle	2.61	Relative Permittivity of Fluid	80

Microspheres were coated with IL-2 antibody. IL-2 analyte was assumed to be initially restricted to the left and right chamber of the domain. The diffusivity of IL-2 was set at $1.0\text{E}-10\text{ m}^2/\text{s}$. The adsorption constant (K_a) for the interaction between IL-2 and its antibody was $8 \times 10^6\text{ M}^{-1}\text{ s}^{-1}$. The available binding site density on the microspheres was $1\text{E}-06\text{ moles/m}^2$. An AC electric field of 10 V is applied to the top and bottom electrodes. The frequency of the AC field was kept at 100 Hz. Since the relative permittivity of the particle is less than that of the medium, it will experience a negative DEP (moves toward electric field minima).

Figures 2.28 and 2.29 show the initial concentration contours of IL2, and the contours of electric field squared, respectively. The random locations of the microsphere are superimposed the top of the contour plot. Figure 2.29 illustrates the sequence of operation as it occurs in the cross channel. From Figures 2.29a to 2.29d, the beads migrate horizontally on either direction (positive and negative x-direction) towards the electric field minima (Figure 2.29a) as expected. As they migrate, they displace fluid volume in the left/right chambers, which sets up chaotic mixing regions within the domain. The IL-2 in the horizontal channel also starts to bind with the IL-2 antibody coated on the beads. This is illustrated via a color change on the bead (blue to red). At time $t = 2$ seconds, almost all the beads have accumulated near the electric field minima and the antigen-antibody binding is almost complete.

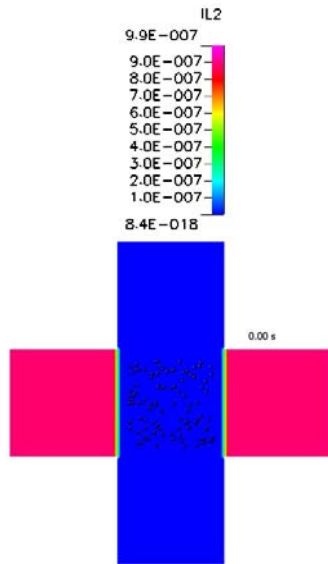


Figure 2.28a: Concentration contours of IL2 at time $t = 0$

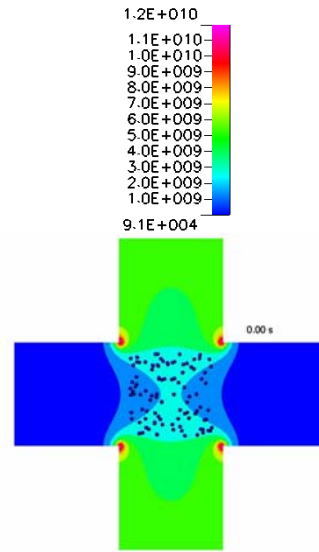


Figure 2.28b: Contours of electric field squared at time $t = 0$

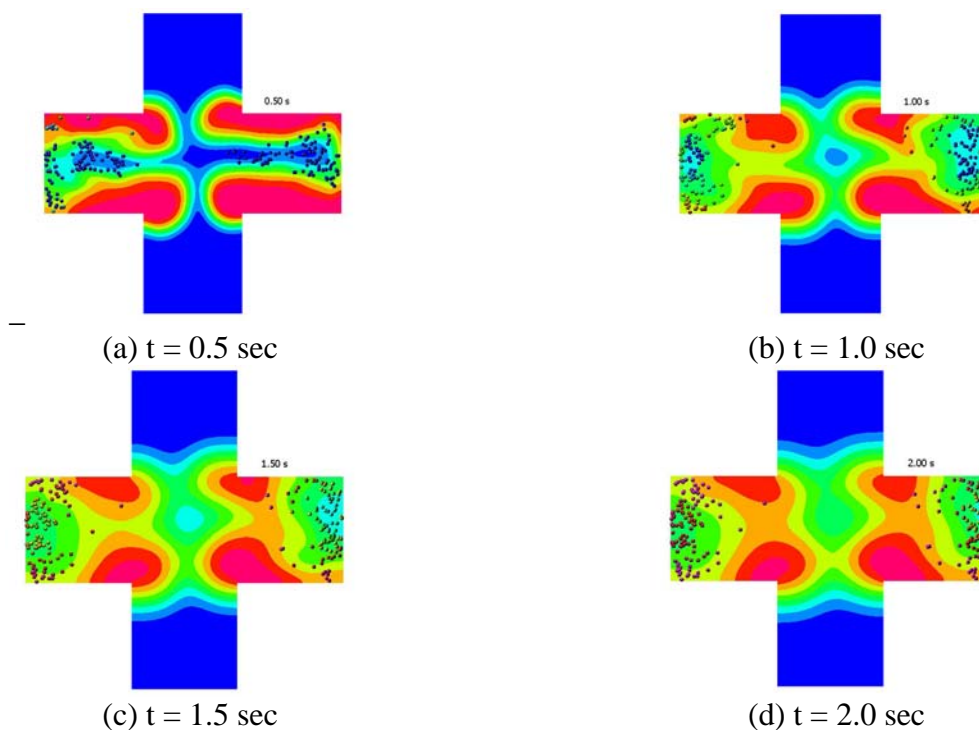


Figure 2.29: Location of microspheres shown at different time levels.

The color of the sphere indicates extent of antigen-antibody binding (blue -> all receptor sites available, red -> no site available). Contour levels of IL2 are also shown.

2.1.10 Architecture for Biomolecular Databases

Primary integration of the Biochemistry and Electrochemistry modules in CFD-ACE+ is complete. The Electrochemistry module has a detailed chemistry database structure set-up for gas-phase chemistry for semiconductor applications. The team designed similar database architecture for the biomolecular reaction kinetics data as well. A sample graphical-user-interface for specifying/choosing biomolecular surface interactions is shown below in Figure 2.30. After completion of this task, the user can readily choose from a wide range of data pertaining to biomolecular kinetics, presented in an intuitive, easy-to-use format.

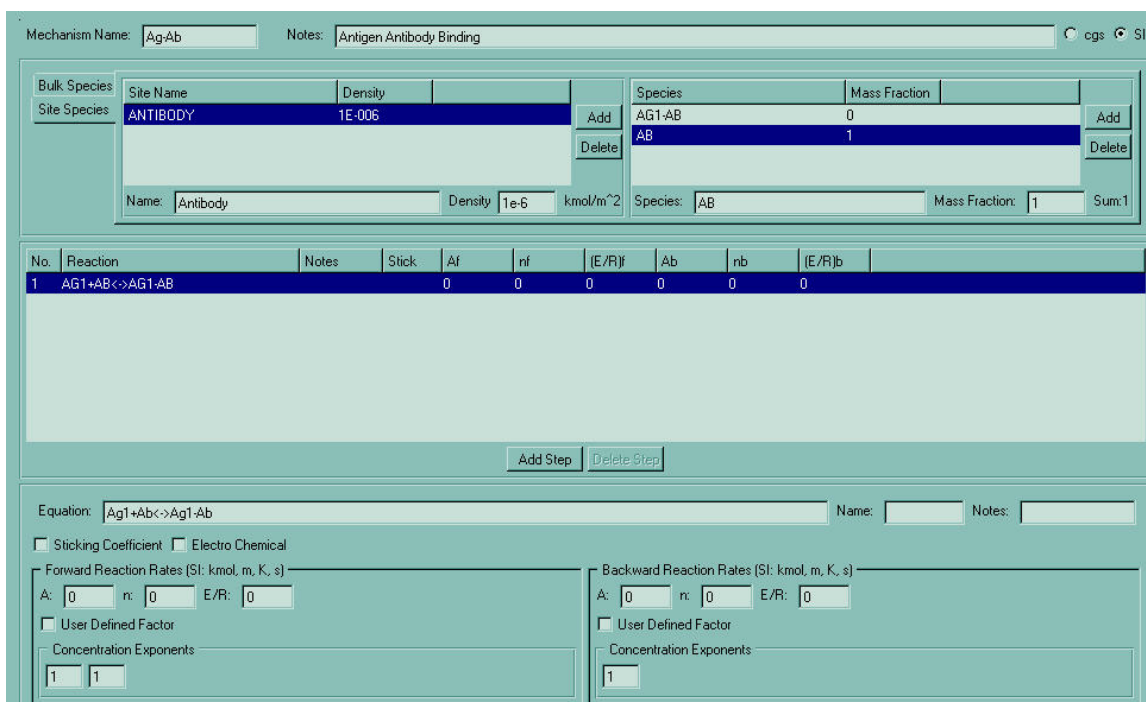


Figure 2.30: Developed architecture for surface biokinetics manager.

This user interface keeps track of reactions, reagents, and the salient reaction kinetics and transport parameters.

2.1.11 Neural Net Modeling for Data Extraction

Work was performed on the adaptation of the Artificial Neural Network (ANN) models to the extraction of the coefficients associated with surface reaction kinetics. The approach taken is based on treating the ANN as a reduced model for time series prediction. The time series represents the time history of surface concentration as a function of input flow rate, temperature, as well as the maximum allowable surface and initial bulk concentrations. System geometry is taken as constant. This non-linear dynamical system is being represented by a static topology ANN in a dynamic configuration of the general form:

$$(2.37) \quad y(t+1) = f[y(t), y(t-1), \dots, y(t-m), u(t), u(t-1), \dots, u(t-n)]$$

where $y(t)$, $u(t)$ represent the time dependent output and input, respectively. The work was performed in three stages: (1) General ANN preparation; (2) Input/Output Data Preparation; and (3) Model-Based ANN preparation.

1) General ANN Preparation: The static ANN is cast in a general feed-forward Multi Layer Perceptron (MLP) topology with time lagged elements and global feedback capability. The work involved using model problems for testing of training techniques for selected candidate ANN topologies. The topologies under consideration include ANNs with feedback elements. Such representations can in principle model very complex dynamical systems but require more general training techniques. Test of these ANNs are nearly complete. The final selection of the most suitable ANN architecture will be based on test results using experimental data.

2) Input/Output Data Preparation: Since the time-dependent process that the ANN is modeling is of finite duration all ANN training will be done off-line using archived experimental and computational data. The existing ANN software, designed for on-line computations using real-time input, was extended to accept archived, file-based data. Tests of this extension are complete.

3) Model-Based ANN Preparation: A general model-based ANN implementation for extraction of the reaction rate coefficients has been completed and tested on simple problems. The implementation involved: (a) modification of the ANN structure to allow specification of analytical expressions to compute the final ANN output (concentrations); and (b) modification of the training procedure to include the effects of model coefficients variation on the output error. Complete tests and training of this formulation will be performed using the topology as described in the paragraph above.

ANN Training Set Generation

Training data for the neural network was generated using a model of the SPR biosensor - Biacore. The data sets were generated using the CFD-ACE+ multiphysics software to simulate the effects of fluid flow, mass transport via diffusion, and the binding of analyte to receptor on the lower surface of the Biacore device. The surface binding module assumes isothermal, Langmuir adsorption through an adsorption (K_a) and desorption (K_d) term. The system variables held constant were the sensor surface receptor concentration of $2.5 \text{ E-}8 \text{ mole/m}^2$, inlet analyte concentration of 225 nM, flow rate of 50 $\mu\text{L/min}$. The analyte was flowed in for 50 seconds followed by a 30 second wash phase to mimic actual experimental conditions. Kinetic constants K_a and K_d were paired over a wide range to capture the effects of kinetic and mass transport limitations (Figure 2.31), so as to assure the validity of ANN results over the widest possible range of experimental conditions. 100 data sets were generated for the neural network training.

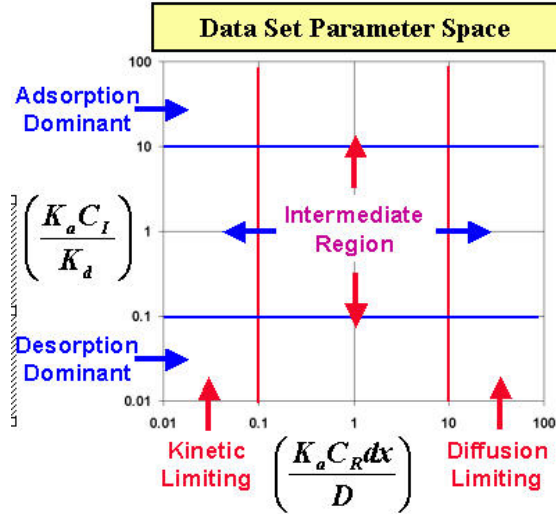


Figure 2.31: Parameter space for training ANN

(Kinetic to diffusion controlled. Adsorption to desorption dominant)

Neural Network Training

Artificial Neural Networks (ANN) with the feedforward Multi Layer Perceptron (MLP) architecture are being used in this study. The ANNs are trained to correlate the time variation of surface concentration $C(t)$ to the numerical values of the kinetic coefficients (K_a , K_d), over a range of the latter. The networks thus define a reduced model for a physical process, capable of predicting the time variation of $C(t)$ for selected (K_a , K_d) values. Currently the nets are being trained using the standard Backpropagation (BP) algorithm with a momentum correction. Typical values of the learning rate and the momentum factor are on the order 1. Several multiplayer topologies are being investigated with inputs and outputs defined by (t, K_a, K_d) and $C(t)$, respectively. The training data contains 8000 datapoints representing 100 concentration histories for different (K_a , K_d) values, with 80 time steps per history. Tests to date indicate that the following topologies give favorable results: 3-20-10-1 and 3-20-10-10-1. The first and last numbers in the previous strings represent the number of inputs and outputs, respectively, and the intermediate values denote the number of neurons in the hidden layers.

Parameter Extraction Results for Neural Network

A fully trained neural network allows for rapid extraction of kinetic constants using a non-linear least squares optimization protocol. The experimental data is essentially curve fit using the neural network as the generator of the theoretical curve. The neural network takes as input a (K_a , K_d) pair and a set of discrete time points and gives as output the surface concentration at each time point. In the current case, a Gauss-Newton non-linear least squares algorithm is used to minimize the squared error between the experimental data and the neural network generated data. The “experimental data” used in this case was a data set was generated with CFD-ACE+ for a $K_a = 8E+6$ 1/(M-s) and $K_d = 0.24$ 1/s. This pair was not one of the pairs in the original training set, but was contained within the bounds of the training set.

The kinetic constants extracted from the experimental data were $K_a = 7.7E+6$ 1/(M-s) and $K_d = 0.19$ 1/s, agreeing well with the known parameters (Figure 2.32). *The time for extracting the kinetic parameters from the data sets was approximately 5 minutes* using the neural network. Please note that parameter extraction using a fully three dimensional ACE+ simulations takes approximately 15-30 hours depending on the initial guess. The time for training data set generation was approximately 6 hours, with a training time of 1-3 hours depending on the training algorithm.

	Actual	ACE+	NN
K_a	8E6	8E6	7.7E6
K_d	0.24	0.24	0.19

Curve Fitting Time:
ACE+ \approx 1 week (3D)
ACE+ \approx 2 hours (2D)
NN \approx 5 minutes

Figure 2.32: Comparison of ACE+ and ANN rate constants, along with the time taken.

(Training time is around 1-3 hours).

2.1.12 Proteomics – Array Based Biosensors Models and Validation (CFDRC and Univ. of Utah)

In many of the SPR sensors (including Biacore) the immobilized species (receptor) is covalently attached to a very thin hydrogel matrix (usually a dextran matrix) relative to the height of the microchannel. For example, in the Biacore flow cell the height of the flow channel is usually on the order of 50 μm , while the height of the hydrogel layer is generally on the order of 100 nm. This scale disparity precludes any explicit simulation of the gel layer. However, the presence of these capture surfaces has been shown to be of critical importance and must be taken into account in high-fidelity computational models[30].

The most common method used for modeling ligand transport within a porous layer is the cylindrical pore model originally proposed by [31]. This model accounts for the equilibrium partitioning of the bulk concentration into the hydrogel layer along with the hindered diffusion experienced by a ligand molecule traveling through a network of cylindrical pores. These partition and hindered diffusion coefficients, in turn, depend on hydrogel and the protein molecular characteristics. Based on prior investigations, [30], [32] the team have developed and implemented within the convective-diffusive-reactive framework of CFD-ACE+, a model to explicitly account for the partitioning, hindered diffusion and volumetric binding effects due to the gel layer.

The main difference between this approach and prior surface biochemical models is that the receptor, analyte, and receptor/analyte complex are described volumetrically within the dextran matrix (as opposed to surface concentrations). Complex effects such as change in pore size due to analyte-receptor complexation are accounted for in this approach. Partitioning of the analyte from the bulk solution into the dextran matrix is accomplished following the vertical cylindrical pore model of Giddings et al. (1968). Here, as a starting point, it is assumed that the partitioning can be characterized using geometric considerations without introducing thermodynamic parameters. The dynamic porosity of the dextran matrix can be computed as follows:

$$\varepsilon(t) = 1 - \left(\frac{4\pi N_A}{3\delta_{dextran}} \right) \left(C_{Receptor}^o r_{Receptor}^3 - C_{Complex}(t) r_{Analyte}^3 \right) \quad (2.38)$$

Where N_A is Avagadro's Number, $\delta_{dextran}$ is the thickness of the dextran layer, $C_{Receptor}^o$ is the available number of receptor sites, $C_{Complex}(t)$ is the time varying analyte/receptor complex, and $r_{Analyte}$ and $r_{Receptor}$ are the analyte and receptor hydrodynamic radii respectively. Now, the average vertical pore radius can be estimated as:

$$r_{Pore}(t) = \left(\frac{2}{3} \right) \left(\frac{\varepsilon(t)}{1 - \varepsilon(t)} \right) \left(\frac{r_{Receptor}^3 - r_{Analyte}^3 \left(\frac{C_{Complex}(t)}{C_{Receptor}^o} \right)}{r_{Receptor}^2 - r_{Analyte}^2 \left(\frac{C_{Complex}(t)}{C_{Receptor}^o} \right)} \right) \quad (2.39)$$

The partitioning coefficient is then specified as:

$$\phi_{Partition}(t) = \left(1 - \frac{r_{Analyte}}{r_{Pore}(t)} \right)^2 \quad (2.40)$$

The concentration of unbound analyte within the dextran matrix (no gradients are assumed to exist internal to the dextran layer).

$$C_{Analyte}^{dextran}(t) = C_{Analyte}^{Interface}(t)\phi_{Partition}(t)\varepsilon(t) \quad (2.41)$$

The boundary conditions in the CFD model need to be modified to include the presence of the dextran layer and the partitioning that takes place. Figure 2.33 illustrates the adjusted flux balance boundary condition that accounts for the presence of the dextran layer. The final balancing of the transport and reactive fluxes is of the form:

$$\frac{D}{\delta - \delta_{dextran}}(C_{Analyte}^{Bulk} - C_{Analyte}^{Interface}) + K_d C_{Complex}^{dextran} - K_a \varepsilon(t)\phi(t)C_{Analyte}^{Interface} C_{Receptor}^{dextran} = 0 \quad (2.42)$$

The first term refers to the diffusive flux of analyte between the cell center and the dextran interface. The second and third terms describe desorption and adsorption of the analyte/receptor complex, respectively.

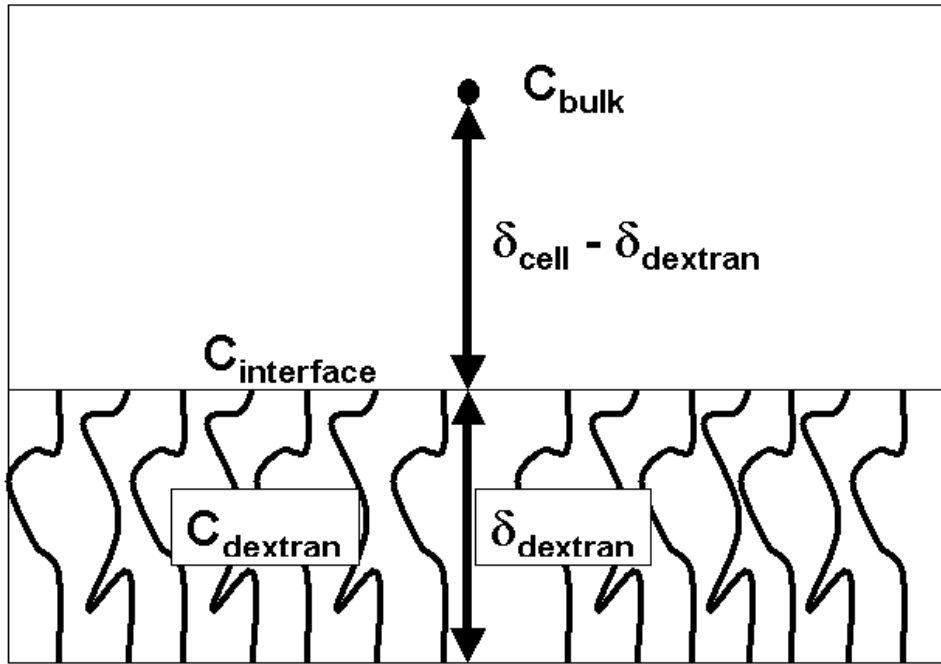


Figure 2.33: Illustration of the adjusted flux balance boundary condition accounting for the presence of the dextran layer.

The diffusive flux is balanced from the center of the cell to the dextran interface. The interfacial concentration is then assumed to partition into the dextran matrix.

The above model has been implemented in the previously available biochemical reaction framework inside CFD-ACE+. The inputs to the model (in addition to the traditional inputs) are

the hydrodynamic radii for the analyte and receptor, the thickness of the dextran layer and initial pore radii and porosities. An example calculation (to gain insight into model behavior) was carried out using the full 3D Biacore geometry (created previously). The buffer flowrate was set at a typical value of 100 $\mu\text{L}/\text{min}$ with an analyte inlet concentration of 0.20 μM . The binding kinetics were set at $K_a=57000 \text{ (M}\cdot\text{s)}^{-1}$ and $K_d=0.045 \text{ s}^{-1}$. The density of available binding sites was set to $9.7\text{E-}8 \text{ mol}/\text{m}^2$. The key parameters, in addition to the Damkohler and Kinetoc numbers described earlier for the virgin surface capture simulations described earlier, are the ratio of analyte to pore radii and the overall porosity. As expected the capture/coverage decreases as the ratio of analyte size to pore size increases (Figure 2.34). This is mainly due to the hindrance effects associated with the decrease in the average vertical cylindrical pore radius as the pores fill with analyte-receptor complex. This is mechanistically reflected by the partitioning coefficient decreasing with decrease in pore size (alternatively increasing analyte size). Characterizations of other parameters such as porosity are currently underway.

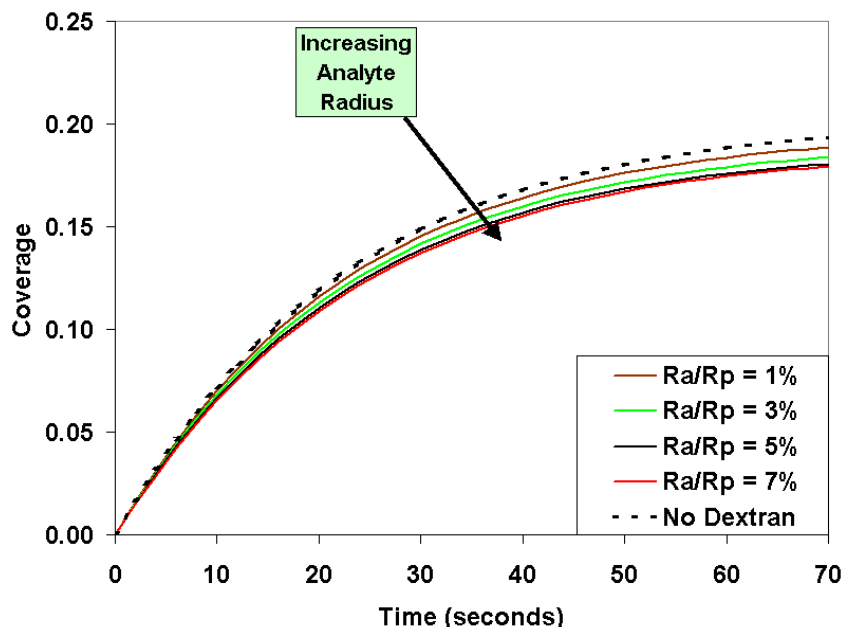


Figure 2.34: Change in the coverage curve with the ratio of analyte radius (R_a) to initial vertical cylindrical pore radius (R_p).

This calculation was performed using a constant receptor radius of 5 nm and a dextran thickness of 100 nm. The calculation was performed on the full 3D Biacore chip geometry.

Model data is available from U. Utah with various surface treatments. In their experiments, three different surface treatments were experimented with three different monoclonal antibody systems. Their results (Figure 2.35) showed that the behavior of the monoclonal antibody

systems is quite different on the different surfaces. For example, Table 2.4 lists the fitted association constants for the individual system. Note the wide variation in kinetic constants that has been observed

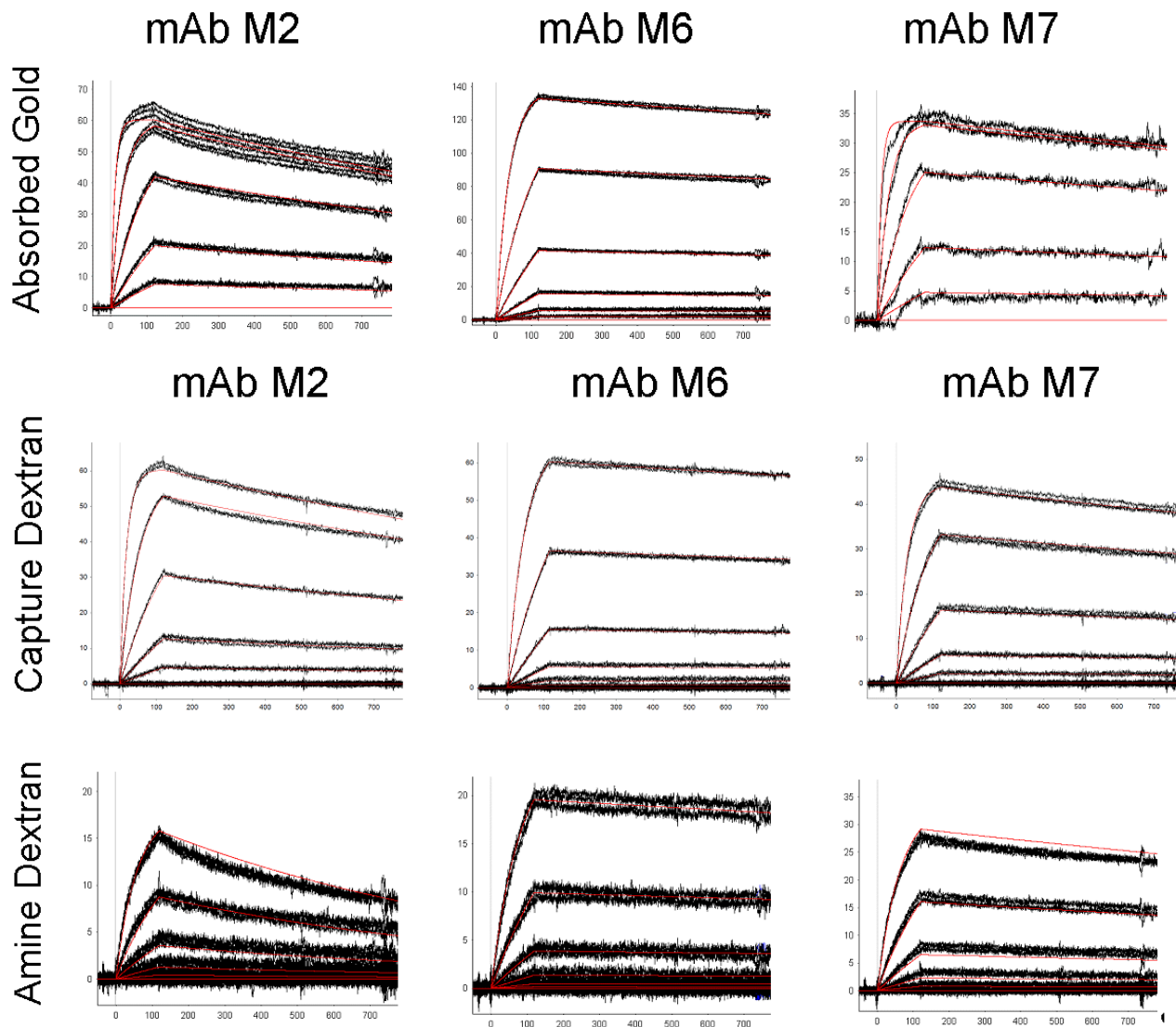


Figure 2.35: Illustration of the differing rates of adsorption on various monoclonal antibody systems and surfaces.

The three surfaces are bare gold, amine dextran, and capture dextran. The kinetic coefficients for each of the above graphs are given below in Table 2.4. Data were obtained using the Biacore-SPR device.

Table 2.4: Binding rate constants determined from SPR analysis of PSA/antibody interactions

	Association Rate (K_a)		
	mAb M2	mAb M6	mAb M7
Absorbed Gold	1.36E+06	1.36E+05	1.64E+06
Cature Dextran	8.05E+05	1.07E+05	5.22E+05
Amine Dextran	2.55E+05	6.51E+04	2.42E+05

2.1.13 Design of New Biacore Flow Cell (CFDRC and Univ. of Utah)

CFDRC worked with David Myszka in the design of a new flowcell for the Biacore instrument whose purpose is to examine biomolecular interactions in the presence of mass transport limited conditions. In their planned design, this is accomplished using a recess in the flow cell before and after the sensor patch. The team is carrying out full-fledged sensing simulations to assess the impact of the recess on flow, analyte transport and binding within the new flow cell. The flow channel domain (with the notch) is shown in Figure 2.37. Figure 2.37b shows the notch along with associated concentration profiles. The flow extends inside the notch, slowing down as it fills the notch and also driving small secondary vortices. Possible implications for analyte transport are twofold (a) there is a time-lag or slow down associated with the longer time taken to traverse the notch and (b) dead zones in the notch corners may pose potential lingering cross contamination problems.

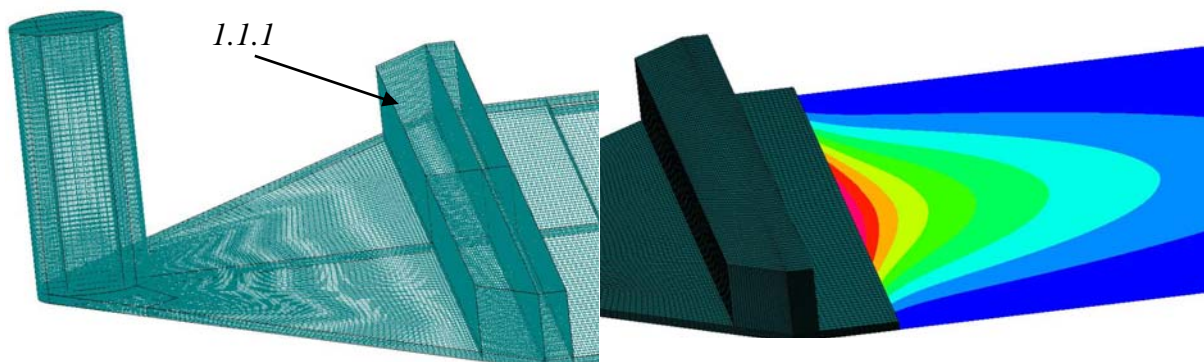


Figure 2.36: (a) Flow cell with notch. (b) IL-2 surface concentration in new flow cell.

2.1.14 Summary of Accomplishments: Model Development

During the course of this project, several simulation models have been developed and implemented in CFD-ACE+. Using these models, several physical phenomena have been studied in detailed. These studies directly benefited the project members, as well as academic and industry community at large. These accomplishments are discussed in detail next:

Models Developed

- M1. Particle dielectrophoresis models that include conventional DEP, traveling wave DEP, and electrorotation [29]
- M2. AC electrohydrodynamic phenomenon of electrothermal flows [16]
- M3. DC electroosmosis in systems with thick double layer [P23]
- M4. Slip boundary models for flow in hydrophobic microchannel systems [33, 34]
- M5. Models for EOF mobility variations as a function of pH for fused silica substrates[35]
- M6. Unit-cell based models for highly concentrated buffer solutions. Models predict following physical properties[P23]:
 - a. Electrophoretic mobility
 - b. Diffusion coefficient
 - c. Electrical conductivity
- M7. Integration of biochemistry models with particle DEP models [P45]
- M8. Joule heating[36]
- M9. Super LU solver for highly non-net neutral system[37]
- M10. Generalized surface chemistry models (beads and surfaces)[38]
- M11. Biochemistry database integrated with electrochemistry
- M12. Hydrogel models for surface biochemistry[30]
- M13. Least square-based engine for extraction of kinetic coefficients[38]
- M14. Rapid ANN based kinetic coefficient extraction algorithm (this has not been published yet)
- M15. Python based scripts to automate geometric generation for proteomic chips (these scripts are available from ESI-CFD, NA, Huntsville, AL)

The above models been validated with following analytical solutions:

1. Joule heating in parallel plate[16]
2. Particle DEP in periodic electrode array[P28]
3. Particle DEP in wedge shaped (conical) electrode system[P28]
4. Electrothermal flow in periodic electrode array[P25]

5. Ion transport near charged surface
6. EOF flow in arbitrary zeta potential and double layer thickness
7. All surface chemistry models were validated against the solutions in Lu, et al.[39]

After validation, the models have been used extensively to study various physical phenomena, and are applied in the design and development of devices. Table 2.5 summarizes these efforts.

Table 2.5: Physical phenomena, their models and examples of the application of the models.

	<i>Physical Phenomenon</i>	<i>Model Used</i>	<i>Device Designed</i>
1	Sample dispersion under non-uniform zeta potential	M3, M5	
2	Electrothermal flow	M2	Tunable laser cavity sensor (Fig 1.37)
3	Field Amplified Sample Stacking	M5, M6	Sample stacking device (Fig. 1.46, 1.52, 1.57, 2.4)
4	Slip at nanoscale	M4	
5	Conventional and traveling wave DEP	M1	Flow field fractionation devices
6	Nanoelectrokinetic phenomena	M3, M6	Nanofluidic devices
7	Transport of analytes in highly concentrated buffers	M6	
8	Bead based immunoassay	M10, M11	Notional immunoassay based sensors
9	Mass transport limitation in biosensor devices	M10, M11, M12, M15	Biacore biosensor
10	Effect of hydrogel layer (porous media flow) on proteomic chip performance	M10, M11, M12, M15	HTS proteomic chip

The models enabled rapid development and demonstration of the devices mentioned. In particular, the models were invaluable in screening design concepts (HTS and tunable laser cavity sensor) and in data analysis (Biacore biosensor). In the absence of the models, a similar end-point may, if at all, have been reached only after expensive and time-consuming iterations.

Design guidelines have been generated for engineers and scientists who work in this field. These are disseminated to the community via publication[40], workshops, conference presentation and

tutorials. Besides, the simulation models have been implemented in CFD-ACE+ Version 2002, 2003 and 2004, and have been successfully marketed.

Commercial Release of Developed Software Capabilities: Both the electrokinetic models and the biochemical assay models have also been fully integrated into the commercial CFD-ACE+ code, along with the development of associated GUI, user manuals and tutorial test cases.

Master Classes for Advanced CFD-ACE+ Users: Sample test cases have also been included based on these capabilities in the Master Classes (for advanced CFD-ACE+ users) for the biochemistry and the electrokinetic modules. These classes were taught at the Annual CFD-ACE+ Users Conference.

Multi-physics Courses: This material (test cases, tutorial examples, etc.) is also included in the following two Biotechnology industry-specific multiphysics courses being developed at CFDRC, which were offered starting November, 2001 in various locations around the country. The two courses offered dealt with: (a) design of biochemical assays in microfluidic systems, and (b) electrokinetic and electrochemistry applications in microfluidic systems. The objective of these courses was to facilitate rapid learning and confidence building in existing and new users of the software described here by discussing theoretical background (adequate physical models, data sources, and boundary conditions), optimal computational strategies, model set-up protocols of CFD-ACE+, and expected results (accuracy, speed, uncertainty).

2.2 Transport Enhancement: Electro-thermal Flow Modeling (UCSB)

AC electrokinetics was used to enhance microfluidic immuno-sensors, for example, immunoassays, in which a ligand immobilized on a microchannel wall specifically binds analyte flowing through the channel. These sensors can be limited in both response time and sensitivity by the diffusion of analyte to the sensing surface. The sensitivity and response of these heterogeneous immunoassays may be improved by using AC electrokinetically-driven microscale fluid motion to enhance antigen motion towards immobilized ligands. Specifically, the electrothermal effect is used to micro-stir analyte near the binding surface. Numerical simulations of antigen in a microchannel flow subjected to the electrothermal effect show that $6 V_{\text{rms}}$ applied to electrodes near a binding region can increase binding in the first few minutes by a factor of seven. The effectiveness of electrothermal stirring is a strong function of the Damköhler number. The greatest binding enhancement is possible for high Damköhler number, where the reaction is limited by diffusion. Based on these results, this technique is useful for a large variety of microfluidic sensors.

2.2.1 Background

Immunoassays, which rely on specific antigen-antibody binding for identification of proteins in a sample, have applications in both clinical laboratories for medical diagnostics and treatment monitoring, and in research laboratories for highly multiplexed testing, such as for biomarker identification. In these cases, throughput is a key consideration. One factor that can limit test duration is diffusion rate of analyte to the reporter. This is particularly true for high sensitivity ELISA tests [41]. An incubation step of minutes to hours allows diffusion-limited binding to reach detectable levels. Tests are often performed at centralized labs where, despite a long test duration, high throughput is achieved through robotics and highly parallel assays. However, if the assay could be moved from the centralized lab to the point of care, *real time* immunoassay-based diagnostics could be performed. In order for this to be achieved, the test must be faster, as well as more portable, while maintaining high sensitivity.

In response to the needs for increasing throughput, portability, and sensitivity, new formats for miniaturized immunoassays have developed dramatically in recent years. These include spotted microarrays, common for “gene chips”, and now used for “protein chips” (e.g. the *ProtoArray* from Invitrogen, Carlsbad, CA), and various forms of Lab-on-a-chip devices which can perform fluid processing and detection steps on a single chip [42]. Small length scales permit small sample sizes and shorter test times; on-chip sample preparation reduces fluid handling steps. Though greatly aided by their small length scales, these assays can still be limited in response by diffusion of the analyte to an immobilized ligand. In this report, a method where AC electrokinetics is used to enhance the performance of heterogeneous assays is presented. Here electrothermal forces are used to micro-stir the analyte near a functionalized surface, increasing the rate of transport to the surface. This addresses the need for faster assays by offering a tool that is adaptable to a wide variety of assay configurations and reduces the incubation time required to perform a specific test while maintaining its sensitivity.

2.2.2 AC Electrokinetic Phenomena

AC electrokinetics refers to induced particle or fluid motion resulting from externally applied AC electric fields. DC electrokinetics has been widely used for lab-on-a-chip applications such as electroosmotic pumping [43] and capillary gel electrophoresis for DNA fractionation [44],[45]. In contrast, AC electrokinetics has received significantly less attention. AC electrokinetics have the advantages of (1) largely avoiding electrolysis, and (2) operating at lower voltages (1~20 V), which is important for portable systems. AC electrokinetics can be classified into three broad areas: dielectrophoresis (DEP), electrothermal forces and AC electro-osmosis [16].

Dielectrophoresis takes advantage of a force arising from differences in polarizability between the particle and the fluid medium in the presence of a non-uniform electric field. DEP has been used to separate blood cells and to capture DNA molecules [46]; [47] provides an overview. However, since the DEP force scales with the cube of particle radius, its effectiveness for

manipulation of submicron molecules (such as 10 nm-scale antigen) is limited in devices with much larger length scales.

AC Electroosmosis arises when the tangential component of the electric field interacts with a field-induced double layer along a surface. A bioprocessor has been developed at UCLA [48] for the concentration of bioparticles including bacteria and λ -phage DNA. This device relies on the balance between electroosmotic flow and DEP force on suspended particles. In another application, Bazant and Squires [49] develop AC electroosmosis for pumping by inducing a double layer around metal posts that are asymmetric either in shape or in surface properties. AC Electroosmosis is only effective when there is a substantially deep induced double layer, that is, for low conductivity solutions and low applied field frequencies. For example, in an aqueous saline solution with an electrical conductivity of $\sigma = 2 \times 10^{-3}$ S/m, it is predicted that AC electroosmosis is not important for frequencies $f > 100$ kHz [50].

Transport enhancement of small proteins may be most successful through electrothermally driven flow (ETF). A non-uniform electric field produces uneven Joule heating of the fluid, which gives rise to nonuniformities in conductivity and permittivity. These interact with the electric field to generate flow, often in circulating patterns. Unintentionally-induced electrothermal flow in a traveling wave DEP cell-sorter was studied numerically [51], and found to be quite sensitive to thermal boundary conditions such as channel material, and applied temperature differential boundary conditions. Characteristic swirling flow patterns can be used to circulate suspended molecules past the binding region, thereby providing more binding opportunity for the suspended molecules.

2.2.3 Experimental Micro-PIV Measurements

With the objective of exploring two-dimensional fluid and particle motion in a non-uniform electric field, a cavity was fabricated with sidewall electrodes (Figure 2.37). The device was sandwiched between glass slides and filled with a solution of 0.05 M KCl and fluorescent polystyrene tracer particles. When the electrodes were driven at $V = 7 V_{\text{rms}}$ and $f = 200$ kHz, a fluid circulation pattern was observed. The two-color micron-resolution particle image velocimetry (μ -PIV) technique presented in Wang *et al.* [52] was used to measure fluid motion. These experiments are described in detail in [53] and are summarized here to provide motivation for the numerical simulations. The measured fluid velocity field is shown in Figure 2.38. The applied field induces a circulating flow, with a characteristic velocity of about 100 $\mu\text{m/s}$. When the driving voltage is varied between 3 - 7 V_{rms} , the flow pattern remains self similar, but the velocity magnitude varies with voltage to the 4th power, which is characteristic of electrothermal flow [16] (data not shown). The treatment of electrodes as isothermal is appropriate for electrodes of sufficient thickness relative to length.

Gradients in temperature produce gradients in electrical permittivity and conductivity in the fluid. For water, the dependence of electrical conductivity on temperature is $(1/\sigma) (\partial\sigma/\partial T) = +2\%$ and the dependence of electrical permittivity on temperature is $(1/\epsilon) (\partial\epsilon/\partial T) = -0.4\%$ per degree Kelvin [54]. These variations in electric properties produce gradients in charge density and perturb the electric field. Assuming the perturbed electric field is much smaller than the

applied electric field, and that advection of electric charge is small compared to conduction, the time-averaged electrothermal force per unit volume for a non-dispersive fluid can be written as [16]:

$$\frac{\mathbf{u}}{F_{ET}} = -0.5 \left[\left(\frac{\nabla \sigma}{\sigma} - \frac{\nabla \varepsilon}{\varepsilon} \right) g E \frac{\mathbf{u}}{1 + (\omega \tau)^2} + 0.5 |\mathbf{u}|^2 \nabla \varepsilon \right] \quad (2.43)$$

where $\tau = \varepsilon/\sigma$ is the charge relaxation time of the fluid medium and the incremental temperature-dependent changes are:

$$\nabla \varepsilon = \left(\frac{\partial \varepsilon}{\partial T} \right) \nabla T, \quad \nabla \sigma = \left(\frac{\partial \sigma}{\partial T} \right) \nabla T.$$

(2.44)

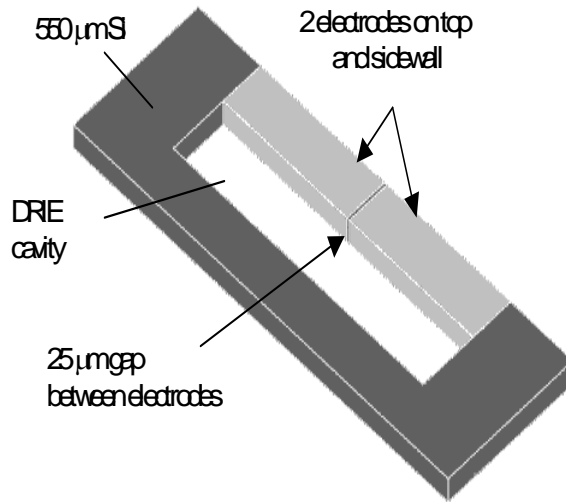


Figure 2.37: Test device used to measure 2D flow created by an inhomogeneous AC electric field.

The device is sandwiched between glass, and the cavity is filled with 0.05 M KCl solution seeded with fluorescent polystyrene particles. An AC driving signal produces an electric field in the fluid which generates fluid motion.

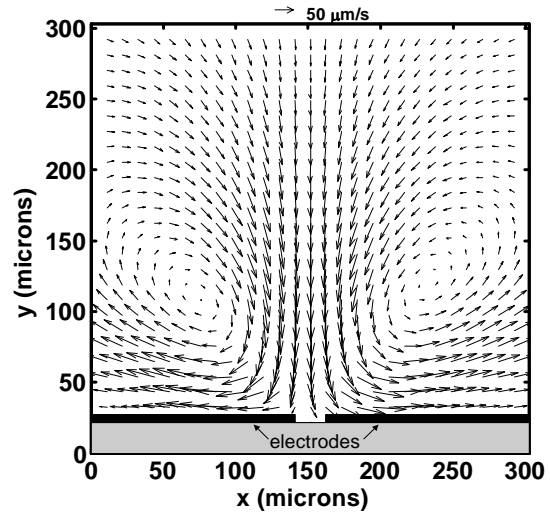


Figure 2.38: Fluid velocity field measured in the device shown in Figure 2.37. Images of the fluorescent particles moving in the fluid are captured at discrete times. Micro-Particle Image Velocimetry is used to determine particle velocity field. Data from two different size particle velocity fields are combined to estimate the fluid velocity. The electrodes are driven at 7 Vrms and 200 kHz. The AC field produces two counter-rotating vortices of characteristic velocity 100 $\mu\text{m/s}$.

The first term on the right hand side of Equation (2.43) is the Coulomb force, and is dominant at low frequencies, $\omega = 2\pi f$. The second term is the dielectric force, and is dominant at high frequencies. The crossover frequency scales inversely with the charge relaxation time of the fluid [16]. For example, an aqueous solution with conductivity $\sigma = 10^{-2}$ S/m has a crossover frequency around $f = 10$ MHz.

The electrothermal force shown in Equation (2.43) is a body force on the fluid. The motion of the fluid can be determined by solving the Stokes' equation for zero Reynolds number fluid flow, such that:

$$(2.45) \quad \begin{aligned} 0 &= -\nabla p + \mu \nabla^2 \mathbf{u} + F_{ET} \\ \nabla \cdot \mathbf{u} &= 0 \end{aligned}$$

where \mathbf{u} is the fluid velocity, p is the pressure in the fluid, and μ is the dynamic viscosity of the fluid. Figure 2.39 shows the resulting velocity field. With an applied voltage of $V = 5$ V_{rms}, the velocity of the electrothermal flow is on the order of 100 $\mu\text{m/s}$ and is characterized by a pair of counter rotating vortices. This velocity field, simulated for $V = 5$ V_{rms}, closely matches experimentally measured velocity for $V = 7$ V_{rms} (Figure 2.38). Out of plane heat transfer, unique to the thin experimental device, is not accounted for in the 2D model, and may cause this difference. The model was run with several grid resolutions, and determined to be grid-independent.

The total power consumption was calculated by integrating the Joule heating term, σE^2 , over the flow domain. For this particular model ($\sigma_w = 0.66$ S/m; applied potential $V = 5$ V_{rms} at $f = 200$ kHz), and for an out of plane cavity depth $d = 200$ μm , the predicted power dissipated is 4.3 mW.

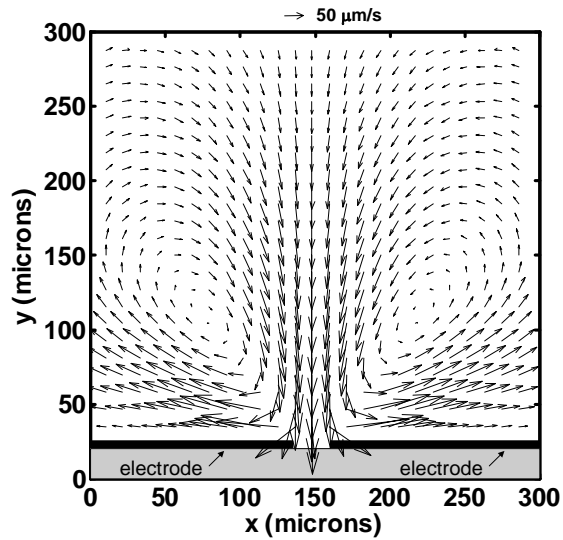


Figure 2.39: Simulation of electrothermally-driven fluid motion with an applied voltage of 5 Vrms.

The velocity of the electrothermally-driven flow is of order 100 $\mu\text{m/s}$ and is characterized by a pair of counter rotating vortices. This flow pattern matches the velocity field that was experimentally measured using micro-PIV (see Figure 2.38) with an applied voltage of 7 V_{rms} .

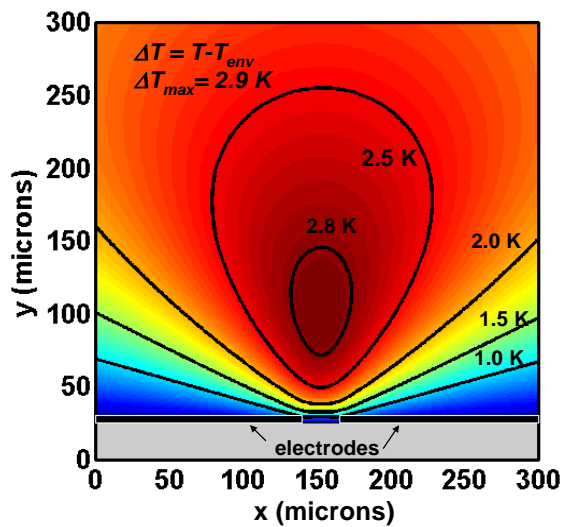


Figure 2.40: Numerical simulation of temperature distribution created by Joule heating.

The maximum temperature rise of 2.9 K. The sidewall electrodes are separated by 25 μm , and an applied voltage of 5 V_{rms} are applied to the electrodes.

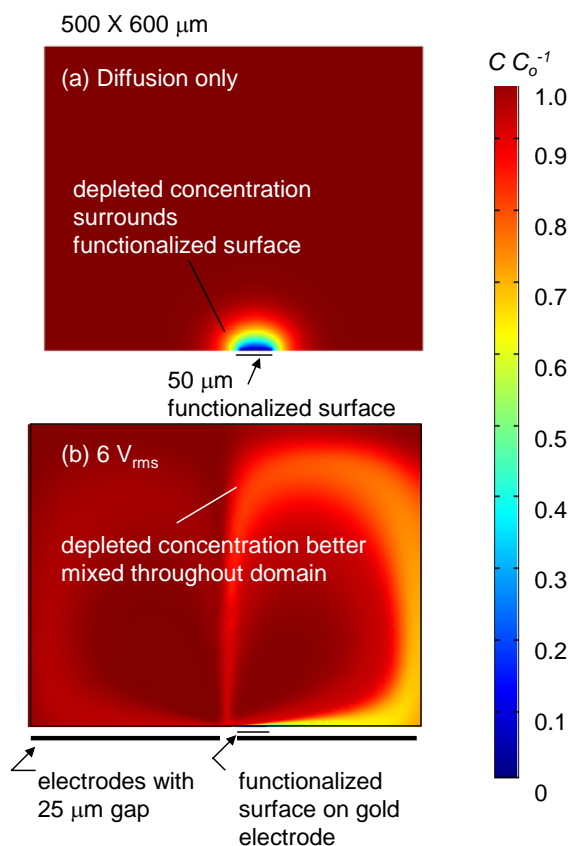


Figure 2.41: Simulation of concentration in a microcavity after 100 sec, subject to binding on the functionalized surface at the wall.

In (a), where mass transport is through diffusion only, a depleted cloud (black) surrounds the functionalized surface, indicating a depletion of analyte. In (b), electrothermal flow circulates the depleted cloud throughout the cavity, and circulates fresh analyte past the functionalized surface, yielding a higher effective concentration close to the functionalized surface.

2.2.4 Effect on Binding: Simulation of Microcavity

The highest flow velocities are predicted directly over the inside edges of the electrodes. Because of the high transport rate here, one expects this to be an optimum sensor location. The gold electrode surface provides a convenient surface for antibody immobilization through thiol linkers. Therefore, the effect of this flow pattern on the binding response of an assay in which antibody has been immobilized along a short length of the electrode near the electrode gap is investigated (Figure 2.41). For these microstirring enhanced binding simulations, a slightly higher potential is applied, 6 V_{rms} , than in the previous simulations (5 V_{rms}), for faster stirring.

The convective scalar equation describes the suspended concentration $c(x,y,t)$ of antigen within the microchannel:

$$\frac{\partial c}{\partial t} + \mathbf{u} \cdot \nabla c = D \nabla^2 c \quad (2.46)$$

where \bar{u} is the fluid velocity and D the diffusivity of the antigen. An initial concentration in the cavity c_o is depleted through binding at the wall. Following the model given by Myszka [55], the rate of binding at the wall for a first order reaction is $k_{on} c_w (R_T - B)$, where k_{on} is the on rate constant, R_T is the receptor concentration, B is the bound antigen concentration, and $c_w(x)$ is the suspended concentration of antigen along the wall. The rate of dissociation is $k_{off} B$, where k_{off} is the off rate constant. The time rate of change of antigen bound to the immobilized antibodies, $\partial B / \partial t$, is equal to the rate of association minus the rate of dissociation:

$$\frac{\partial B}{\partial t} = k_{on} c_w (R_T - B) - k_{off} B. \quad (2.47)$$

The rate of antigen binding to immobilized antibodies must be balanced by the diffusive flux of antigen at the binding surface, $y = 0$, such that:

$$\frac{\partial B}{\partial t} = D \left. \frac{\partial c}{\partial y} \right|_{y=0}. \quad (2.48)$$

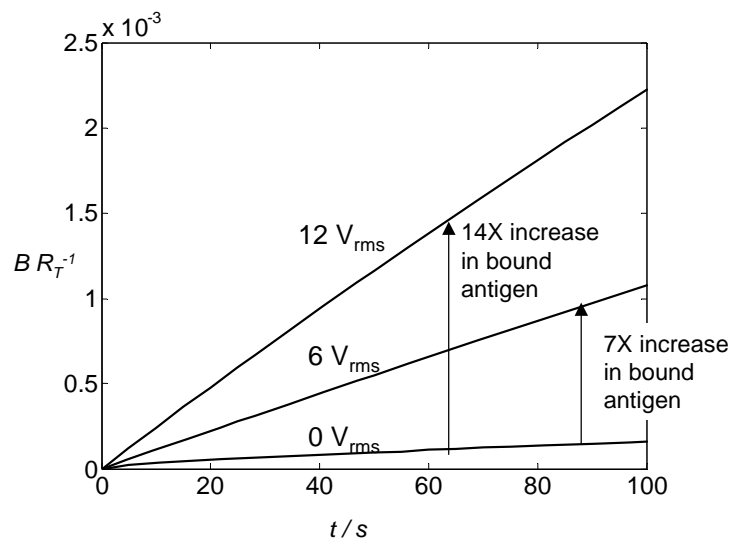


Figure 2.42 : Normalized binding curves for non-enhanced ($0 V_{rms}$) and electrothermally enhanced ($6 V_{rms}$, $12 V_{rms}$) transport.

B is the amount of analyte bound, which is normalized by the concentration of immobilized antibodies, R_T . The differences in the curves show an increase in binding rate which yields a factor of 7 higher binding for an applied voltage of $6 V_{rms}$ and a factor of 14 higher binding after 100 seconds for $12 V_{rms}$.

Equations (2.46), (2.47) and (2.48) are solved with an immobilized antibody concentration $R_T = 3.3 \times 10^{-11} \text{ M m}$ (i.e. 2×10^{16} molecules/ m^2) and an initial suspended antigen concentration of 10^{-10} M . Under the standard, passive format where there is no micro-stirring and binding locally depletes the suspended antigen concentration. Because diffusion is the only transport mechanism, the depleted region surrounding the sensor surface grows with time and reduces the rate of binding. When the functionalized surface is located near the center of an electrode pair (see Figure 2.44), and the electrodes are energized at $V = 6 V_{rms}$ and $f = 200 \text{ kHz}$, electrothermally-driven circulation redistributes the depleted concentration throughout the domain, and the sensor effectively sees higher suspended analyte concentration, resulting in a higher binding rate. Figure 2.43 shows that an applied voltage of $V = 6 V_{rms}$ produces a 7-fold increase in bound antigen compared to the $0 V_{rms}$ (passive) case. For an applied voltage of $V = 12 V_{rms}$, the increase jumps to 14-fold. The associated velocities ($u_{max} \sim 0.4 - 6 \text{ mm/s}$) vary with voltage to the 4th power, which is characteristic of electrothermal flow. These velocities are characteristic of other types of AC electrokinetic flows. For example, Bazant and Squires predict a 0.7 mm/s velocity generated by charge-induced AC electroosmosis [49]. To be conservative, this work will focus on the $6 V_{rms}$ case, for which the numerical simulations suggest a factor of 7.2 increase in binding rate. Higher binding rates may be achieved with higher voltages. The following parameters were used in the numerical simulation: solution conductivity $\sigma_w = 066 \text{ S m}^{-1}$; on and off rate constants $k_{on} = 10^6 \text{ M}^{-1} \text{ s}^{-1}$ and $k_{off} = 10^{-3} \text{ s}^{-1}$; immobilized receptor

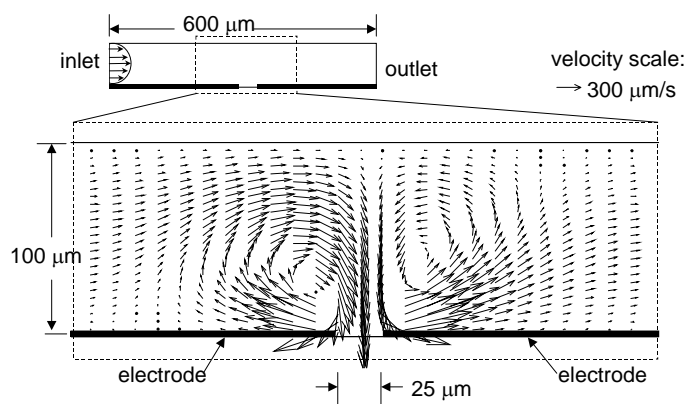


Figure 2.43 : Velocity field in microchannel showing effect of electrothermal force on channel flow.

Inlet mean velocity: $67 \mu\text{m/s}$. Electrothermal forces from a 6 V_{rms} electric field generate velocities which are on the order of $300 \mu\text{m/s}$.

concentration $R_T = 3.3 \times 10^{-11} \text{ M m}$; diffusivity $D = 10^{-11} \text{ m}^2\text{s}^{-1}$; initial suspended antigen concentration $c_o = 0.1 \text{ nM}$. The elements in the 2-D model are triangular with sizes ranging from $1 \mu\text{m}$ near the electrode gap to $20 \mu\text{m}$ far from the gap. At this mesh size, the solution was shown to be mesh-independent. The boundary condition at the functionalized surface (Eq. 2.48) is solved in a separate one dimensional domain and coupled to the 2D model. In order to facilitate the solution convergence, which can be difficult for low diffusivities, artificial streamline diffusion is added to the model. It was verified that this does not affect the results: the average bound concentration $\overline{B}(t = 100\text{s})$ agrees within 0.3% for cases with and without streamline diffusion (data not shown).

2.2.5 Flow-through Simulations

The team investigated the binding enhancement from micro-stirring in microchannels with pressure-driven flow. In these sensors, the pressure-driven flow continually exposes the sensor to fresh analyte, and so one does not expect that the binding enhancement through micro-stirring will be as significant as for non-pressure driven flow. The microchannel is also smaller in these flow-through simulations to better represent microscale flow-through channels (e.g. MEMS based) which often have smaller fluid volume than static immunoassays (eg. microarray). The channels are $100 \mu\text{m}$ in height, so the Damköhler number is reduced by a factor of 5, as compared with the same assay in the larger microcavity simulations. For these simulations, a parabolic velocity inlet boundary condition is prescribed. Electrothermal forces distort the parabolic flow around the electrode gap to produce a circulating flow as shown in Figure 2.43. For this case (average inlet velocity $u = 67 \mu\text{m/s}$; $V = 6 \text{ V}_{\text{rms}}$) the electrothermally generated velocity ($\sim 300 \mu\text{m/s}$) is large compared with the average base flow ($67 \mu\text{m/s}$). In the convection-

diffusion model, zero initial concentration is prescribed throughout the microchannel. A concentration of $c_o = 0.1$ nM is introduced at the inlet (left hand side) of the channel for $t > 0$. For the passive case, where there is no applied voltage, the base flow is parabolic, and analyte is transported downstream most rapidly at the channel center. This is shown in Figure 2.45a, where the highest concentrations of analyte extend through the center of the channel. When an electric potential is applied, the electrothermally-induced motion redirects the concentration profile (Figure 2.45b). The optimum position of the functionalized surface is near the leading edge of the downstream electrode.

In this case, where convective transport from pressure-driven flow through the microchannel is important, the Peclet number must be considered as well as the Damköhler number. The Peclet number is defined as $Pe = uhD^{-1}$, which is the ratio of convective to diffusive transport. Figure 2.45 shows the binding enhancement factor Be for $t = 100$ s, for various Peclet numbers, and as a function of Da . As in the non-flow-through format (Figure 2.46), the binding enhancement factor Be has a strong dependence on Da . In this flow-through case, however, there is an additional strong dependence on Pe . Figure 2.46 indicates that the binding enhancement factor Be is lower for larger Pe , that is, for faster flows. While electrothermal micro-stirring may not be able to increase reaction rates in channels with high flow rates, it may provide more efficient capture of antigen, thereby allowing reduced flow rates. In cases where a high flow rate has been required to achieve sufficiently high binding rates in a transport-limited regime, the addition of electrothermal stirring to the channel allows the flow rate to be reduced while maintaining the same high binding rate. This effectively reduces required sample volume.

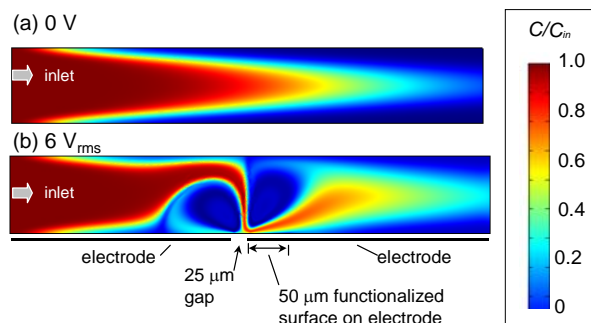


Figure 2.44: Concentration plots of electrothermally modified channel flow at $t = 5$ sec with applied voltages of (a) $0 V_{rms}$ and (b) $6 V_{rms}$.

With optimal size and placement of electrodes, the electrothermal eddies can be engineered to span the width of the channel, as is the case here, for a 100 micron channel. High flow rates and concentration gradients and therefore an increase in diffusive flux in the vertical direction directly over the inside edges of the downstream electrode indicate a favorable location of the functionalized surface.

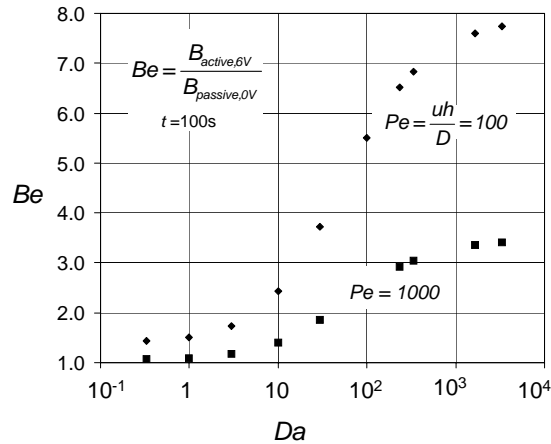


Figure 2.45: Simulation results show binding enhancement factor, Be , increases with increasing Damköhler number Da as in the static case, but decreases with increasing Peclet number, that is, faster pressure-driven flow.

2.2.6 Binding Enhancement Summary

Electrothermally-generated fluid motion was investigated experimentally and numerically. Experimental measurements of AC electrokinetically-driven velocity fields suggest that electrothermal forces are more important than AC electroosmosis for generation of fluid motion in high conductivity ($\sigma = 0.66$ S/m) buffers, which are applicable for many bioassays. Numerical simulations were conducted to predict electrothermally-generated fluid motion. The model predicts, for 5 V_{rms} applied, a temperature rise on the order of 2.9 K, which results in velocities on the order of 100 $\mu\text{m/s}$. The numerical model flow pattern closely matches experimental measurements with an applied voltage of $V = 7$ V_{rms}. The total power consumption of the electrothermal flow was 4.3 mW for a 200 μm deep cavity.

This model was used, together with a first order reaction model, to predict binding enhancement in heterogeneous reactions, for example, immunoassays. The model suggests that electrothermally-generated micro-stirring can increase the binding rate for non-flow-through assays, such as a microarray or microtiter plate, by a factor of seven, for 6 V_{rms} applied potential. A series of simulations with different parameters show that the binding enhancement depends strongly on the Damköhler number (Da). The binding rate is increased by a factor of 7.3 with electrothermal micro-stirring, for $Da = 10^4$. However, the binding rate is only increased by a factor of 3 for $Da \sim 100$, and little increase in binding rate is observed for $Da \sim 1$.

Electrothermally-generated micro-stirring can also improve binding rates for flow-through assays, for example in BioMEMS or lab-on-a-chip devices. In these cases, the binding enhancement factor depends on the Peclet number as well as the Damköhler number. Higher Peclet numbers, which correspond to higher flow rates, yield lower binding enhancement through electrothermal micro-stirring. For example, with a Damköhler number of 3×10^3 , and a

Peclet number of 100, a factor of nearly 8 improvement is possible. However, with a Peclet number of 1000, the expected improvement is reduced to a factor of about 3. The numerical simulations reported here indicate that electrothermal micro-stirring can be a useful technique for increasing binding rates in heterogeneous assays, particularly for diffusion-limited reactions.

2.3 Design and Fabrication of Electrokinetic Systems (ACLARA BioSciences)

2.3.1 Plastic Microfluidic Device Fabrication

The design and fabrication of microfluidic devices in plastic has tremendous potential impact in the commercial endeavor of pharmaceutical drug discovery, where such assays as multiplexed gene expression analysis, multiplexed proteomics experiments, and multiplexed enzyme assays have been pioneered by ACLARA and other fluidics companies and research groups to lower the cost, enhance the performance, and speed the process of these bioassays. To optimize such measurements, a wide range of designs and microfluidic configurations have been designed and prototyped. Plastic microfluidics also are beginning to have significant impact in clinical diagnostics, where disposability is a must and functional integration to save size, cost, and sample volume while improving reliability are paramount. The Stanford DARPA SIMBIOSYS Program pushed the frontiers of such parameters as microchannel aspect ratio, thus helping ACLARA to define the limits of low-cost plastic-to-plastic card technologies. The multiplexed assays mentioned above were also used to identify biological pathogens under DARPA BioFLIPS Program, a synergistic effort with the SIMBIOSYS Program.

In addition, ACLARA developed expertise and demonstrated technology in several key areas that contributed to rapid progress in the program:

- low-defect glass mastering of fluidic chips
- RIE-based mastering (using the Stanford facility, and commercial vendors) for variable aspect ratios and unique geometries
- prototyping of moderate volumes (5 – 50) of new designs
- thermal lamination of plastic-to-plastic chips to maintain channel definition
- pressure-sensitive adhesive channel sealing to enable in-chip reagent storage
- multilevel channel patterns for complex fluidic architectures
- integrated heaters for on-chip temperature control/monitoring
- integrated electrodes for on-chip drive of electrokinetic processes
- laser-induced fluorescence detection in plastic chips
- high-resolution CE separations in plastic microchannels
- highly multiplexed bioassays

2.3.2 Activities

Microfabrication of Masters with Complex Geometries using Silicon RIE, SU-8 Patterning, and Glass Etching.

ACLARA developed a new method of ITP (isotachopheresis, or “stacking”) for which simulated results have been reported [56]. This new ITP methodology offers high concentration ratios and simpler electrical control relative to conventional ITP. In general, these ITP designs include geometric features requiring higher aspect ratios, different angles, and better pattern resolution than attainable with wet etching of glass plates (ACLARA’s best-developed mastering technology). Further development of the RIE process was completed, and optimal etching parameters were selected to provide non-reentrant sidewall profiles with minimal sidewall roughness and micromasking defects. A total of six silicon masters were etched with the point concentrator design and evaluated. An SEM photo of a Si master and optical micrograph of a molded plastic part from such a master are shown in Figure 2.46.

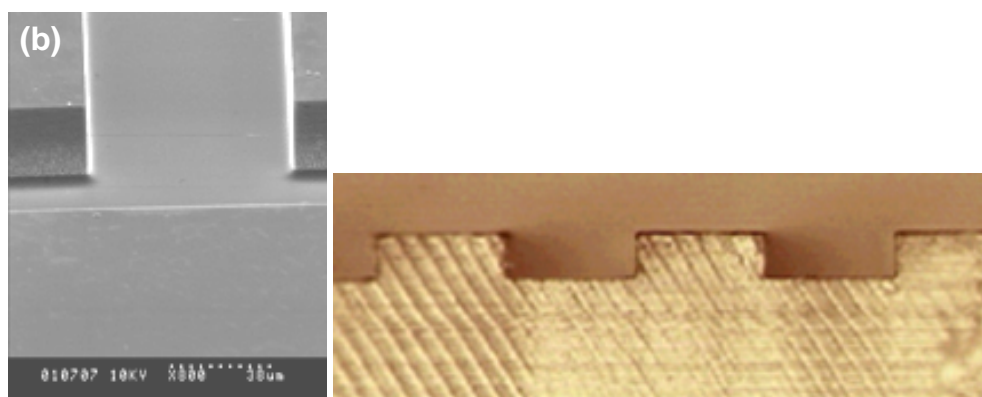


Figure 2.46: Left: SEM image showing reactive ion etched silicon master for point-concentrator device (close-up of a channel intersection).

Right: example of a plastic part molded with an electroform mold tool that was produced from a reactive ion etched silicon master, sawed to show the cross-section.

This particular stacking method, called the “point concentrator”, relies on a distortion of the electric field in the injection region caused by a geometrical feature protruding into the channel in the injection offset. The result of the distortion to the electrical field is an increased concentration of ionic species in the region of the point concentrator. The concentrated sample plug is then injected and separated, to achieve a higher observed signal-to-noise ratio at the detector. Point concentrator designs were fabricated with silicon RIE and SU-8 mastering processes. Both approaches produced channel dimensions with close to 1:1 aspect ratios.

Electroforms were successfully generated from these masters, and were used to mold plastic prototype cards.

A set of experiments designed to evaluate the anticipated signal enhancement relative to a control pattern with identical channel dimensions and lengths was performed. Separations were attempted using both 1) 40 nM fluorescein in 25 mM HEPES and 25 mM NaCl, and 2) four ACLARA eTag reporters[57] in 1x buffer with 12.5 mM MgCl₂. In both cases, a running buffer of 1% PEO in 25 mM HEPES was used, and the separation was detected 1 cm downstream from the injector. Injections were run using both pinch/pullback and floating/stacking scenarios, with results shown in Figure 2.47.

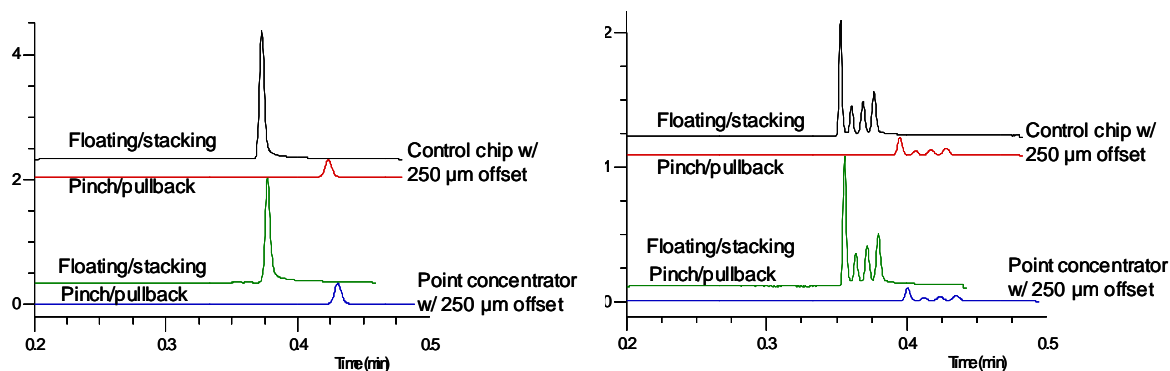


Figure 2.47: Left: Separation performance of point concentrator, compared to control chip without this feature, using fluorescein.

Right: Separation performance of point concentrator, compared to control chip without this feature, using 4 eTag reporters (molecular tags of different mobilities that are used in genomic and proteomic multiplexed assays).

Modeling results suggested that a signal enhancement of around 2x should be expected from the introduction of the point concentrator feature described above. However, for both fluorescein and eTag reporters, signal enhancement was insignificant relative to the control pattern. The likely cause of this failure has been identified as a rounded peak on the triangular point concentrator, which stems from the difficulty of microfabricating an arbitrarily sharp peak. Modeling results were achieved using an idealized triangular geometry, while the feature on the plastic device was slightly rounded at the feature peak. As shown in Figure 2.48, both the RIE and SU-8 processes resulted in slightly rounded point concentrators and channel corners. This is most likely due to the wet etching of the oxide mask in the RIE case, and the nature of photoresist development in the SU-8 case. Follow-up adjustments to the model suggested that the effect of the point concentrator diminishes rapidly as its geometry is rounded.

To improve point concentrator performance, efforts to improve the sharpness of the point concentrator feature were made. In particular, an isotropic glass etching approach was investigated. With isotropic etching, it is possible to obtain sharp convex corners with an appropriately designed etch mask. A variety of potential point concentrator features have been considered in addition to the simple triangular feature described above. A transparency photomask was created as the first step toward quickly mastering and evaluating a variety of potential point concentrator geometries. The most promising features from this mastering test were incorporated into a glass photomask. With improved mastering techniques, it is hoped that both the triangular point concentrator and other potential geometries can be demonstrated to result in the signal increase suggested by the original modeling results.

Figure 2.49 shows an example of a triangular point concentration feature as it appears in an AutoCAD design file, on a transparency photomask, and in the etched glass master. This triangular feature extends across the full width of the photomask line. Using these results, an optimized design with appropriate line widths was used to obtain a chrome photomask. A number of different designs were considered, including triangle-shaped features extending into the channel, conical sharp points in the center of the channel, and raised sharp ridges running perpendicular or parallel to the channel. Figure 2.50 shows an example of the sharp features possible with isotropic glass mastering techniques.

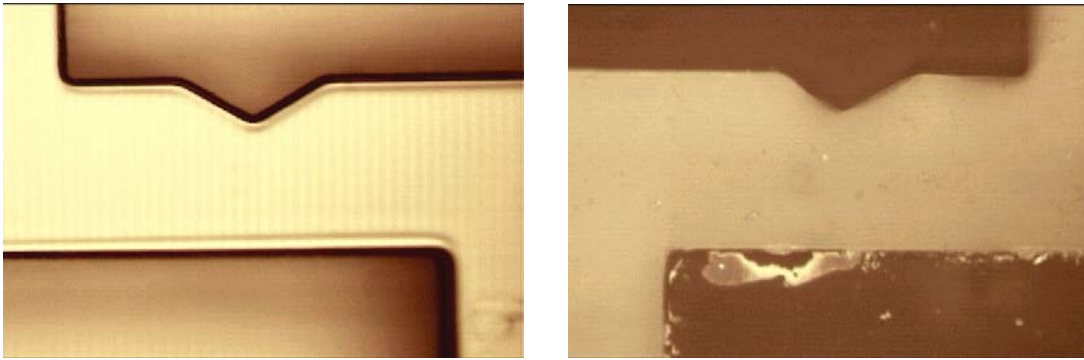


Figure 2.48: Electroform (left) and molded plastic part (right) from a reactive ion etched silicon master, showing rounded channel corners and point concentrator features.

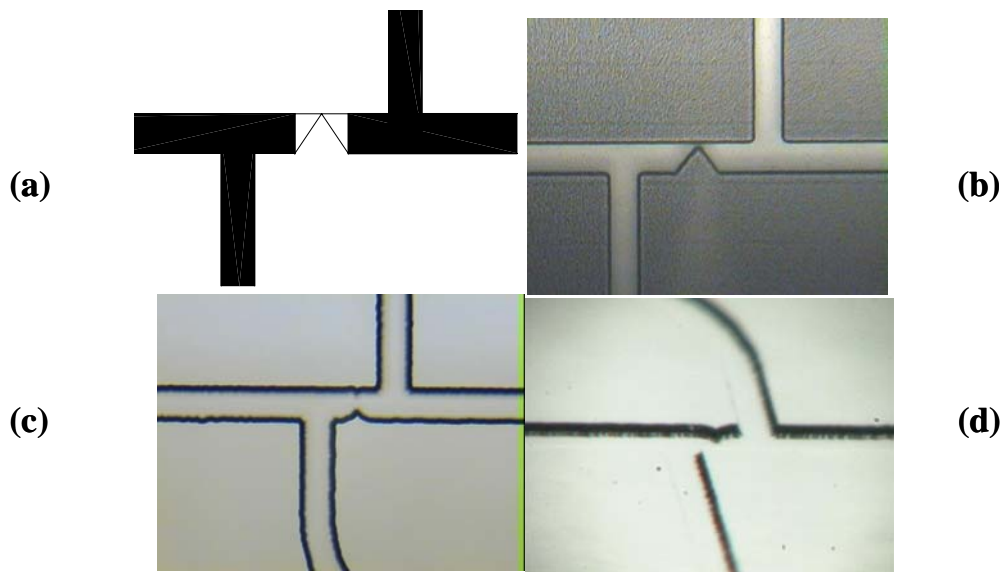


Figure 2.49: Triangular point concentration feature across full photomask line width.

(a) CAD layout; (b) transparency photomask; (c) optical micrograph of resultant etched glass master; (d) rotated perspective optical micrograph of etched glass master.

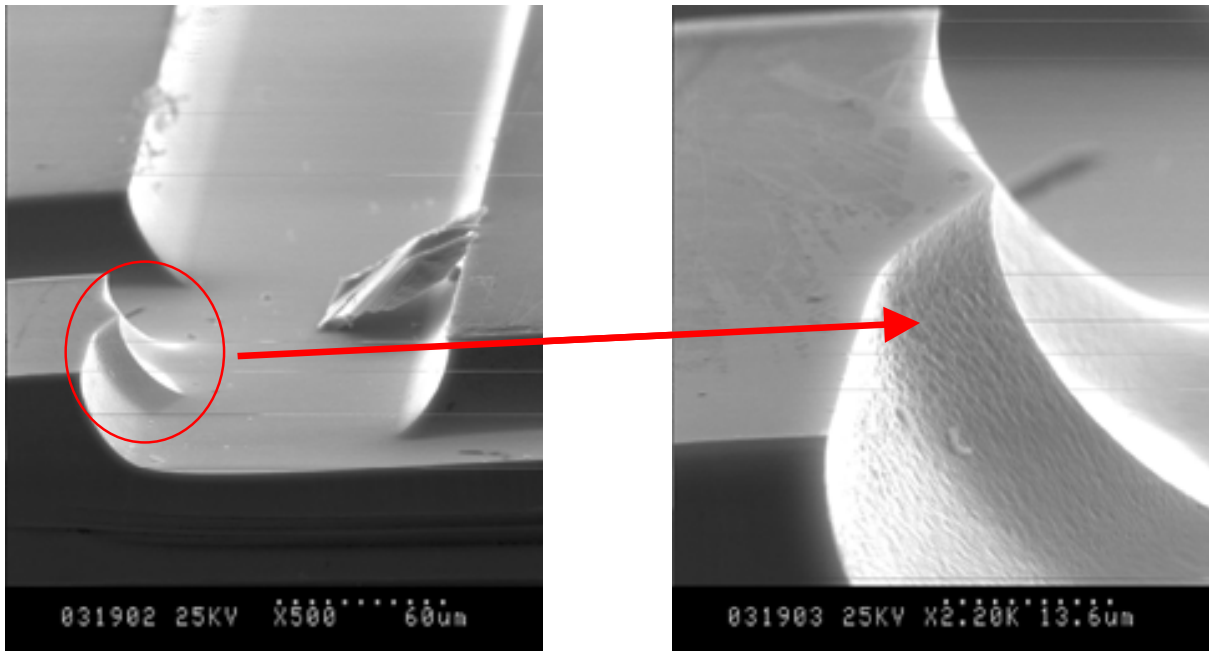


Figure 2.50: Scanning electron micrograph (SEM) showing features created with isotropic glass etching techniques.

Fabrication, inspection, and delivery of plastic microfluidic chips.

A number of plastic chips of the DS-1 and DS-2 chip designs were fabricated, inspected, and delivered to Stanford. The DS-2 design demonstrated the production of 20 μm -deep channels in thermoplastic, an advance over typical plastic fluidic cards. Table 2.6 shows the cards delivered to Stanford.

Table 2.6: Microfluidic card deliveries.

Card # (ETD)	Order	Suborder 1	Suborder 2	Suborder 3	Suborder 4	Suborder 5
Design						
DS1 Shallow <i>Depth: 20 μm</i> <i>Width: 50 and 200 μm</i>		15 (03/22/02)	16 (05/08/02)	15 (07/15/02)	15 (08/18/02)	
DS1 Deep <i>Depth: 40 μm</i> <i>Width: 90 and 240 μm</i>		15 (04/03/02)	13 (06/18/02)	15 (07/15/02)	15 (08/31/02)	
DS2 <i>Depth: 20 μm</i> <i>Width: 50 μm</i>		10 (04/26/02)	10 (07/01/02)	10 (07/30/02)	10 (09/15/02)	10 (09/30/02)

A second DS-2 electroform was obtained in May 2002, alleviating the defect problems created during the de-molding process by using the original DS-2 eform. Plastic cards were molded from this new eform and the image and profilometer measurement of the channel showed that the lip defect was eliminated, resulting in improved channel replication.

ACLARA developed a non-destructive evaluation technique for examining cross-sectional profiles of masters and electroforms. The process involves casting a layer of silicone rubber (polydimethyl siloxane, PDMS) onto the substrate bearing the microchannel features of interest; curing the rubber; peeling it from the substrate; cross-sectioning with a sharp metal blade; then examining the cross section by optical or electron microscopy. Figure 2.50 shows a channel cross sectional image obtained using this method.

2.3.3 Simulation and Demonstration of Point Concentrator Device (ACLARA BioSciences and CFD Research Corp.)

Improvement of the limits of detection in electrophoretic separations can enable more accurate and sensitive medical diagnostics, forensic measurements, and other bioassays with ever smaller sample quantities. The early diagnosis of cancer, for example, can be more effective as a consequence of the capability to detect fewer copies of a particular gene or a smaller concentration of key proteins.

In the floating-stacking approach, concentrations of salts and ionic mobilities are selected, and potentials on the various electrodes are controlled (including being left “floating”), such that isotachopheresis (ITP, or “stacking”) conditions are established. Simulations showed that this method can decrease sample loss and improve sensitivity relative to more standard methods.

The floating-stacking experiments were conducted on ACLARA's eTag™ reporter chemistries (a series of functionalized fluorescein molecules, each with a slightly different electrophoretic mobility; see [57]) to determine whether a large set of multiple species behave in the same manner as the single component simulation. The mixture consisted of 12 eTag reporters in 25 mM HEPES buffer used with a plastic chip with a standard double-T injector, 3-mm offset, and with the injection and separation voltage and timing given in Table 2.7 and Table 2.8.

Table 2.7: Injection voltage setup and timing for floating/stacking.

	V1	V2	V3	V4	Time (sec)
Inj	float	500	float	0	12
Sep	0	float	4200	float	

Table 2.8: “Pinch-and-pullback” voltage and timing setup.

	V1	V2	V3	V4	Time (sec)
Inj	0	500	0	0	12
Sep	0	380	4200	380	

In the resulting simulated electropherograms, each of the peak areas was integrated and the areas for the pinch-and-pullback method were compared to the floating/stacking method. These results are summarized in Table 2.9, and indicate that there is a near-uniformity in the ratio of areas for floating/stacking vs. pinch & pull-back for each of the 12 eTag reporters. This proves that the electrophoretic “loading” of the various eTag reporters is accomplished in a “democratic” fashion (without bias); i.e., the ratio of eTag reporter concentrations at the detector is the same as the ratio of concentrations in the original sample. This critical result is necessary for the floating/stacking technique to be broadly applicable. Note as well that the average enhancement of peak area is some 13x for the floating/stacking technique relative to “standard” injection methods.

Table 2.9: Comparison of areas of electrophoretic peaks resulting from pinch-&-pullback and floating/stacking injection and separation of 12 different eTag™ reporters.

eTag	Peak AREA <i>Pinch & pullback</i>	Peak AREA <i>Floating/stacking</i>	ratio <i>P&PB/FS</i>
1	15.2	210	13.8
2	3.1	43.7	13.9
3	2.8	37.0	13.3
4	3.3	41.7	12.8
5	5.2	72.6	13.9
6	11.4	145	12.6
7	2.4	37.3	15.5
8	5.4	72.7	13.4
9	18.0	213	11.8
10	8.6	106	12.3
11	14.9	169	11.3
12	11.5	127	11.0
average ±SD			13.0±1.3

Implementation of “Point Concentrator” Features for Improved Limits of Detection in Electrophoretic Analysis

Improvement of the limits of detection in electrophoretic separations offers the potential to allow more accurate medical diagnostics, forensic measurements, and other bioassays with ever smaller sample quantities.

Electrophoresis is commonly used to move ionic species for subsequent separation and detection. A common problem with this technique is that the concentration of species at the detector is often too small to detect with good signal-to-noise ratios. One previously explored method to address this problem is the technique of “stacking” (preconcentrating) sample species by changing the conductivity of the background electrolyte relative to that of the sample. ACLARA developed a new technique introducing local geometrical features (asperities) in the channels used to carry out electrophoresis, distorting the electric field in the injector’s offset region. These geometrical changes caused a local concentration buildup of the sample species to be detected. The geometrical features explored include the placement of triangular asperities in the offset region. The overall geometry and placement of electrodes used in the electrophoresis model is shown in Figures 2.51 and 2.52.

Figure 2.51: Channel and reservoir configuration utilized for point concentrator studies.

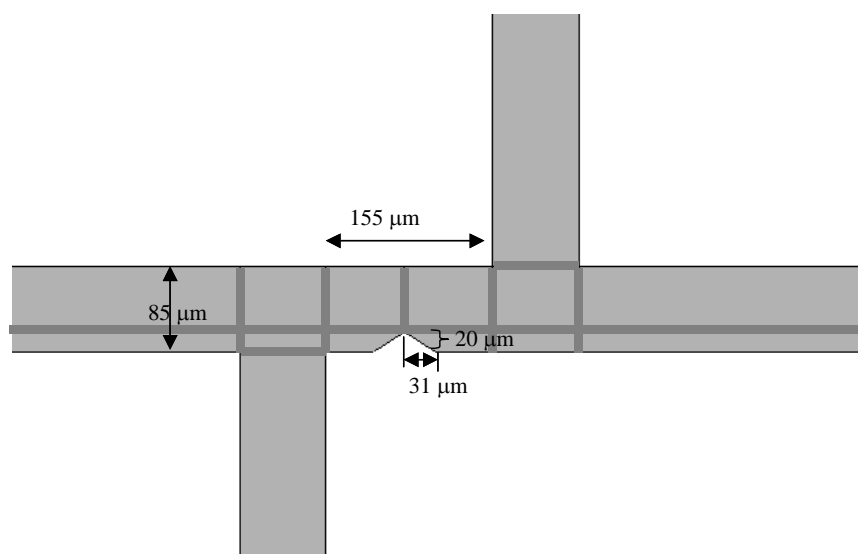
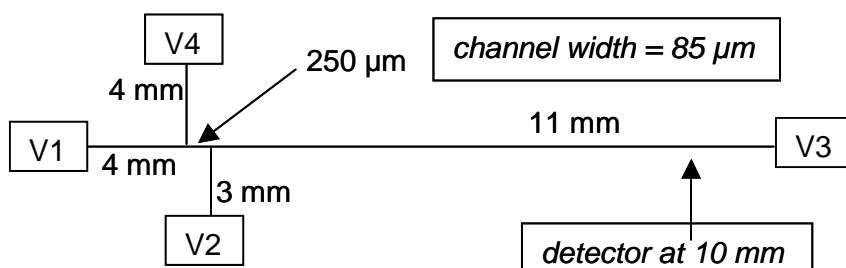


Figure 2.52: Channel geometry/layout for point-concentrator simulations, showing the 20 x 31 μm triangular asperity used to create local distortion of the electric field during the loading/injection process.

The sample channels were coated with 1% PEO; the running buffer was 25 mM HEPES at pH 7.38; the sample, placed in the well at electrode V4, consisted of 1 μM fluorescein in 25 mM HEPES + 25 mM NaCl. A geometrical configuration that was found to substantially increase the local electric field strength in the offset region is shown in Figure 2.52.

Simulation of the electrophoresis, consisting of injection followed by separation, was made using this geometry, and an electropherogram (Figure 2.53) was generated. This electropherogram was compared to an electropherogram obtained by using the same injection/separation scheme, but without a triangular step-shaped asperity in the channel. The comparisons were done with use of

the floating scheme described in Table 2.10, as well as with a pinch-and-pullback configuration described in Table 2.11.

Table 2.10: Timing/voltage conditions for floating/stacking operation of channel with triangular asperity in the region of the injector.

	V1	V2	V3	V4	Time (sec)	
Inj	float	500	float	float	0	12
Sep	0	float	700	float	float	25

Table 2.11: Timing/voltage conditions for pinch-and-pullback operation of channel with triangular asperity in the region of the injector.

	V1	V2	V3	V4	Time (sec)	
Inj	0	500	0	0	0	12
Sep	0	380	700	380	380	25

The electropherogram shows that the triangular asperity (“triangle”) gives about a 2x improvement in peak height relative to the result without the triangle in floating/stacking mode (float), and a much higher peak than the use of the triangular offset in pinch-&-pullback mode.

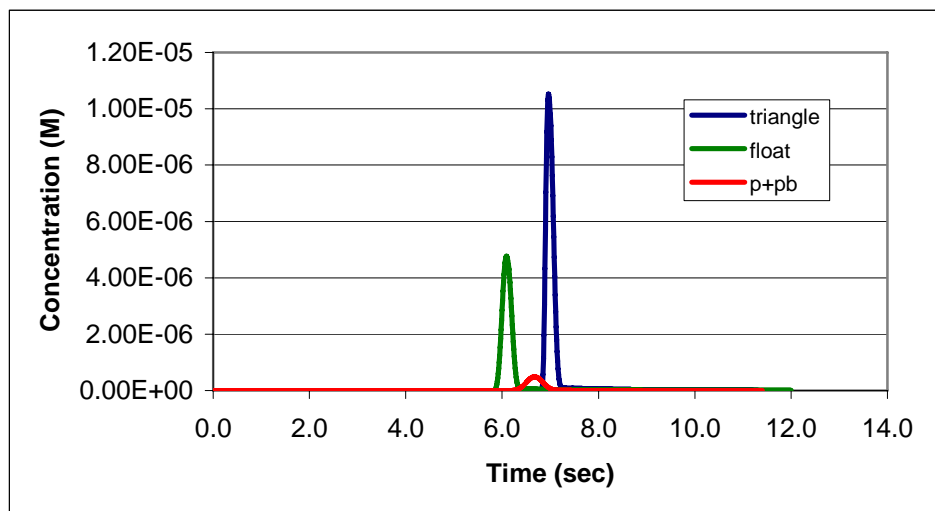


Figure 2.53: Comparison of single-species electropherogram using the geometrical configuration shown in Figure 5.3 (“triangle”) with a floating/stacking voltage/timing configuration; the same voltage/timing without the triangular asperity (“float”); and the use of the asperity with the “pinch-and-pullback” configuration.

2.4 Biokinetic Data Extraction for Array-Based Biosensors (University of Utah and CFD Research Corporation)

Interpreting binding kinetics from array-based biosensors requires new data analysis tools. The methods must be fast in order to interpret the large amounts of reaction data and accurate enough to account for transport effects that occur because of analyte concentration gradients created within large flow cells. In order to develop the appropriate analysis tools for array-based biosensors, the team focused the initial work on validating data extraction methods used for single flow cell systems. Three-dimensional CAD within CFD-ACE+ was used to generate a realistic construction of an operating BIACORE 2000 biosensor flow cell (see Figure 2.54). Binding data were then simulated under a variety of conditions, including increasing the association rate for the reaction from 10,000 to 30,000,000 $M^{-1}s^{-1}$ (see Figure 2.54).

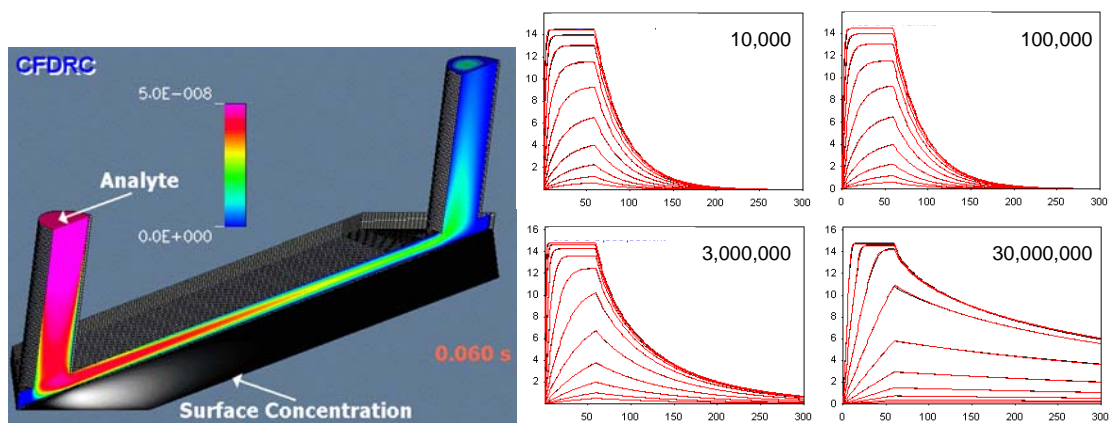


Figure 2.54: Left panel shows CFD-ACE+ simulation of three-dimensional flow, diffusion, and binding reaction within a single flow cell.

Right panel shows response data simulated for reactions with increasing association rates ($k_a = 1e4, 1e5, 3e6$ and $3e7 M^{-1}s^{-1}$) but with the same dissociation rate ($k_d = 0.03 s^{-1}$). The red lines represent a fit to the data using a fast two-compartment model to describe transport and binding.

These simulated data were then fit using a fast two-compartment model that describes transport of an analyte to the surface and a reversible binding reaction with an immobilized ligand. Excellent fits were obtained to the data simulated with the different association rate constants (as shown by an overlay of the red lines with the simulated data in Figure 2.54). More importantly, the association rate constants that were determined from the data extraction program correlated very well with the values used in the simulation. Furthermore, the analysis method also returned accurate values for the dissociation rate constant for all of the simulations ($k_d = \sim 0.03 s^{-1}$). The analysis program, which utilizes the simple two-compartment transport model, runs very quickly

and reduces analysis time by ~1000-fold for a comparable data set that is analyzed using the full three-dimensional fitting routine developed for this work using ACE+. Increased speed will be particularly important when it becomes common to analyze hundreds of data sets obtained from array-based biosensors.

In order to establish validated test reagents for molecule devices, the team characterized a number of molecule interaction systems ranging from antibody/antigen, drug/target and DNA/DNA interactions. Examples of data from some of the molecule systems the team characterized are illustrated in Figure 2.55. This work is critical for several reasons. Before initiating these studies, if someone wanted to test the performance of a device, there were no standardized systems to choose from. The team now has sets of commercially available reagents which can be used by the research community for systems evaluation and training. The team has published several papers describing the characterization of some of these systems and have utilized them for training and to conduct four global benchmark studies [58-63]. Having standardized systems also allowed us to develop and validate a novel approach to kinetic analysis

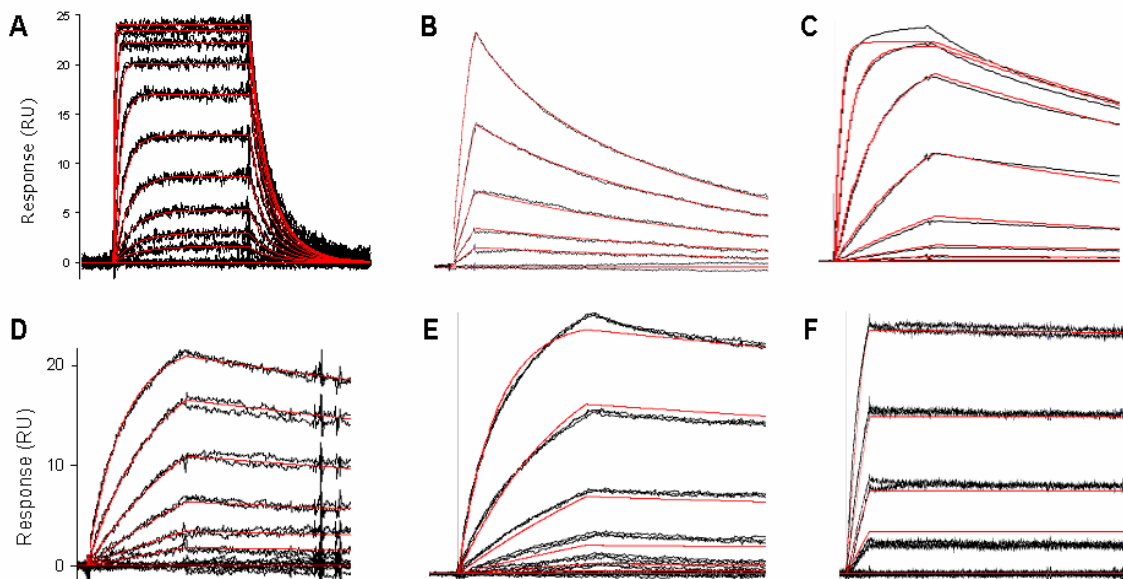


Figure 2.55: Example data sets for six validated molecular systems.

(A) DNSA/CAII, (B) BODIPY/CAII, (C) GFP/mAb, (D) FITC/mAb, (E) Protein A/mAb and (F) a DNA/DNA interaction. Black lines represent the responses collected from the biosensor. Red lines represent the global fit of each data set to a simple 1:1 interaction model.

that is called “kinetic titration”[64]. The data shown in Figure 2.56 are an example of a kinetic titration series carried out on an antibody/antigen system that had been validated previously. In a

kinetic titration assay analyte samples are tested from low to high concentration without regenerating the surface. Kinetic titrations allow one to collect the required concentration dependent binding information faster than traditional kinetic methods which require regenerations between binding cycles. Kinetic titrations will be particularly important as array – based biosensor technology is further developed, by allowing the user to analyze a wide range of kinetic systems without the need for regeneration. This new method also required the development new data fitting methods which have made available to the research community through CFDRC’s distribution of new software (Figure 2.56).

The research produced key innovations in the areas of electrokinetic stirring and electrothermal flow quantitation and physics. The group demonstrated that one can achieve an order of magnitude improvement in heterogeneous reactions using AC electrokinetic microstirring. It also demonstrated that micro-PIV can be used to quantify ac electrokinetic flow, and that use of the team’s 2 particle strategy can significantly reduce errors due to dielectrophoresis.

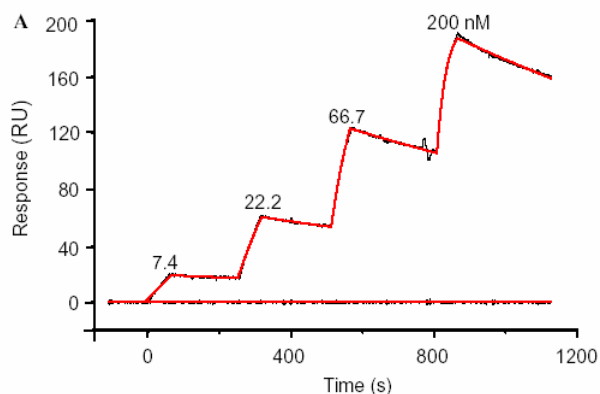


Figure 2.56: Left panel shows kinetic titration data for PSA/mAb interaction.

Right panel shows modeling program interface which was developed and used to fit titration data [64].

In addition to the team’s own interest in developing validated systems, the team’s work also received the attention of the National Institutes of Standards and Technology. Members of NIST saw a need for developing standardized reagents for molecular devices and the team worked closely with them to design, develop and validate a new system which they could mass produce and distribute. A bivalent mutant of the protein Barnase was designed which would produce a system with two binding sites containing different affinities (Figure 2.57). Having one system with two affinities makes this standardized system useful for testing a wider range of devices. The group is currently in the final stages of testing these reagents but have already used them to develop a novel method of assaying long association phases on Biacore biosensors [65].

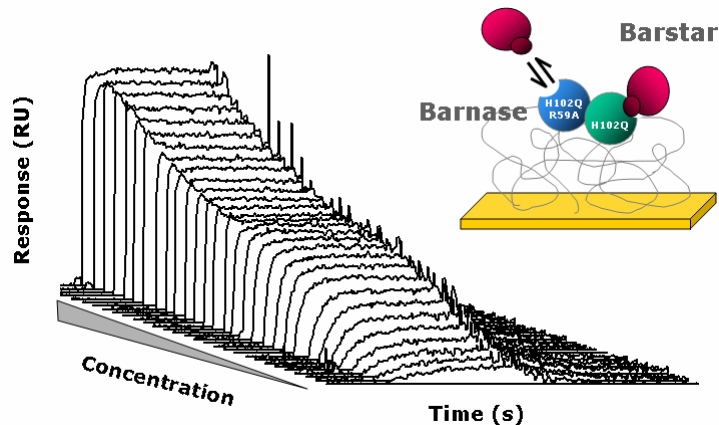


Figure 2.57: Concentration dependent binding profiles for the NIST bivalent Barnase/Barstar system.

Finally, the team's standardized reagents are being used by a number of instrument manufacturers to benchmark their own technology. Companies such as Lumera (Bothell, WA), BioRad (Hercules, CA), and Biacore Inc. (Piscataway NJ) requested and received reagents from the team for their developmental work. BioRad and BIACORE later adopted two of the systems produced by the team as training and test reagents that they distribute with their instruments. The experiments are currently using a validated antigen/mAb system to test the sensitivity of a new array based biosensor from Lumera. Therefore, the current efforts in developing and validating molecular reagents have impacted a wide area of research and will continue to do so in the future.

2.5 Electrokinetic Instability (Stanford University)

The team discovered, formulated, and created models of a new electrokinetic instability. This instability is in fact an electrohydrodynamic instability that occurs in the regime applicable to electrokinetic microsystems and which couples with electroosmotic flow to produce convective motion. This section describes some background on this work, presents sample experiments, introduces the current formulation of this problem, and presents modeling results and their comparison with experiments.

2.5.1 Importance of Electrokinetic Instability Flow Studies

Over the past decade there has been extensive research into the design of devices that perform chemical analyses in micro-fabricated fluidic channel structures. Often referred to as micro total analysis systems (μ TAS), these systems exhibit a mass transport regime that is often distinct from that of macro-scale flow devices. Many of these devices apply electrokinetic liquid-phase, bioanalytical techniques including capillary electrophoresis and isoelectric focusing, and often manipulate samples having poorly characterized or unknown electrical conductivities. As a result, conductivity mismatches often occur between the sample/reagent species and the

background electrolyte. In the presence of applied electric fields, conductivity gradients can induce electrohydrodynamic coupling, which can in turn generate complex, unstable flow-fields. Flows exhibiting these physics have been reported in the classical electrohydrodynamics literature (see for example, the seminal paper by Hoburg and Melcher, 1976 [66], and a later work by Baygents and Baldessari, 1998 [67]). In this section, flow instabilities due to electric field and conductivity gradients coupling in electrokinetic systems are reviewed. Electrokinetic flows are a subset of electrohydrodynamics characterized by the presence of an electrical double layer and regimes where transport due to molecular diffusion is important.

Although desirable for rapid-mixing applications, electrokinetic instabilities are unwanted in microfluidics applications such as sample injection, separation, and controlled diffusion-limited reaction processes where minimal sample dispersion is required. This motivates research toward a better understanding of the conditions necessary for the onset of electrokinetic flow instability.

2.5.2 Brief Review of Work Conducted as Part of the Current Project

In 2001 Oddy et al. (Stanford) [8] first reported observation of electrokinetic instability (EKI) in a microchannel system. These experiments were performed in 4-mm-long glass capillaries with rectangular cross sections, and the instabilities were in general of temporal nature [8]. In a slightly different geometry (microfluidic T-junction), Chen and Santiago also reported spatial amplification of disturbances which was later identified as convective instability [68, 69]. In all of these experiments, conductivity gradients were in the spanwise direction (perpendicular to the electric field), and there existed critical values of the applied streamwise electric field above which instabilities and significant stirring occurred.

Following these initial experimental observations, there has been a development of models for electrokinetic flow instabilities. Models are useful in predicting threshold conditions for instability onset as well as other flow features including coherent wave structures and mixing rate. Lin et al. [70] and Chen et al. [69] showed that a generalized EHD modeling framework (derived from the so-called “leaky dielectric” model first developed by Melcher and Taylor, 1969 [71]) can be used to describe both low-conductivity, non-diffuse charge dynamics of classical EHD, and the more recently reported flow instabilities of high-conductivity electrolyte in electrokinetic microsystems. Lin et al. [70] analyzed the temporal stability properties based on a two-ion model, comprising the conductivity transport equation along with the conservation of momentum and electromigration current. They showed that the model provided good qualitative and fair quantitative agreement with regard to the threshold electric fields and critical wavenumbers. Lin et al. [70] also presented non-linear simulations of their set of governing equations that capture the high Peclet (or the so-called electric Rayleigh) number stirring events observed in experiments. Using a convective framework, Chen et al. [69] showed that EKI could manifest itself convectively in the presence of a strong electroosmotic flow. In the latter analysis, EKI is modeled using a linearized, thin-layer limit of the Navier-Stokes equations coupled with conservation equations for electrical conductivity and current. The model reveals both convectively and absolutely unstable eigenmodes. More recently, Storey et al. [72] presented a depth-averaged version of the governing equations used by the Lin et al. model [70]. Their depth-

averaged model compared favorably with a complete three-dimensional model for thin channel geometries.

In the next two sections, salient results from these various studies are presented. A brief presentation of sample experimental results is followed by a depth-averaged model useful in predicting flow instabilities and computing dispersion in electrokinetic microfluidic systems.

2.5.3 Example Flow Visualizations and Experimental Results for Electrokinetic Flow Instabilities

Here are shown a few exemplary results from these experiments. The microchannel consisted of a borosilicate glass capillary (Wilmad-Labglass, NJ) with a rectangular cross-section. The channel was 4 mm long (in the x or streamwise direction), 1 mm wide (in the y or spanwise direction), and 0.1 mm deep (in the z or depth direction). Two buffer streams initially occupied the upper and lower halves of the microchannel resulting in a diffuse conductivity gradient along the spanwise, y -direction; an electric field was subsequently applied along the streamwise, x -direction. The conductivity of the buffer streams were 50 and 5 $\mu\text{S}/\text{cm}$, respectively, resulting in a conductivity ratio of $\gamma=10$. For flow visualization, an electrically neutral, heavy-molecular-weight dye (70kDalton) composed of a dextran-rhodamine B conjugate (Molecular Probes, OR) was added to the high conductivity buffer stream. The imposed electric potential initiated an electroosmotic flow in the channel and, for electric fields above a threshold value, electrokinetic instabilities.

Here are presented a few exemplary results from the current experiments. A schematic of the microchannel system used in many of the current parametric studies is shown in Figure 2.58 below. The microchannel consisted of a borosilicate glass capillary (Wilmad-Labglass, NJ) with a rectangular cross-section. The channel was 4 mm long (in the x or streamwise direction), 1 mm wide (in the y or spanwise direction), and 0.1 mm deep (in the z or depth direction). Two buffer streams initially occupied the upper and lower halves of the microchannel resulting in a diffuse conductivity gradient along the spanwise, y -direction; an electric field was subsequently applied along the streamwise, x -direction. The conductivity of the buffer streams were 50 and 5 $\mu\text{S}/\text{cm}$, respectively, resulting in a conductivity ratio of $\gamma=10$. For flow visualization, an electrically neutral, heavy-molecular-weight dye (70kDalton) composed of a dextran-rhodamine B conjugate (Molecular Probes, OR) was added to the high conductivity buffer stream. The imposed electric potential initiated an electroosmotic flow in the channel and, for electric fields above a threshold value, electrokinetic instabilities.

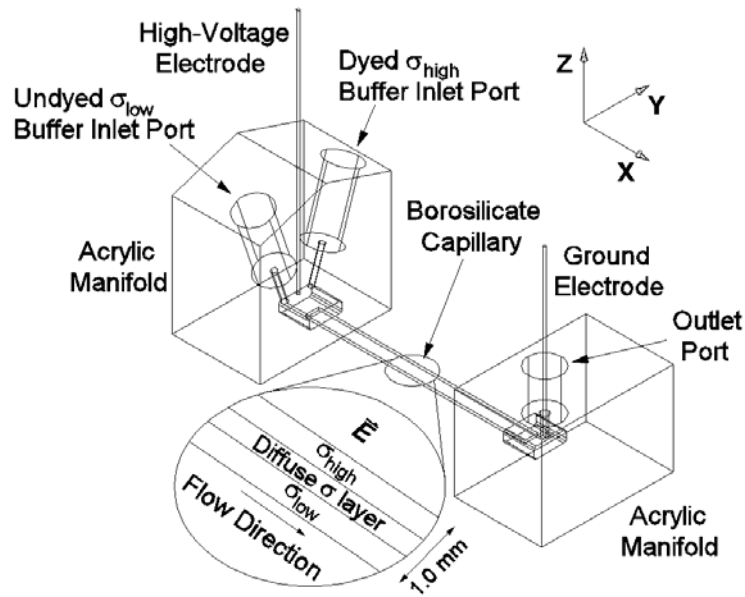


Figure 2.58: Schematic of the microchannel setup.

Two buffer solutions with differing electrical conductivities are advected through the microchannel using a syringe pump, resulting in a single buffer stream having a spanwise electrical conductivity gradient. Images were captured halfway between the inlet and outlet of the capillary. Fluid motions were observed using an inverted, epi-fluorescent microscope (Nikon TE300), 4x (NA 0.2) objective and a 0.6x demagnifying lens, resulting in an overall magnification of 2.4x. A CCD camera (CoolSnap fx, Roper Scientific Inc., AZ) with a 12-bit intensity digitization resolution recorded the images. Image signal-to-noise ratio SNR was improved by binning individual CCD pixels forming 4 x 4 super pixels having final dimensions of 26.8 x 26.8 μm in the image plane.

This experimental setup allowed for rapid change of parameters including the applied electric field; the characteristic width of the diffuse region between the two conductivity streams (an important initial condition); the location of imaging; and the ratio of conductivity of the two streams. The setup also allowed for rapid change between rectangular capillaries of a variety of sizes (with cross-section, inner dimensions ranging from 10 μm to 2 mm) and aspect ratios (varying from 1:1 to 10:1).

A representative set of images from experiments conducted at 1, 2, and 3 kV applied potentials are shown in Figure 2.59. The potentials were applied over a distance of 40 mm, such that they were equivalent to applied fields of 25,000, 50,000 and 75,000 V/m, respectively. In each case, the top figure of each series shows the initial, undisturbed interface between the dyed and undyed buffer streams in the channel ($t=0$). The successive images in each column show the temporal evolution of the imaged dye under a constant, DC potential. In this color scheme, blue corresponds to the undyed, low-conductivity stream, and red to the dyed high conductivity stream. For an applied field of 25,000 V/m, the interface was only slightly perturbed and only

slight fluctuations are apparent in the images captured at 4.0 s and 5.0 s. At the two higher applied voltages, the interface exhibited a rapidly-growing wave pattern within the first 1 s. The unstable fluid motion in the channel buckled the interface and proceeded to stretch and fold material lines. The transverse and fluctuating velocities associated with this unstable motion resulted in rapid mixing of the two streams. At the 75,000 V/m applied field, the channel reached a well-stirred state and with nearly-homogeneous concentration fields observable within 5 s.

A representative set of images from experiments conducted at 1, 2, and 3 kV applied potentials are shown in Figure 2.59. The potentials were applied over a distance of 40 mm, such that they were equivalent to applied fields of 25,000, 50,000 and 75,000 V/m, respectively. In each case, the top figure of each series shows the initial, undisturbed interface between the dyed and undyed buffer streams in the channel ($t=0$). The successive images in each column show the temporal evolution of the imaged dye under a constant, DC potential. In this color scheme, blue corresponds to the undyed, low-conductivity stream, and red to the dyed high conductivity stream. For an applied field of 25,000 V/m, the interface was only slightly perturbed and only slight fluctuations are apparent in the images captured at 4.0 s and 5.0 s. At the two higher applied voltages, the interface exhibited a rapidly-growing wave pattern within the first 1 s. The unstable fluid motion in the channel buckled the interface and proceeded to stretch and fold material lines. The transverse and fluctuating velocities associated with this unstable motion resulted in rapid mixing of the two streams. At the 75,000 V/m applied field, the channel reached a well-stirred state and with nearly-homogeneous concentration fields observable within 5 s.

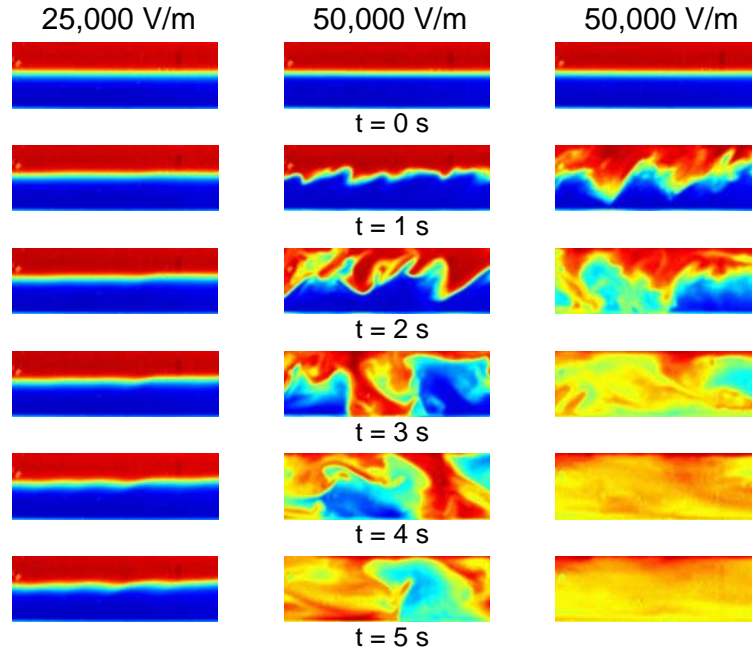


Figure 2.59: Sample images from the experiment, shown for applied fields of 25,000, 50,000, and 75,000 V/m, corresponding to the first, second, and third column.

Images obtained at various times are shown for each column. The electric field and bulk flow directions were from left to right. High voltage was applied as a Heaviside function at $t = 0$ s. Each image corresponds to a physical area 1 mm wide (y) and 3.6 mm long (x). The depth of the channel is $100 \mu\text{m}$ along the z -direction (into the page). Small amplitude waves at $t = 1$ s grew and led to rapid stirring of the initially distinct buffer streams. The instability stretched and folded material lines and, after about 4 s for the 75,000 V/m applied field, resulted in a well-stirred, relatively homogeneous dye concentration field. The time of the images in each row are shown in the figure.

The team demonstrated the electrokinetic instability in a variety of flow geometries including T-channels and X-intersections (see Figure 2.60). An example result from across-channel electrokinetic flow injection geometry is shown in Figure 2.60. The figure shows experiments in a 50 μm wide (20 micron deep) borosilicate microchip system from Micralyne (Alberta, Canada). On the left, is a sample image showing a stable flow when the two streams have the same conductivity. On the right, are two sample instantaneous images for the case where the center stream (from the west to east wells) conductivity is 100 times that of the background sheath stream from the north and south wells.

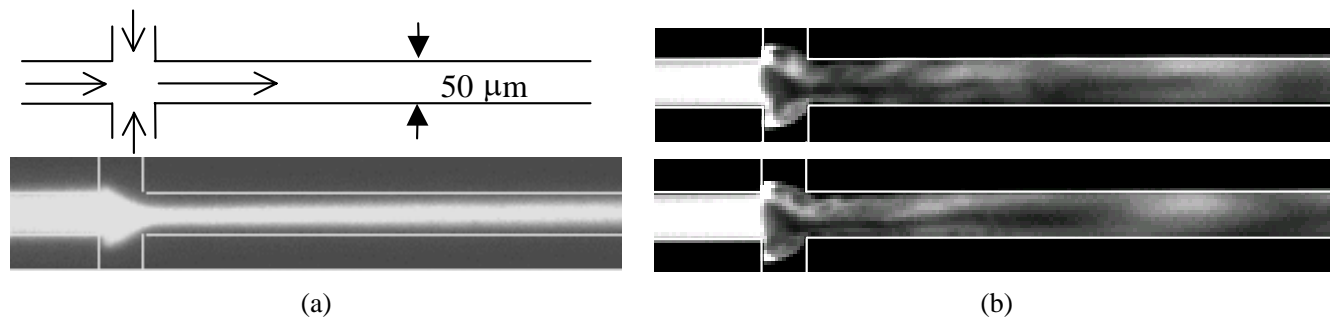


Figure 2.60: Electrokinetic instability during electrokinetic “pinching” at an X-intersection.

(a) Schematic and concentration field in the conductivity-matched condition, (b) Unstable, fluctuating concentration field for a sample conductivity 100 times smaller than the background electrolyte. Same DC voltage scheme but conductivity-gradient case results in rapid (0.1 sec scale) fluctuations in a region within a few channel widths from the intersection. A 180 V/cm field with $Re_L < 0.1$ is shown (smallest structures are $< 5 \mu\text{m}$).

It is also important to mention that, early on in the EKI research effort, the team designed and fabricated an EKI-based micromixer which successfully demonstrated rapid mixing for low Reynolds number flows. [1] The mixer design won the 2001 inventor’s award from the National Inventors Hall of Fame (established by the U.S. Patent Office), and a patent is pending. The device represents an enabling technology for binding and surface-hybridization assays of “Lab-on-a-Chip” systems.

2.5.4 Electrokinetic Flow Instability Model and Sample Results

A general theoretical formulation developed in Lin et al. [70] is presented here. Using these equations results from various linear analyses as well as nonlinear simulations, and assess their qualitative and quantitative agreements with experimental data are shown. As a conclusion of this section of this technical report, the Stanford group’s latest development in a depth-averaged framework suitable for the study of generalized electrokinetic flows in microchannels with thin channel geometry is introduced.

Below is a summary of the governing equations and the key parameters of interest in the Stanford studies. The equations of the Stanford model are derived from the conservation laws for a dilute, two-species electrolyte solution [73], and (with justification) a relaxation assumption to simplify the equations is adopted. The scaling analysis and derivations are discussed in detail in [70] and should not be repeated here. The (*dimensionless*) equations read

$$\frac{\partial \sigma}{\partial t} + \mathbf{v} \cdot \nabla \sigma = \frac{1}{Ra_e} \nabla^2 \sigma, \quad (2.49)$$

$$\nabla \cdot (\sigma \nabla \Phi) = 0, \quad (2.50)$$

$$\nabla^2 \Phi = -\rho_E, \quad (2.51)$$

$$\nabla \cdot \mathbf{v} = 0, \quad (2.52)$$

$$Re \left(\frac{\partial \mathbf{v}}{\partial t} + \mathbf{v} \cdot \nabla \mathbf{v} \right) = -\nabla p + \nabla^2 \mathbf{v} - \rho_E \nabla \Phi. \quad (2.53)$$

where σ is the conductivity, \mathbf{v} is the bulk fluid velocity, Φ is the electric field (which includes both applied and generated components), and p is pressure. The electric Rayleigh number (similar to a Peclet number) and the Reynolds number that arise from the nondimensionalization are defined as:

$$Ra_e \equiv \frac{U_{ev} H}{D}, \quad Re \equiv \frac{U_{ev} H}{\nu}. \quad (2.54)$$

Here H is half channel width, D is an effective diffusivity of the conductivity, and ν is the kinematic viscosity of the electrolyte solution (usually aqueous). The velocity U_{ev} , the so-called electroviscous velocity, is a velocity scale derived by setting equal the electric body force and the viscous force in the momentum equation [66, 69, 70] (Note: More discussions on these parameters can also be found in these literatures.)

First, a two-dimensional formulation is presented, where it is assumed that the flow exists only in the $x-y$ plane, and that there are no dynamics in the z -direction. This analysis will capture the basic physics of the instability mechanisms due to the conductivity gradient. A linear stability analysis is used to predict the regimes where it would be expected rapid mixing to occur. The base states are a diffused, spanwise conductivity profile $\sigma_o = \sigma_o(y)$ with a (high-to-low) conductivity ratio of 10, and a shear electroosmotic flow $u_o = u_o(y)$. Note that the spanwise dependence of the later was induced by that of the former *via* the dependence of zeta potential on conductivity. An assumption is that the disturbance is periodic in the x direction, and the growth of amplitude is exponential in time. The results are, for each streamwise wave number k and applied field E_o , a set of eigenvalues (the exponential growth rates), together with their respective eigenfunctions. Figure 2.61 is a contour plot of the growth rates of most unstable eigenfunction in the wave number-Rayleigh number (electric field) parameter space. The symbol s denotes the real and dimensional growth rate. The neutral stability curve is obtained by setting $s=0$. A threshold electric field is successfully captured from the minimal value of E_o on the neutral stability curve. As originally reported by Baygents and Baldessari [67], the team found that the inclusion of the diffusive term $\nabla^2 \sigma / Ra_e$ in equation (2.49) is crucial for the existence of the neutral stability curve.

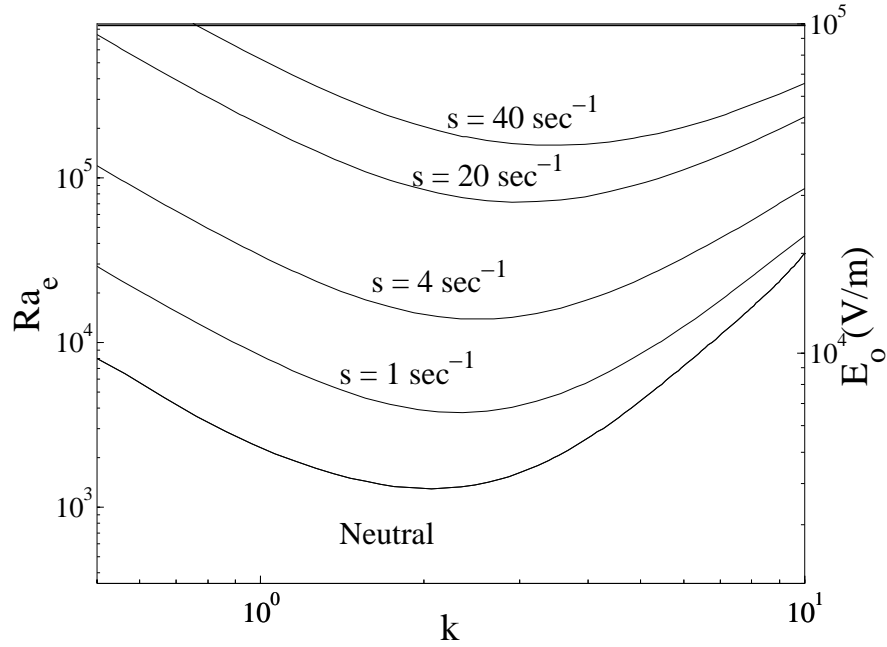


Figure 2.61: Contour plot of growth rates (s) versus wave number and Rayleigh number.

Dimensional applied electric field is provided on the right axis. For the case plotted here, the ratio of the conductivity between the two streams is 10.

In addition to the two-dimensional linear stability analysis presented above, the group also solved the full nonlinear governing equations numerically to capture the nonlinear evolution of the instability observed in the experiments. The initial conditions are the base states plus a small white noise perturbation. The solution details are documented in Lin et al. [70].

Figure 2.62 shows the nonlinear evolution of the simulated dye at various instances in time and for three different electric fields. The model reproduces many of the essential features observed in the experiments, including the shape and initial break-up dynamics of the interface, the transverse growth of a wave pattern in the interface, and the roll-up of scalar structures observed at later times. Note the similarity in the most unstable (and most apparent) wave number at later times between the simulation and experiments.

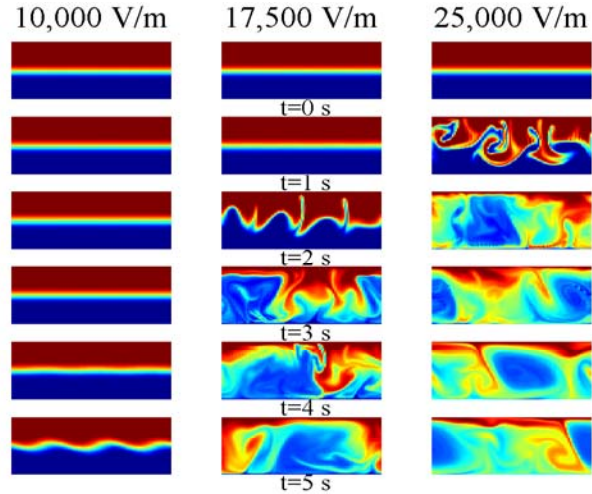


Figure 2.62: Snapshots of the simulated dye field at various instances in time for different driving electric fields.

In this color scheme red corresponds to the high conductivity buffer, and blue to the low one. Each column indicates a different applied field and the rows within each column present selected snapshots in time. The image corresponds to a physical domain of $3.6\text{mm} \times 1\text{mm}$. The time for noticeable waves to develop is decreased as the field is increased.

Despite similarities between wave number and the dynamics of the interface breakup, the threshold imposed fields from both the linear and nonlinear predictions are lower than those shown for the experiment in Figure 2.59. For example, compare the evolution of the dye at 25,000 V/m from the experiments (Figure 2.59, column 1) and the simulation (Figure 2.62, column 3). The results show that the simulation at 25,000 V/m predicts a well-stirred flow field in less than three seconds while experiments show that the flow is stable on the time-scale of the experiments. The simulation of 25,000 V/m is qualitatively similar to the experimental flow at 75,000 V/m (Figure 2.59, column 3). Despite the discrepancy in the magnitude of the applied field, the Stanford group simulation captures a threshold field and scalar features qualitatively similar to the experiment. In the following section possible causes for the under-prediction of the threshold electric field is addressed by including three-dimensional effects.

In comparison with the temporal instability analysis presented here (which is consistent with the experimentally observed instability in the previous section), Chen et al. [69] analyzed the instability in a convective framework which is consistent with the spatial growth that was observed in T-junction microfluidic channels. Among other contributions, the authors found that an important dimensionless group R_v , defined as the ratio of the electroviscous to electroosmotic velocity, is critical in demarcating the absolute/convective instability boundary. Interested readers are referred to [69].

The previous sections have been providing a two-dimensional framework which appears to capture the primary physics of the current flow. However, the primary flaw in that model is the two-dimensional assumption, for a channel with an aspect ratio of $\delta \equiv d/H = 0.1$, where d denotes the channel half-width. Such a thin channel geometry was also used in the experimental work of Chen et al.[68, 69]. In three dimensions, an EDL forms not only on the top and bottom walls of $y = \pm 1$, but also along the side walls ($z = \pm 1$), and strongly drives the flow due to the small depth of the channel. The three dimensional nature of a thin channel has the added dynamics that the fluid motion in the interior of the channel is directly coupled to the top and bottom wall boundary condition (determined in part by the local value of ion density).

In Lin et al. [70] the group presented 3D linear analysis and found that the predicted threshold field was an order-of-magnitude higher than that from the 2D linear analysis, in much closer agreement with the experimental observations. However, a depth-averaging approach is preferred since in general the 3D analysis (simulations) are computationally more expensive, and considering that the microchannels of Stanford's interest are "shallow" in the depth (z) direction. In Chen et al.[69] a depth-averaged analysis was performed on a set of linearized governing equations, and the resulted linear equation system was used for convective instability analysis. In Storey et al. [72] a more complete Hele-Shaw type of integrated momentum equation was used. Both models yielded favorable quantitative results when compared with experimental data.

Here the ideas that were first developed by Chen et al. [69] and Storey et al. [72] are extended and completed. A generalized, nonlinear depth-averaged model suitable for the study of electrokinetic microchannel flows with thin channel geometries is developed. It is accomplished this through a complete asymptotic analysis of the full three-dimensional equations based on a smallness parameter which is the channel cross-sectional aspect ratio δ . Stanford's general methodology follows a combined lubrication (for the momentum equations) and Taylor-Aris (for the convective-diffusion of the conductivity field) approach. Without presenting the details of the derivation, the final equations are:

$$\frac{\partial \bar{\sigma}}{\partial t} + \bar{\mathbf{u}} \cdot \nabla_H \bar{\sigma} = \frac{1}{Ra_e} \left\{ \nabla_H^2 \bar{\sigma} + \frac{2}{105} Ra_e^2 \delta^2 \nabla_H \cdot [\bar{\mathbf{U}}(\bar{\mathbf{U}} \cdot \nabla_H \bar{\sigma})] \right\}, \quad (2.55)$$

$$\nabla_H \cdot (\bar{\sigma} \nabla_H \bar{\Phi}) = 0, \quad (2.56)$$

$$\nabla_H \cdot \bar{\mathbf{u}} = 0, \quad (2.57)$$

$$Re \delta^2 \left(\frac{\partial \bar{\mathbf{u}}}{\partial t} + \bar{\mathbf{u}} \cdot \nabla_H \bar{\mathbf{u}} \right) = -\nabla_H \bar{p} + \nabla_H^2 \bar{\Phi} \nabla_H \bar{\Phi} - 3\bar{\mathbf{U}} + \delta^2 \nabla_H^2 \bar{\mathbf{u}}. \quad (2.58)$$

Here the overbar denotes a depth-averaged quantity, the operator ∇_H denotes the in-plane gradient (to distinguish from the full three-dimensional gradient), and $\bar{\mathbf{U}} \equiv \bar{\mathbf{u}} - \mathbf{u}_o$ is the

difference between the total depth-averaged velocity and the electroosmotic velocity. The main contributions of this new equation set are the Taylor-dispersion-type term in the conductivity equation, and the Darcy-Brinkman-Forchheimer (DBF) type of momentum equation which is of second-order consistency in δ [69, 74]. Preliminary results in the assessment of the validity and accuracy of the model are presented.

Figure 2.63 compares the linear stability results for growth rate of disturbances versus wave number at a single Rayleigh number of $Ra_e = 5,000$. Linear analyses is performed using the following three models: 1. The linear integrated momentum equations used by Storey et al. [72]; 2. The linearized three-dimensional equations[70]; and 3. The depth-averaged DBF formulation presented here. Note that at the linear regime the Taylor dispersion in Equation (2.55) drops as a higher-order term, and the only difference between the models are within the momentum equations. It is found that all three models are in good agreement for wave numbers below about 4. However, when compared with the more accurate three-dimensional analysis, the DBF momentum equation provides significantly better results at higher wave numbers than the lower-order, integrated momentum approximation.

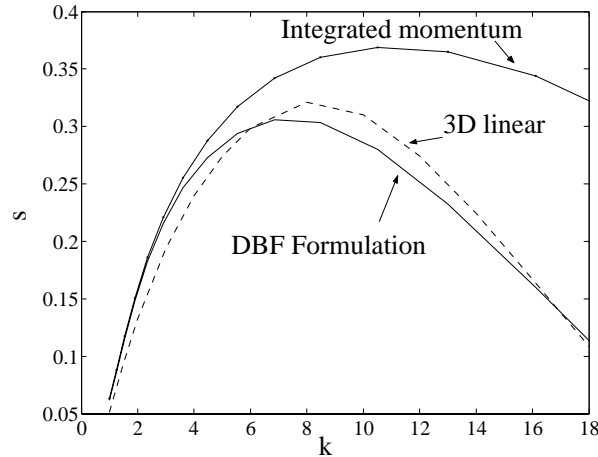


Figure 2.63: Comparison of growth rates of disturbances as predicted by three models.

Shown here are the real part of the growth rates versus the wave number for $Ra_e = 5,000$ as computed with the DBF momentum equation presented here, the integrated momentum equation (δ^0 approximation [72]), and the three-dimensional equation set. The DBF formulation represents in-plane viscous stresses that quench unphysical high wave number growth and is in agreement with the three-dimensional result.

The characteristics of the DBF momentum equations also make it more advantageous to use in nonlinear simulations when compared with the integrated momentum equation. In particular, the inclusion of in-plane diffusion $\delta^2 \nabla_H^2 \bar{\mathbf{u}}$ preserves a mathematical structure similar to the original Navier-Stokes equations, and enables reproduction of boundary effects (*e.g.*, at $y = \pm 1$ walls) that are not captured by lower-order approximations. This will be discussed further in future

work, and here are simply shown some sample results of the full nonlinear, depth-averaged simulations with Equations (2.55-2.58). That is, a model with the combined effects of Taylor dispersion and the DBF momentum equation. The team tries to reproduce the experimental image presented in Figure 2.59 at the two lower voltages (25,000 and 50,000 V/m), the result is shown in Figure 2.64. Again the model reproduces essential features observed in the experiments such as fastest growing wave numbers and the growth rates of the interface disturbance amplitude. However, note that the computations are now at exactly the same field strength as those applied in the experiments (as opposed to the unnaturally low fields used for comparison with the simple 2D model results of Figure 2.62). Future work will also include the application of the model to different flow configurations such as those used in field amplified sample stacking (FASS).

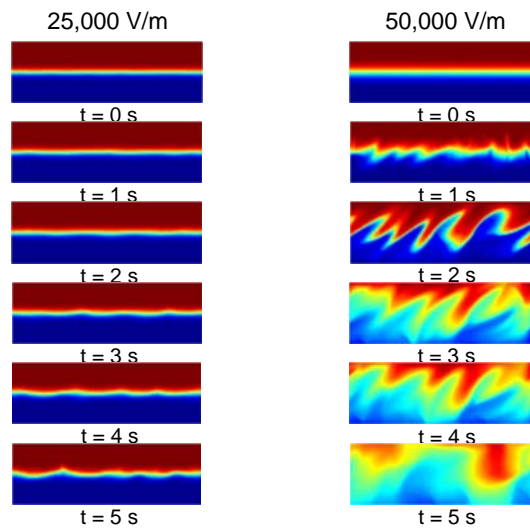


Figure 2.64: Nonlinear simulation of the depth-averaged equation system.

This model includes the combined effects of the Taylor dispersion and the DBF momentum equation. In the strongly nonlinear regime the Taylor dispersion acts as an extra smoothing mechanism. The results compare favorably with the experimental data presented in Figure 2.62.

As shown in Figure 2.64 above, the depth-averaged, non-linear model of EKI quantitatively the threshold field for the instability as a function of conductivity ratio. The model also qualitatively captures the development of the concentration field and dispersion dynamics.

2.5.5 Summary of Electrokinetic Instability Research

Experimental, numerical, and analytical results that explain the basic mechanisms behind an electrokinetic mixing phenomenon observed in microfluidic channels have been presented; this

was a major result and accomplishment of this project. The group developed analysis and computations based on various sets of assumptions for electrokinetic flows in a long, thin channel with a transverse conductivity gradient. The models developed here are able to predict general trends in the data, as well as many of the qualitative and quantitative aspects of the observed flow field.

The models presented in this work are useful in optimization studies, as parameter space can be spanned in simulations more quickly than in the laboratory. Work described by Oddy et al. [75] has demonstrated that oscillatory electric field can potentially drive even more vigorous mixing. The models presented here can be used to optimize the form of the forcing function, to design the shape of a micromixer, and to develop optimal control strategies for both micro-mixing and the suppression of instabilities.

This work has had a significant impact on the microfluidics communities. For example, the Stanford group's first three papers in this area [69, 70, 76] have already been referenced by other journal articles over 150 times.

2.6 Slip Flow Investigation (UCSB)

In addition to binding enhancement, a significant amount of time was spent investigating slip flow. The team developed a simple two-phase continuum model which predicts the Navier boundary condition as a function of thickness of gaseous bubbles formed at a microchannel surface. The results predict a slip length of 0.9 microns for a 18 nano-meter thick bubble layer. The resulting model is also in agreement with measurements of Zhu & Granick [34], and consistent with atomic force microscope measurements of bubble formation by Tyrell and Attard[1]. The group is devising experiments to test the validity of the simple experimental model, and to develop more complicated models describing the non-homogeneous characteristics of the velocity flow field.

Prior measurements with micron-resolution particle image velocimetry (μ -PIV) have shown an apparent fluid slip for de-ionized water flowing through 30 x 300 micron channels that are coated with hydrophobic octadecyltrichlorosilane (OTS). Figure 2.65 compares the experimental velocity profiles for flow near the wall of a clean hydrophilic microchannel (squares) and for flow near the wall of a hydrophobic microchannel (triangles). For a hydrophobic channel, the results show fluid slip near the wall of approximately 8.5% of the free stream velocity. Assuming Navier's hypothesis ($v_{\text{slip}} = \beta (dv/dy)_{\text{wall}}$) as the appropriate boundary condition at the wall, the measured slip corresponds to a slip length, β , of approximately 0.9 μm . The mechanism for the generation of apparent fluid slip is unknown. Ruckenstein and Rajora (1983) suggest that fluid slip may develop from entrained and soluble gases forming a gap near the wall. Recently, Tyrell and Attard [1] imaged, with an atomic force microscope, a hydrophobic glass surface submerged in water. Their results showed the presence of pancake shaped, 20 to 30 nm thick nano-bubbles completely covering the surface. In addition, they showed that the hydrophobic surface acts as a nucleation site pulling dissolved gasses out of solution. Within 10 to 20 minutes after scraping the surface clean, the surface was once again completely covered with nano-bubbles. To determine if dissolved gasses could generate the apparent fluid slip in Figure 2.65,

flow between to infinite parallel plates assuming nano-bubbles form an effective air gap near the wall is examined analytically. From this simple one dimensional model one can calculate the bubble height or air gap required to generate measured slip lengths assuming Navier’s hypothesis effectively describes a thin air gap at the surface.

For two phase flow between two infinite parallel plates with a thin air gap of thickness, δ , at the wall and a fluid layer of thickness $2h$, the solution for the velocity in the water phase assuming Stokes flow for both phases, no stress at the centerline, continuity of stress and velocity at the air-water interface, and no-slip at the air-wall interface is:

$$u_w = \frac{1}{2\mu_w} \left(\frac{dP}{dx} \right)_w \left[y^2 - 2hy - 2 \frac{\mu_w}{\mu_a} h\delta - \frac{\mu_w}{\mu_a} \delta^2 \right] \quad (2.59)$$

where μ_a and μ_w are the viscosity of air and water respectively, $(-dp/dx)$ is the pressure drop and $y=0$ at the air water interface. Assuming Navier’s hypothesis effectively describes the thin air gap at the wall the velocity is set equal to the slip length times the shear rate and obtain an equation for the air gap thickness (or bubble height) as a function of plate separation and slip length :

$$\frac{\delta^2}{2} + h\delta - \frac{\mu_a}{\mu_w} \beta h = 0 \quad (2.60)$$

Velocity profiles

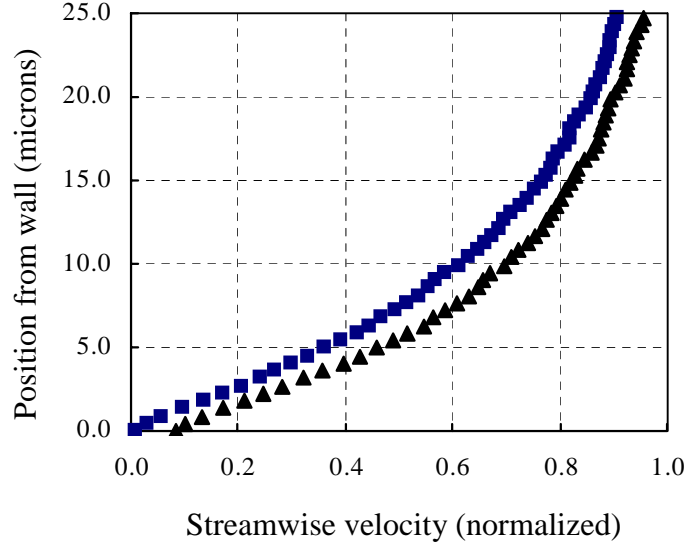


Figure 2.65: Velocity profiles for water flow through a hydrophilic (squares, no-slip) and a hydrophobic (triangles, slip) microchannel.

Figure 2.66 shows the air gap thickness required for a given plate separation to generate a given slip length. As the plate separation decreases the slip length generated by a given air gap thickness increases. At very small separations the slip length is strongly dependent on the air gap thickness. In this work is calculated a slip length of 0.92 μm . With 30 μm channels, this yields a required air gap thickness of approximately 18nm. This thickness is consistent with the measured bubble heights of Tyrrell and Attard[1]. In addition, when surfaces are hydrophobic, Zhu and Granick [34] calculated slip lengths of approximately 2.5 μm for a 20nm separation. The corresponding bubble height of ~20nm is consistent with the required bubble height in this work and the measured values of Tyrrell and Attard [1]. Pit et. al. [77] calculate a slip length of approximately 400nm for a 190 μm separation, which would require a bubble height of 9nm. These results suggest that the measured apparent fluid slip may develop as a result of dissolved or entrained gasses accumulating on hydrophobic surfaces. However, the assumption that the air gap/nano-bubble may be modeled as a continuum is quite coarse. At a lengthscale less than approximately 100nm, the gas is rarefied and slip would occur at the gas/wall interface. From kinetic theory of gasses the velocity at the wall would be:

$$u_{slip} = \frac{4-2\sigma}{3\sigma} \lambda \left[\frac{du}{dy} \right]_{y=wall} \quad (2.61)$$

where σ is the accommodation coefficient and λ is the mean free path of the gas. Solving the two phase flow problem described above but with the kinetic theory boundary condition yields the following equation for the slip length as a function of air gap height and plate separation:

$$\beta = \frac{1}{2h} \left(\frac{\mu_l}{\mu_g} \right) \left[\delta^2 + 2(\varepsilon + h)\delta + 2\varepsilon h \right] \quad (2.62)$$

where $\varepsilon = \lambda(4-2\sigma)/(3\sigma)$. For the experimental conditions of Tretheway and Meinhart [33], Zhu and Granick [34], or Pit et. al. [77], Equation (2.62) produces slip lengths substantially larger than those observed experimentally. In fact, the experimentally measured slip lengths are not obtainable with Equation (2.62). Thus, the assumption that the nano-bubbles completely cover the surface and form a thin air gap along the wall is incorrect. However, if the bubbles partially cover the surface, the wall would contain regions of slip and no-slip. Since the nano-bubble dimensions of Tyrrell and Attard [1] are substantially smaller than the current measurement area, the measured velocities average the regions of slip and no-slip. Thus, the appropriate equation for the slip length as a function of bubble height and plate separation is:

$$\beta = \frac{x\mu_l (2\varepsilon\delta + \delta^2 + 2(\varepsilon + \delta)h)}{\mu_g (2h - xh)} \quad (2.63)$$

here x is the surface fraction covered with bubbles. From this equation is calculated a required surface fraction covered with bubbles equal to .25 to produced the measured slip length of 0.9 μm for flow through a microchannel. This low surface coverage may lead to substantial regions of no-slip. Further examination of the velocity profiles combined to form Figure 2.67 verifies this idea. Figure 2.67 shows the velocity profiles along the length of the channel. In different

regions, the velocity profiles show varying degrees of slip. This may indicate regions of high and low bubble surface concentration.

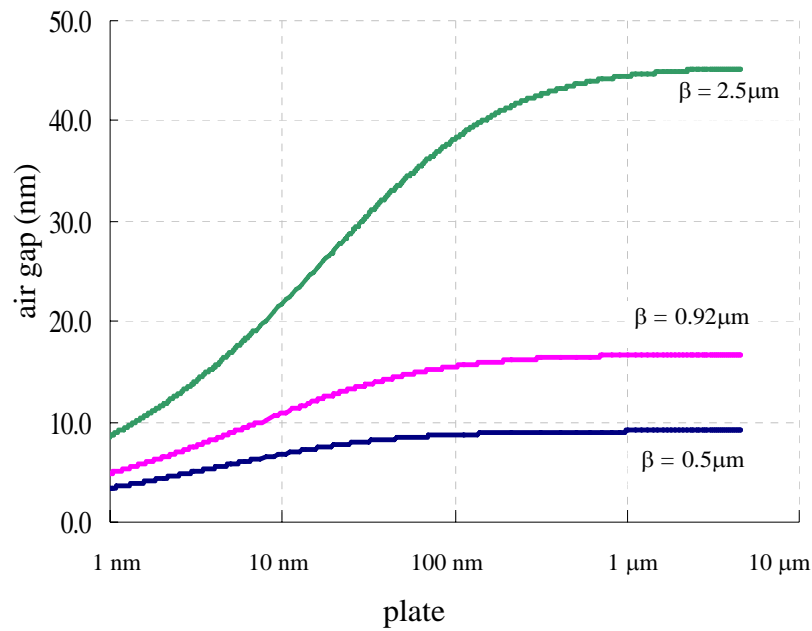


Figure 2.66: Solutions of Eq. (2), showing air gap thickness as a function of plate separation to produce a given slip length.

Measured slip lengths for various researchers are indicated. Tyrrell and Attard[1] measured bubble heights of 20-30 nm.

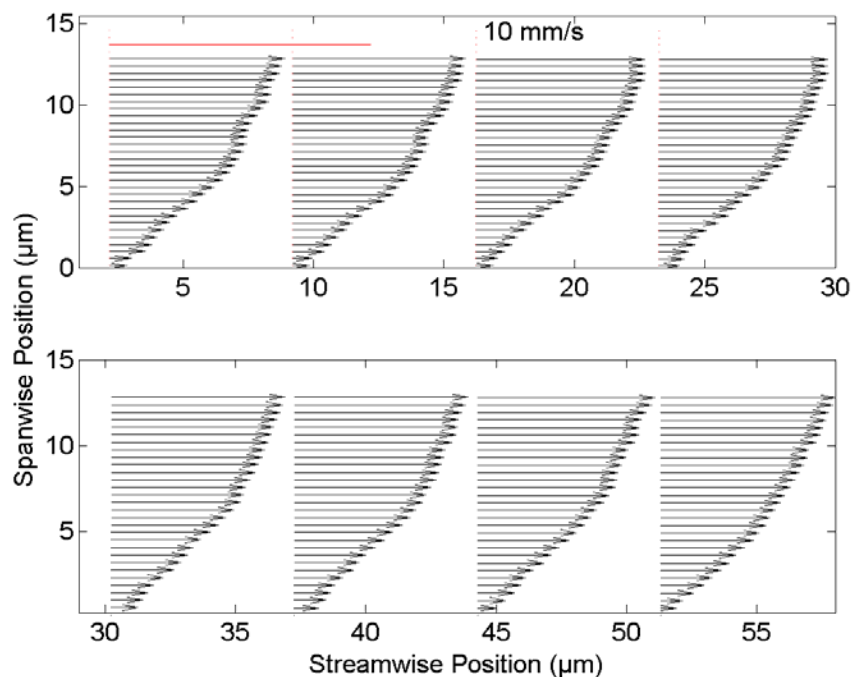


Figure 2.67: Velocity profiles along the microchannel wall. The various profiles show regions of slip and no-slip.

2.7 On-chip Two-Dimensional Separations (Stanford University)

The team developed a novel on-chip assay devices that combines isoelectric focusing and zone electrophoresis to achieve a 2D assay in 1/30th of the time of a traditional system (and with 10,000x less sample). Based on conventional two-dimensional electrophoresis, this system sequentially combined isoelectric focusing and capillary electrophoresis in a single planar microfluidic device. Isoelectric focusing (IEF) separates chemical species based on their isoelectric points. At completion, sample species reach a steady state distribution of concentrated bands within a separation channel. Due to the focusing, steady state nature of IEF, the assay is inherently insensitive to dispersion caused by initial sample injection. Capillary electrophoresis (CE) separates species based on their electrophoretic mobility, a characteristic that is approximately proportional to the charge-to-mass ratio of the species.

The planar geometries used for much of this work were designed in-house and fabricated by ACLARA Biosciences (Mountain View, CA) in poly(methyl methacrylate) (PMMA) using an imprinting and laminating technique similar to that reported in the literature [78]. The channel cross-sections were D-shaped and measured 200 μm wide and 20 μm deep.

The schematic of the microchip and assay procedure is depicted schematically in Figure 2.68. The first dimension (horizontal channel in the figure, from A to C) is 2.8 cm long and the second

dimension (vertical channel B-W) is 2.5 cm long. Custom fixturing was designed and fabricated in-house to provide wells for inserting electrodes and allow for pressure filling of liquid into the channels [79].

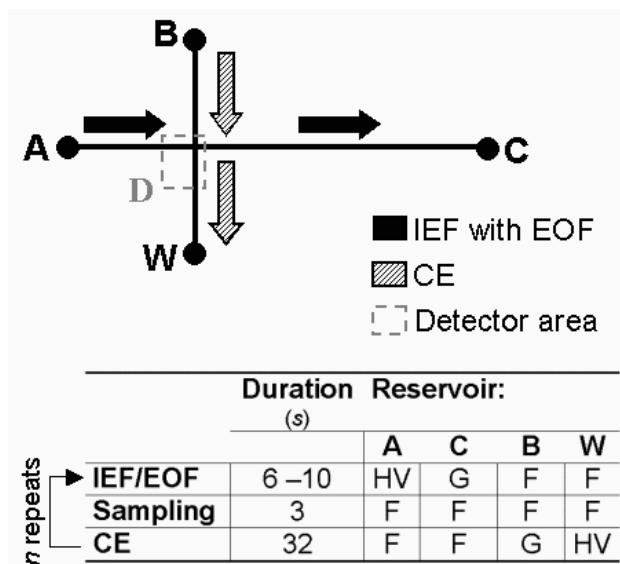


Figure 2.68 Separation algorithm for the 2D IEF-CE separation.

The device geometry is shown with arrows indicating the bulk fluid motion during each serial separation step. The first dimension (IEF) extends from reservoir A (analyte) to reservoir C (catholyte). The second dimension (CE) extends from reservoir B (buffer) to reservoir W (waste). The imaged area is indicated by the dashed box, D. The voltage applied during each step of the 2D separation is shown in the table (HV: high voltage, G: ground, F: float).

Figure 2.68 and the CCD images presented in Figure 2.69 aid in description of the 2D separation algorithm. After the initial focusing step, the 2D separation algorithm consisted of multiple iterations through the following sequence of steps: (Figure 2.69 A) an IEF separation with simultaneous EOF mobilization of sample species along the axis of the first dimension (IEF/EOF), (Figure 2.69 B) electrokinetic sampling of a relatively small volume of the IEF dimension constituents into the CE channel, and (Figure 2.69 C) a CE separation in the second dimension. Figure 2.69 D shows the start of the next separation cycle in which IEF and simultaneous mobilization have been reinitiated in the first dimension. As this is a serially implemented 2D separation, the separation sequence is repeated until all fluid volumes from the IEF dimension have been sampled into the CE dimension.

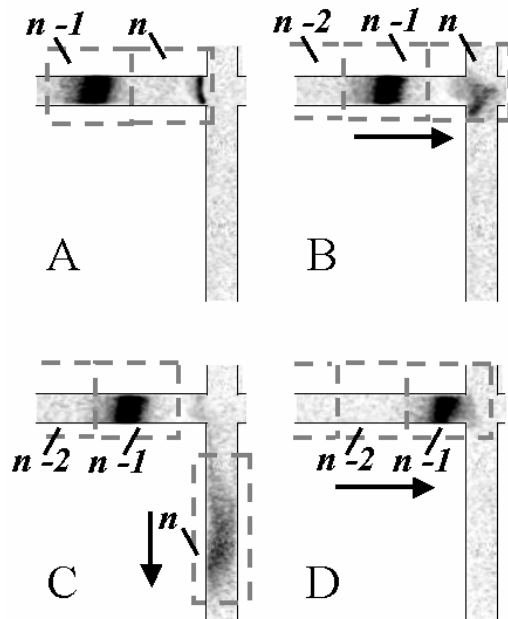


Figure 2.69: CCD images during species sampling.

(A) Species are focused by IEF in the first dimension (dark bands in horizontal channel). Simultaneously, the bands are mobilized towards the catholyte reservoir by low-dispersion EOF. (B) Once a fluid volume of interest, n , reaches the microchannel intersection, all electrodes are switched to electrically float for 3 s. (C) High voltage is then applied at reservoir B and reservoir W is grounded, initiating sample separation in the second dimension. (D) Upon completion of the CE separation, IEF/EOF is reinitiated causing sample species to refocus and the next fluidic volume ($n-1$) to migrate to the intersection. This sequence is repeated until all fluidic volumes are sampled from first dimension into the second.

Simultaneous focusing and EOF-driven mobilization transported focused sample species to the sampling intersection with an electroosmotic velocity of order $20 \mu\text{m}/\text{sec}$ (Figure 2.69 A, D). After a fluidic volume of interest reached the intersection (Figure 2.69 B), all reservoirs were switched to electrically float for 3 s prior to sampling. During this period, focused sample species began to defocus, as presumably did the much lower molecular weight ampholytes. The floating step was incorporated into the voltage algorithm to electrically decouple the two assay dimensions and to allow for a more homogenized pH field near the intersection. Mass continuity ensures that the bulk of fluid sampled from the IEF dimension into the CE dimension was replaced with unfocused ampholyte solution (Figure 2.69 C). This algorithm resulted in an IEF separation that was essentially ‘parked’ during each CE analysis, as species were refocused ($E = 350 \text{ V}/\text{cm}$ for 6 - 10 sec) prior to additional CE analyses (Figure 2.69 D). Each sampling event, CE separation, and IEF re-focus cycle had a period of 45 s.

Two-dimensional “gel-like” plots were constructed from a time-sequence of CCD images collected during the 2D separations. The gel-like plots were formatted to display inverted gray scale intensity information so as to mimic a slab-gel result with dark regions corresponding to

high fluorescence intensity zones. Figure 2.70: shows the results of a 2D separation using a gel-like format for three time steps during the 2D analysis (Δt of 3s, 5s, and 7s). Each vertical column ('lane') in the gel-like plot is generated from a spatial electropherogram that indicates the intensity of fluorescence along the CE separation channel. In each gel-like plot, the electropherograms correspond to equal-duration CE separations (i.e., the CE data for each 2D plot were collected at equal time periods after the respective electrokinetic injection). Accordingly, the ordinate axis of the gel-like plot corresponds to the axial coordinate along the second dimension of the assay. Since the method developed in this work is a serial 2D analysis, the vertical lanes correspond to CE analyses of fluid volumes sampled from different, adjacent locations along the IEF dimension; thus, each vertical lane is an analysis of a single sampling event from a discrete pI range. As a consequence, the abscissa of each 2D plot is proportional to the axial dimension along the IEF channel. Recall that during IEF, the focused bands are mobilized from left to right into the injection region with a mobilization velocity of roughly 20 $\mu\text{m/s}$. The left-most lane of each gel-like plot presented in Figure 2.70: corresponds to the first sampling event, while columns to the right correspond to subsequent sampling from fluid volumes containing decreasing pI values.

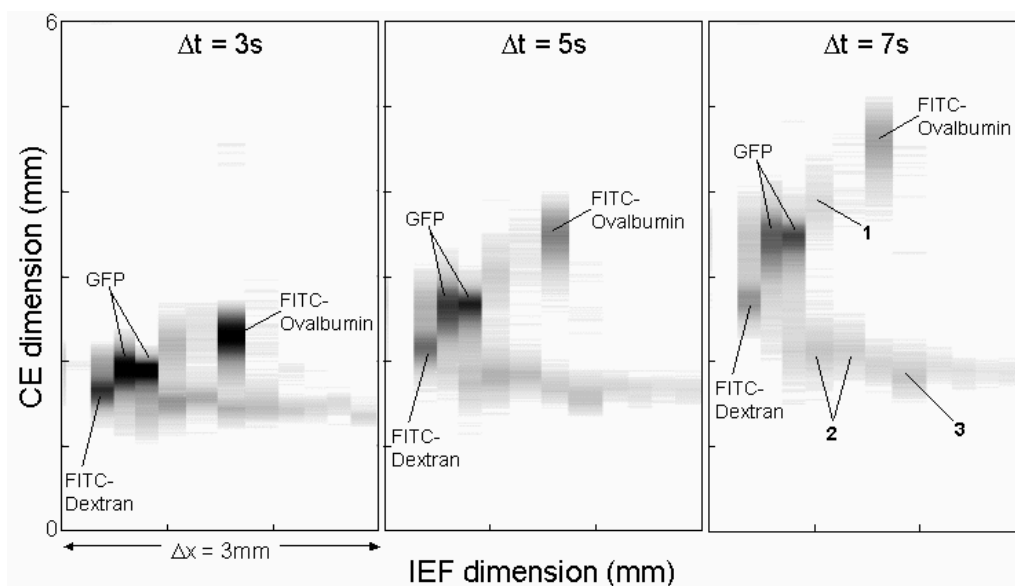


Figure 2.70: Gel-like plots of an IEF-CE separation at CE analysis times of 3 s, 5 s and 7 s.

The horizontal axis corresponds to the relative position of each fluid element during the IEF separation. Approximately 3 mm, or 15%, of the total IEF channel length was sampled ($E = 350 \text{ V/cm}$). The vertical axis corresponds to the spatial axial dimension of the subsequent CE separations ($E = 390 \text{ V/cm}$).

Species not identified in companion 1D separations are labeled as peaks 1, 2, and 3.

2.7.1 2D Assay Performance

The team demonstrated a single, planar, polymer microdevice that serially integrates two rapid, orthogonal chip-based separation schemes (IEF and CE). The boundary conditions of the terminal channel reservoirs (e.g., applied potential, chemistry, and pH) in a cross geometry were used to govern the separation mechanisms throughout the analysis. A mixture of fluorescent sample species was focused during IEF and mobilized by low-dispersion EOF to a junction, where effluent volumes were repeatedly electrokinetically sampled into the CE dimension. Such electrokinetic control of sample species and bulk fluid motion is advantageous for automated on-chip systems. IEF in 2D system showed rapid peak generation (less than 1 min), reduced EOF without the introduction of high viscosity additives, resultant highly concentrated sample species (70-fold), and a high peak capacity. Species behavior in the second dimension of the IEF-CE system was consistent with a CE separation mechanism (i.e., a constant velocity difference between neighboring peaks and diffusional broadening of injected sample species). These results suggest that the two separation mechanisms (IEF and CE) remain independent despite the fact that the two separation dimensions are fluidically coupled and use the same liquid medium. Results from the 2D analysis suggest increased separation resolution over that of the corresponding uncoupled 1D separations, as peaks that were not detectable during 1D separations under identical conditions were apparent in the 2D separation. The complete 2D system was estimated to have a peak capacity of ~1300.

The peak capacity and resolution may be further improved by reducing the size of each fluid volume sampled into the second dimension (perhaps by reducing the width of the extraction junction), increasing the channel length of the second dimension, and reducing dispersion during sample handling between the first and second dimensions. The low viscosity of the separation media, in combination with the short separation channel length scales used, resulted in rapid IEF and CE analyses. That noted, the analysis time of this system was dominated by that of the second dimension and could be reduced further through implementation of a manifold of CE channels that would allow sampling and analysis of numerous analyte volumes from the first dimension in parallel. The total analysis time for a parallel system should decrease as the number of additional CE channels increases, although system complexity will also increase. The liquid-phase approach presented may facilitate further system integration, including fraction collection and coupling of IEF-CE with a third dimension (e.g., mass spectrometry).

The combination of these two powerful separation techniques, in a single system, can be used to obtain two important physical characteristics (isoelectric point and mobility), a significant preconcentration of the sample, and a high separation resolution. These species are well resolved after less than a minute of elapsed focusing time. The full characterization and performance of the system is described in [80].

2.7.2 Benchmark Comparisons with Competing Technologies

Comparisons between several key performance parameters of the system described here and that of various other systems are presented in Table 2.12. These benchmark comparisons were made to: classical 2D slab-gel electrophoresis, a capillary-based 2D system involving IEF, and an on-chip 2D separation system involving CE as the second dimension.

Table 2.12: Multi-dimensional system performance comparison.

Comparisons are made between slab-gel 2D electrophoresis, a capillary-based system that couples IEF with mass spectrometry, an on-chip system that couples MEKC with CE, and the system developed in this work.

	2D Electrophoresis (Slab-gel)	CIEF-MS	On-chip MEKC-CE	On-chip IEF-CE
Analysis time	Several days	150 min	10 min	~60 min
Volume of first dimension analyzed	100 %	--	10 %	100 %
Peak capacity	1000 – 3000 (standard) 10^3 – 10^4 (large format)	>700	180-360	~800
RSD%	> 20%	5-10% (?)	--	> 30% (?)
pI resolution	0.01	< 0.1 pH unit	N/A	< 0.1 pH unit
Required sample amount	100 mg - \geq 1 mg	300 ng	--	10 ng
Automation	No completely integrated systems, only semiautomated	Possible	Possible	Possible

2.7.3 Impact of 2D Assay Work

The development of robust, fully-functional multi-dimensional assay chips applicable to complex analytes is considered by many to be the "holy grail" in microfluidic systems development. The Stanford two-dimensional assay system was the first to combine capillary isoelectric focusing (CIEF) (a method of separating and focusing proteins in a pH gradient) and CE on a chip [81]. The device was less than 2.5 cm on each side (1.1 mm thick) and automates sample injection and separation. The initial IEF step focuses samples to more than 100X their concentration, and a pH range of 3 to 9 is addressable. The peak capacity here achieved is comparable to that of commercially-available macroscale devices while the assay time is less than 1 hr (vs. a typical 2 days for the macroscale system). The required sample amount is 0.05 micrograms vs. order 1 mg for the macroscale systems. This device and its associated innovations have the potential of replacing 2-D slab gel assays in a variety of applications. The system holds promise as a basis for high-throughput, high-resolution protein and peptide analysis. The team demonstrated the performance of this device in a challenging six protein assay in a collaboration with Prof. P.J. Utz of the Stanford Medical School [81]. The Stanford team's close collaboration with Utz is impacting many areas of the Stanford team's work and is an excellent example of the importance of interdisciplinary research in the field of microfluidics.

2.8 Field Amplified Sample Stacking Experiments (Stanford University)

The team developed a novel FASS CE system with a porous polymer structure that facilitates the establishment of high conductivity gradients required to achieve ultra-high concentration increases using FASS[4]. The porous structure minimized instabilities associated with the mismatch in conductivity. A signal increase greater than a factor of 1000 is obtained, which, at that time, was the highest sensitivity-enhancement reported to date using on-chip FASS as a stand-alone method.

A porous polymer plug was fabricated in a glass microchannel with a double-T injection geometry (Micralyne, Alberta, Canada) using photoinitiated polymerization. The porous structure was photo-defined at a desired location using a reagent injection process (in conjunction with a Mylar film mask) which the team developed.

The group applied this FASS system to effect a separation of 2 μM and 1 μM initial concentrations of fluorescein and bodipy, respectively. Figure 2.71 shows the separation of sample analytes detected at 10 mm downstream from the injection region. The electropherograms shown are determined by spatially integrating full-field detection data (over a 5000 μm^2 region to simulate the detection of a photo-multiplier tube device). First, it is shown that the use of the device in a CE injection and separation with matched sample and background buffers, i.e. no FASS (Figure 2.72a). Second, the group have demonstrated that a signal increase by more than a factor of 1000 (Figure 2.72b) using an aggressive FASS process chemistry with a high conductivity (77.6 mS/cm) background buffer and a low conductivity (60.1 $\mu\text{S/cm}$) background buffer and sample. Additional details on the experiments and FASS dynamics may be found in [82] and [83].

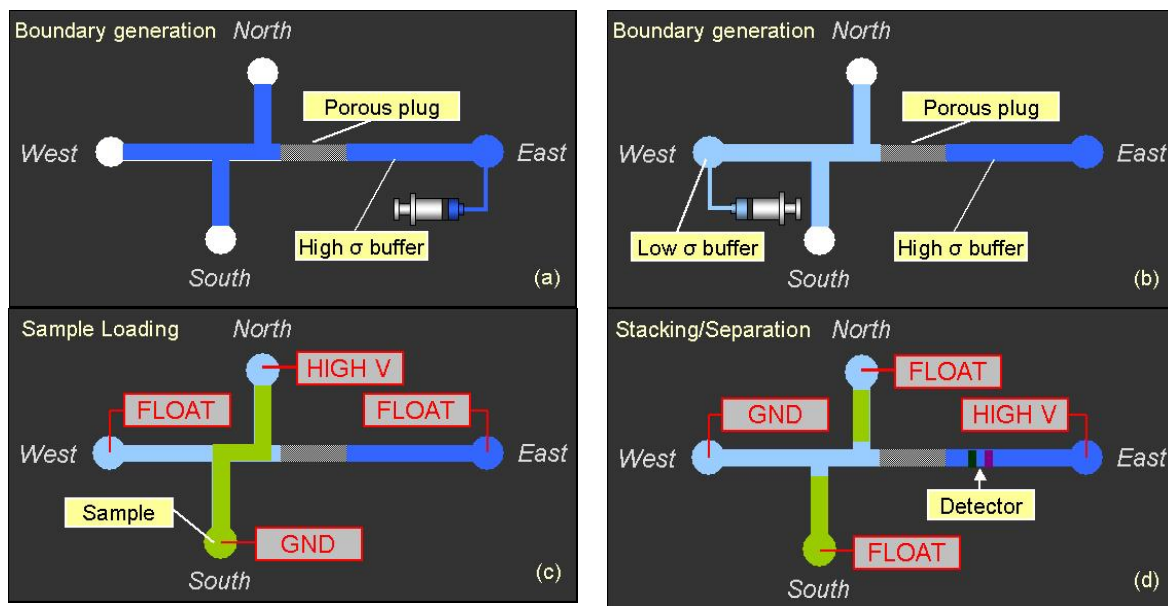


Figure 2.71: Schematic of FASS/CE protocol.

(a) High conductivity buffer is injected from the east reservoir. (b) Low conductivity buffer is introduced from the west reservoir. Porous structure provides high fluidic-resistance which minimizes the mixing of two buffers at the boundary. (c) Sample is electrokinetically loaded in the double-T injector. Negatively charged sample ions electromigrate from the south reservoir (grounded) to the north reservoir (high voltage). (d) Sample stacking, separation, and detection.

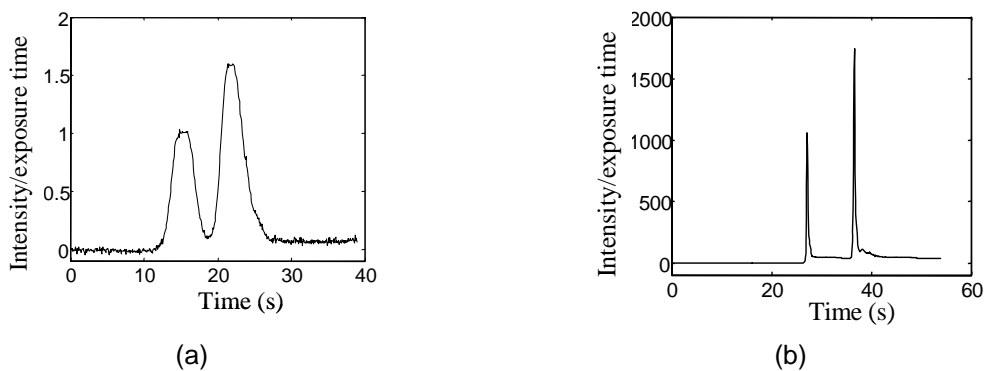


Figure 2.72: Electropherograms of fluorescein and bodipy separation.

Fluorescence signal was normalized with exposure time. The signal increase is on the order of 1000 fold for the stacked case. The position of detector is 10 mm from the downstream intersection of the channel. (a) Electropherogram of analytes in a CE separation and detection performed without stacking. Conductivity ratio, $\gamma = 1$, exposure time is 50 ms. (b) Stacked CE Electropherogram. Conductivity ratio, $\gamma = 1290$, exposure time is 5 ms. Difference in electromigration time is due to the effects of FASS.

3.0 MICROFLUIDIC SYSTEMS FOR HIGH SAMPLE STACKING ASSAYS

3.1 Introduction

An additional task was added to the initial research effort that focused on developing rapid sample pre-concentration methods to improve the sensitivity of on-chip assays (with a target figure of merit of 10,000 fold increase by project end). Leveraging the results on field amplified sample stacking and electrokinetic instabilities from the initial project, the Stanford team was able to develop improved stacking methods using field amplified sample stacking (FASS), thermal gradient focusing, and isotachopheresis (ITP). Ultimately, the team experimentally demonstrated million-fold sample concentration increase (approximately three orders of magnitude better than the second best ever demonstrated on or off chip). This section reviews the results of this experimental work.

3.2 Field Amplified Sample Stacking Results

As part of the extension project, narrow-channel chips were designed to have a comparable hydraulic resistance to the porous plug chip design developed under the original project[84]. Figure 3.1 shows the layout of the new stacking chip and images of narrow-channel regions.

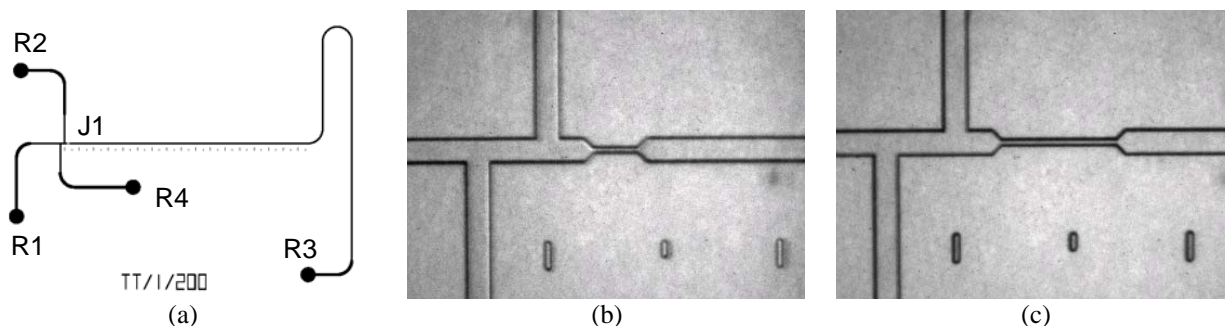


Figure 3.73: (a) Narrow-channel stacking chip geometry.

Channel length between R1-J1, R2-J1, and R4-J1 are 6.5 mm, length between R3-J1 is 45 mm. (b) & (c) Reflective mode microscopy images of narrow-channel with a double-T injection geometry. The microchannels are 10 μm deep with a D-shape characteristic of wet etching of glass. Wide-channels are 120 μm wide, and narrow-channel is 40 μm wide at the top. The lengths of narrow-channels are 200 μm (b) or 500 μm (c).

High conductivity ratio FASS experiments were performed using these narrow-channel plug microchips. A 12,000-fold concentration increase was achieved through the use of a modified sample loading scheme that was developed (Figure 3.2). The new sample loading scheme enabled the introduction of sufficient sample ions for ultra-high conductivity ratio sample stacking (Figure 3.3). Various EOF suppression reagents and pretreatment methods were also

explored, and it was determined that a poly-*N*-hydroxyethylacrylamide (PHEA) coating achieved the greatest EOF reduction. The electroosmotic mobility of a glass microchannel was reduced to 2% of the original value by adding 0.1% PHEA in buffer solution (10 mM 4-(2-Hydroxyethyl) piperazine-1-ethanesulfonic acid, HEPES, pH = 7).

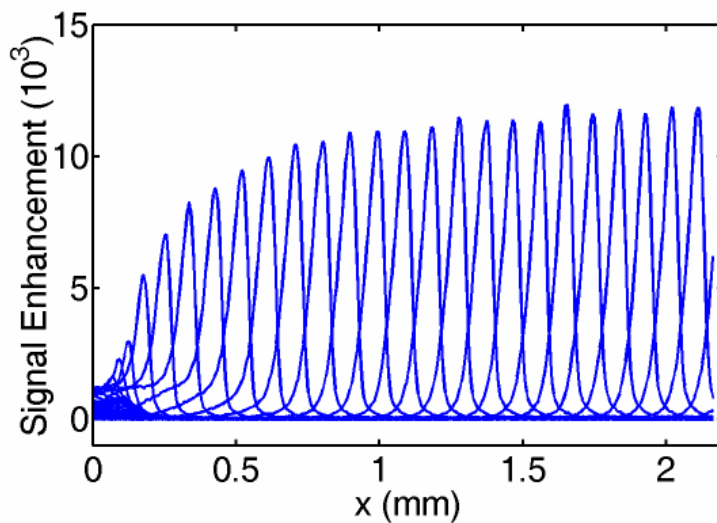


Figure 3.74: Plot of signal peaks for sample stacking of AlexaFluor analyte.

The highest peak shows a stacking ratio (i.e., concentration increase) of 12,000-fold. The initial sample concentration was 0.1 μ M of AlexaFluor in DI water ($\sigma = 4.72 \mu\text{S}/\text{cm}$), and the high conductivity solution was 0.5 M KCl in 5 mM HEPES (59.1 mS/cm). The conductivity ratio was 12.5×10^3 .

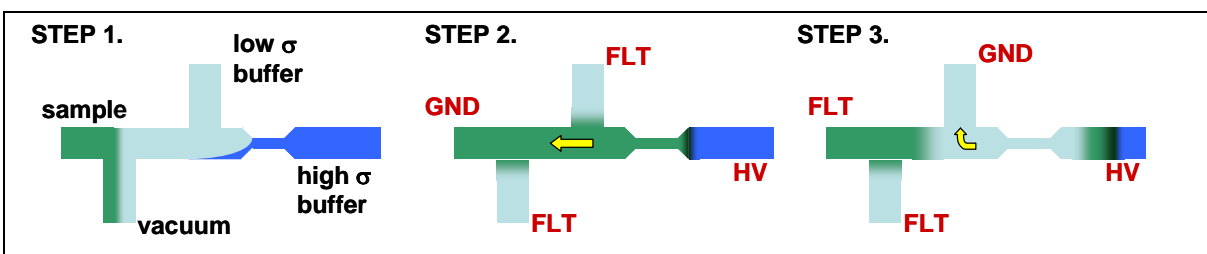


Figure 3.75: Schematic of FASS assay protocol.

(i) The north, east, and west reservoirs are filled with low conductivity buffer, high conductivity buffer, and sample solution, respectively. The conductivity boundary is formed by applying vacuum to the south reservoir. (ii) FASS is initiated by applying high voltage and ground to the east and west reservoirs, respectively. The yellow arrow shows the direction of electric field. Negatively charged samples electromigrate towards the anode under suppressed EOF. (iii) The voltage is switched to stop further sample introduction.

The 12,000-fold stacking represents a likely practical limit for stacking with FASS. At higher conductivity ratios, both nonlinear effects and electrokinetic instabilities were observed. These non-linear effects showed behavior similar to that of ITP, another electrokinetic preconcentration technique. The results from the FASS studies suggested that ITP itself might yield improved stacking performance. The Stanford team pursued this approach and the results are summarized later in this section.

3.3 Isotachophoretic Stacking Results

Isotachphoresis is another electrokinetic preconcentration technique where sample ions stack in adjent regions according to their electrophoretic mobility, ultimately creating a train of sample zones which migrate at a constant speed (hence “isotacho”). Based upon the insights from the FASS work, Stanford initiated development of an ultra high stacking ITP/CE method (Figure 3.4).

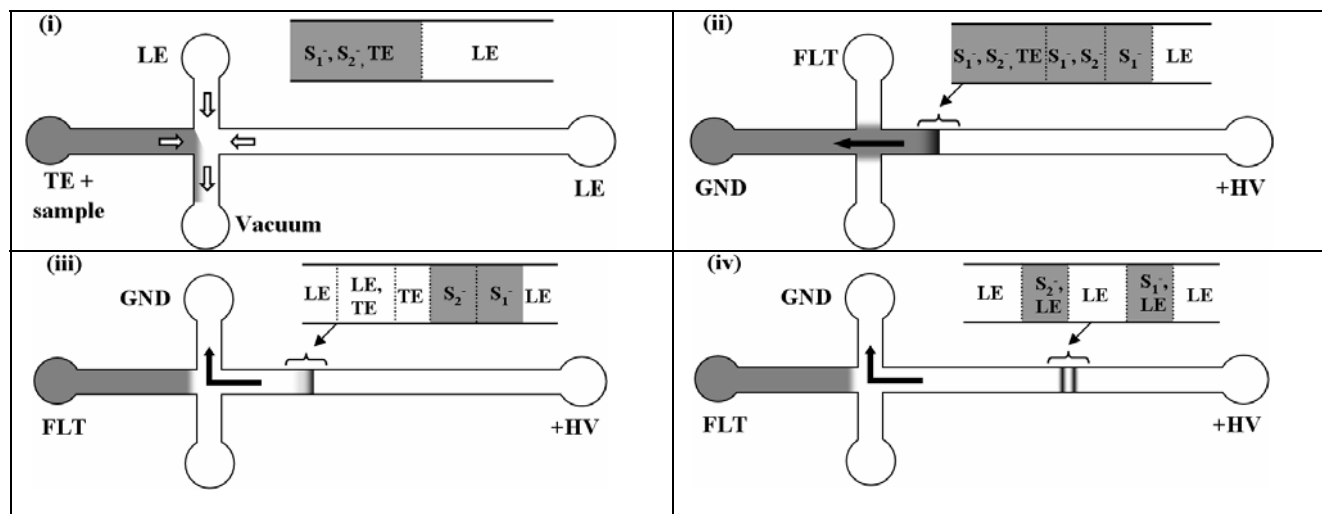


Figure 3.76: Schematic of ITP/CE assay protocol.

Configurations of co-ions are also shown at each step. (i) The north and the south reservoirs are filled with leading electrolyte (LE), and the west reservoir is filled with a mixture of trailing electrolyte (TE) and sample. The TE/LE boundary is formed by applying vacuum at the south reservoir. White arrows show the direction of pressure-driven flows. (ii) ITP stacking is initiated by applying high voltage and ground at the east and west reservoirs, respectively. The black arrow denotes the direction of electric field. Sample ions (negatively charged) electromigrate toward the anode as EOF is suppressed. The early stage of ITP stacking results in a partial separation (i.e., moving boundary electrophoresis). (iii) The field is switched toward the north reservoir to initiate CE. ITP stacking occurs until the leading ions overtake the trailing ions. (iv) Separation of sample analytes occurs further downstream where sample ions electromigrate in homogeneous background electrolyte.

The hybrid ITP/CE method did not require a specialized microchannel design or complex flow control. It could therefore be implemented with easily available “off-the-shelf” chip systems using common voltage control methods and buffer chemistries. High sample stacking was achieved through a variety of optimizations. These included: using a high concentration leading electrolyte and low initial sample concentration, as suggested by non-dispersive 1D theory; suppressing EOF to minimize dispersion due to EOF mismatch; leveraging the high conductivity ratio and using proper channel lengths to maximize electric field in the sample zone and increase electric Peclet number; and implementing single interface stacking to yield a large effective injected sample volume.

ITP stacking is implemented using a leading electrolyte (LE) with relatively high mobility ions and a trailing electrolyte (TE) with low mobility ions. The ion mobilities of the LE and TE are respectively lower and higher than those of the sample ions, so sample ions focus within a

narrow zone between the two electrolytes and then migrate at the same velocity. After preconcentration, the ITP is terminated and CE separation is initiated using a novel injection method which depletes LE ions and replaces them with TE ions.

The resulting isotachopheresis injection method was very robust and easily integrated with microchip-based capillary electrophoresis (CE) devices. The Stanford team was able to improve the performance of the ITP/CE protocol and to achieve better than one million-fold sample preconcentration of Alexa Fluor 488 and performed high sensitivity electrophoretic separations.

The effectiveness of the ITP/CE protocol was demonstrated with separations of Alexa Fluor 488 and bodipy. Figure 3.5 shows the separations of sample analytes detected 30 mm downstream of the intersection without (inset) and with ITP stacking. The electropherograms were determined by spatially integrating full-field CCD imaging data over a 60 by 60 μm region centered on the channel centerline to simulate the detection of a point-wise photodetector. The exposure time and CCD frame rate were 10 ms and 50 frames per second, respectively. The inset of Figure 3.5 shows the separation without ITP with initial (relatively high) concentrations of 100 nM and a uniform background electrolyte consisting of 5 mM HEPES buffer (pH 7.0). Signal intensity was normalized using the flatfield image signal of 100 nM Alexa Fluor 488. The applied field was 280 V/cm. The SNRs of Alexa Fluor 488 (first peak) and bodipy (second peak) were 12.9 and 10.8, respectively, and the peak resolution was 29.4. SNR is defined as the ratio of peak intensity to twice the standard deviation of background noise; and resolution as the distance between two peaks divided by the full-width half-maximum of the wider peak. Separation was performed on a sample mixture diluted by a factor of $1\text{E}5$ (1 pM solutions each of Alexa Fluor 488 and bodipy) using the ITP/CE method. The result is shown in Figure 3.5. The injection/ITP time was 40 s and with a nominal applied field of 220 V/cm. The resolution of these peaks was 6.1 and the SNRs were respectively 57.6 and 39.0 for Alexa Fluor 488 and bodipy. The ITP phase of the experiment shown in Figure 3.5 achieved a concentration increase of approximately 0.5 million-fold immediately prior to initiation of the CZE mode. This experiment achieved concentration increase of $6.4\text{E}4$ relative to the initial sample concentration (1 pM), and signal increase of $4.5\text{E}5$ -fold relative to the unstacked case.

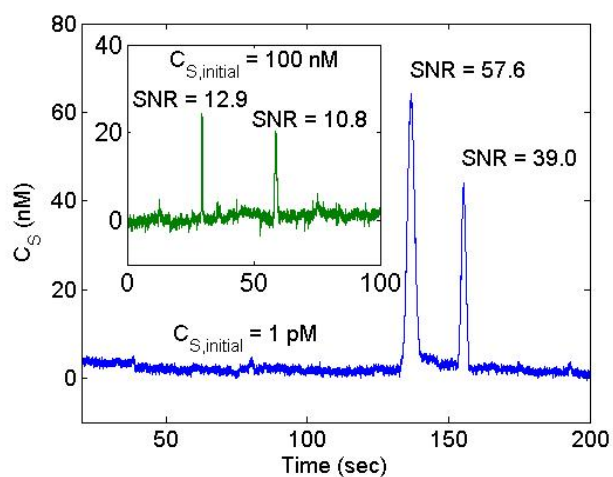


Figure 3.77: Isotachophoretic stacking and detection of Alexa Fluor 488.

Figure 3.6 shows a spatiotemporal intensity plot of the calibrated fluorescence intensity (a measure of concentration) versus separation distance and time from which sample peak reaches the detection window, for an initial sample concentration of 100 fM of Alexa Fluor 488 dye. The LE was 1 M NaCl, and the TE was 5 mM HEPES buffer. The microscope is equipped with a 10X objective (Numerical Aperture (N.A.) of 0.4) with viewing dimensions of 1.2 by 0.1 mm in the object plane. A brief (~ 2 min) sample stacking step enables the detection of 100 fM analyte concentration with $SNR = 11$. Measured concentration distributions yield a maximum measured concentration increase, CI , of approximately $2E6$ -fold. This concentration increase is achieved within 120 s and 30 mm downstream of the injection point. To the knowledge of the Stanford group, this is the highest sample preconcentration for either capillary or on-chip electrophoresis systems.

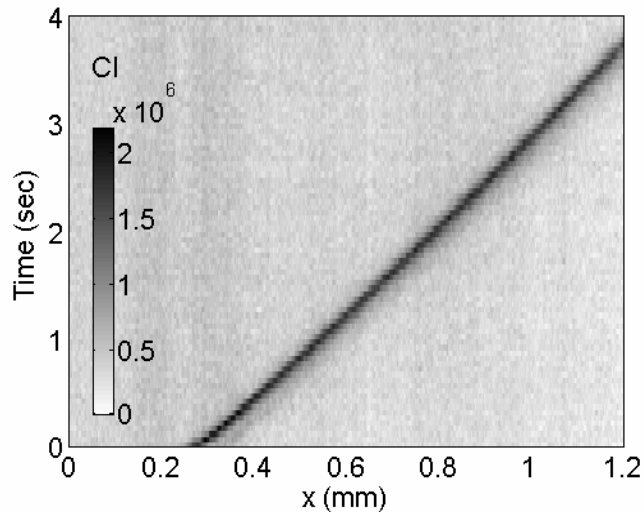


Figure 3.78: Detection of Alexa Fluor 488 at an initial concentration of 100 fM, greater than million-fold concentration increase.

LE and TE were respectively 1 M NaCl and 5 mM HEPES. A 10X objective (N.A. of 0.4) was used.

3.4 Comparison of the Current High Sensitivity Methods with Other Work

Here is presented a comparison of the work with the detection limits of various point-wise CE detection modalities and associated research efforts. This comparison is an effort to characterize and summarize the many point-wise detection methods and serves as a short introduction to the electroosmotic flow diagnostics systems discussed in this chapter.

Figure 3.7 shows the detection limits of CE detection systems as a function of their molar sensitivity. The figure is adapted from a less comprehensive version published in the book by Landers[85]. Molar sensitivity is plotted on the abscissa, and is formulated here as the number of sample moles loaded onto the capillary column. The ordinate of the graph shows the concentration of the sample of interest. The concentration limit of detection for a given sample amount is then dictated by the detection technique used. Trends are apparent for three detection schemes: electrochemical, fluorescence and ultraviolet (UV) absorbance.

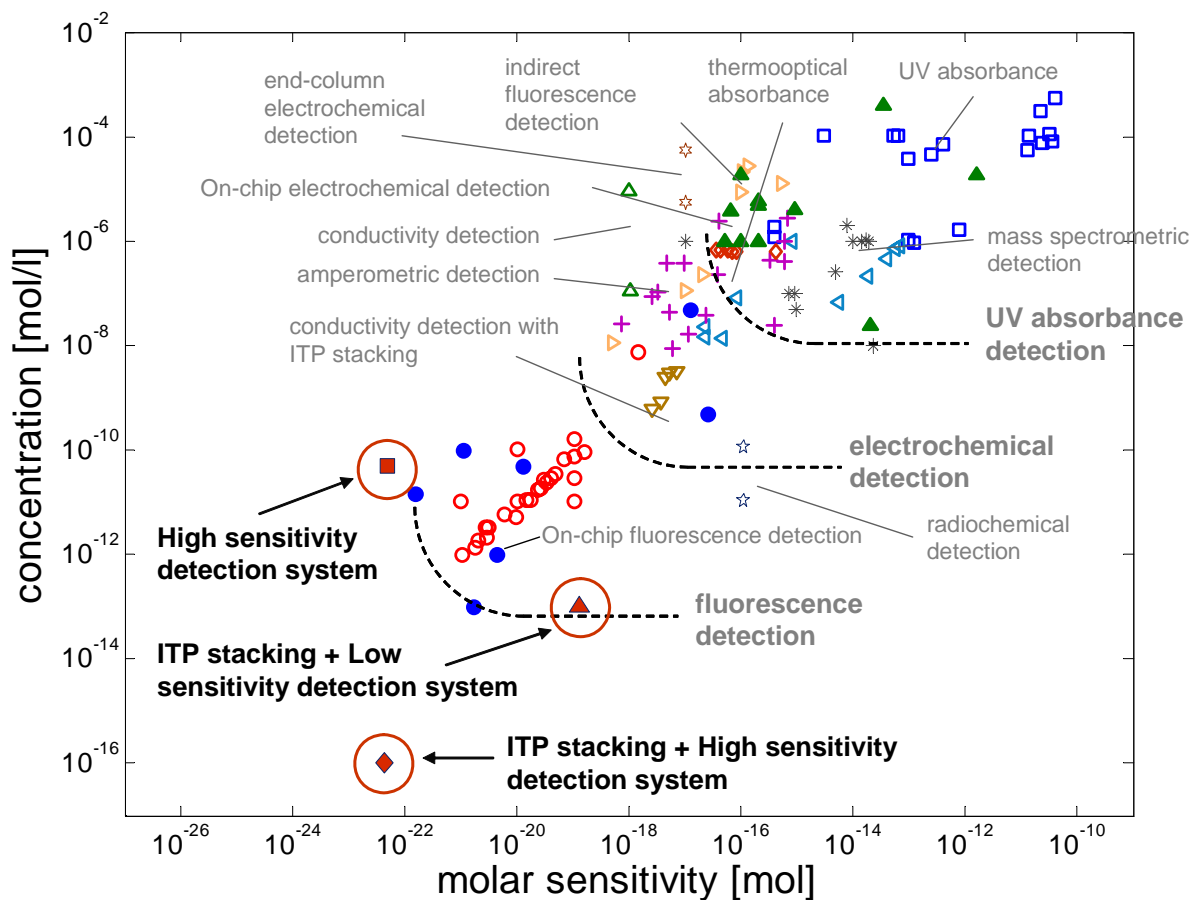


Figure 3.79: Detection techniques for capillary electrophoresis (adapted from the CRC Handbook of Capillary Electrophoresis [85], with permission).

Molar sensitivity (here defined as the number of moles which are detected) and concentration are plotted on the abscissa and ordinate, respectively. Fluorescence detection is observed to have the highest sensitivity among single-point CE detection schemes. Also shown in the plot is the detection capability for fluorescence detection in a microfluidic system with an intensified 12-bit CCD camera.

Electrochemical detection includes amperometry, conductivity, and potentiometry. The drawback with this detection scheme is the requirement for integrated electrode structures within the microchannel. In contrast to electrochemical detection, the sensitivity of UV absorbance is weak but is still very popular due to its simplicity of operation and the fact that untagged samples are detectable. A majority of the samples of interest, including peptides and proteins, absorb in UV wavelengths. Despite its popularity in free-standing capillary systems, UV detection is not easily applicable to microchannel systems etched in planar glass substrates due to the short optical path lengths available from the shallow channel depths, and the difficulties associated with transmitted light optics in an etched microchannel. Example detection limits from various high-sensitivity, on-chip detection efforts are shown as filled (blue) circles.

Shown together with this review of other work are results from the current high sensitivity ITP work. As mentioned above, the team developed a high sensitivity on-chip CE detection system that leverages both optimized optics and with a single-interface, transient ITP stacking protocol. The sensitivity of this system (without sample stacking) is shown by the data point labeled “High sensitivity system.” As described by Jung et al. 2006 [84] high efficiency photodetectors are combined, and performed extensive calibration studies of signal intensity dependence on excitation lasing power and objective specifications (N.A.s and magnifications). A high N.A. objective was used with relatively low magnification (yet compatible with cover glass thickness of microchip) and optimization of laser power so as not to overly saturate sample analytes. Fluorophores with high quantum yield and photo- and chemical stability were also used. As an example of the sensitivity of this system the group demonstrated effective single-molecule detection of 10 pM Alexa Fluor 488 under pressure-flow conditions (bulk velocity of 1 cm /s and no stacking) using an optimized laser-induced confocal fluorescence microscope setup fitted with 60x objective (N.A. of 1.4).

The sensitivity achieved by combining more standard CCD type detection (i.e., the detection system used for Figure 3.5) with the current optimized million-fold-capacity ITP stacking is indicated by the data point labeled “ITP stacking + low sensitivity system.” Lastly, the sensitivity achieved by combining the current high sensitivity detection (i.e., the detection system used for Figure 3.6) with the current optimized ITP stacking is indicated by the data point labeled “ITP stacking + high sensitivity system.” This high sensitivity CE detection system and a single-interface, transient ITP stacking method developed previously were combined to show separation and detection of 100 aM concentrations each of Alexa Fluor 488 and bodipy. This is, to the team’s knowledge, the highest sensitivity capillary electrophoresis separation and detection [84].

3.5 Some Reasons Why the Current ITP Stacking is Three or More Orders of Magnitude Better than other ITP

The group developed a 1D non-dispersive model and scaling of dispersion analysis[64, 86]. Although these scaling arguments are simple, they yield important insight into key ITP stacking parameters and suggest strategies for optimizing ITP in practice. These strategies include using high LE concentration and low initial sample concentration to maximize achievable concentration increase; suppression of EOF to minimize dispersions; and implementation of a single-column ITP configuration (where initially there is a single interface between the LE and the TE/sample mixture) to inject a large effective sample width. These strategies were implemented in the design of an ITP/CE method that combines a simple and robust single-column ITP stacking step with a subsequent CE step. First, a sample/TE mixture was injected to initiate ITP stacking and then injected LE at the channel intersection. The latter LE ion stream overspeeds the TE ions behind the stacked sample zone, terminates ITP, and initiates CE separation.

The team performed an experimental parametric study focused on the variation of LE, TE, and initial sample concentration. Consistent with the 1D non-dispersive model, it was found that

stacked sample concentration is proportional to the LE concentration, and the concentration increase, CI , (conveniently) increases as the initial sample concentration decreases. It was also found that the stacked sample concentration is a strong function of the TE concentration and the initial sample concentration. For the current configuration, low conductivity TE zones result in higher TE zone electric fields and therefore faster rates of stacking. High TE zone fields are probably also correlated with high stacked zone fields. The hypothesis is that this finding, combined with the large effective injection length of the single-interface ITP configuration, results in large sample electric/electrophoretic Peclet numbers and efficient stacking that is less susceptible to dispersion. Results suggest that comprehensive multi-species models with coupled fluid flow (including perhaps effects of non-uniform and dynamic zeta potentials), current conservation, and convective-diffusion-electromigration conservation are needed to fully describe ITP. Including of reaction buffer kinetics may also be important. The latter is the major motivation for the Stanford team's collaboration with the Sandia group whose work is described below.

3.6 Conclusions for High Sample Stacking Assays

Electrokinetic stacking techniques are a powerful tool for preconcentration of analytes of interest. The Stanford team successfully met and exceeded the target goal of 10,000-fold sample stacking, and further developed techniques capable of delivering better than million-fold stacking in less than two minutes. The team also demonstrated the highest sensitivity ever demonstrated for an electrophoresis separation: detection of 100 aM samples.

4.0 MODELING OF HIGH SAMPLE STACKING ASSAYS

4.1 Introduction

This section of the report details work on the simulation of sample stacking using isotachopheresis. The simulations were performed with a microchannel flow model that has a detailed representation of the various coupled physical phenomena that are relevant to sample stacking in flows with high electrical field strength gradients. The model relies on an equilibrium buffer electrolyte formulation to represent the changes in the buffer composition as a function of the solution pH . The effect of free charges in the solution, which are non-negligible in cases with high gradients in the electrical field strength, is taken into account in the momentum and charge conservation equations.

Extensive parametric studies were performed using isotachopheresis sample stacking methods developed by Prof. Santiago's research group at Stanford University. One-dimensional simulations showed good qualitative agreement with the experimental observations in terms of the early-time evolution of the dye in the stacking zone. The simulations also revealed that the buffer pH can change quite dramatically in this area. Despite the promising qualitative agreement, there remains a significant discrepancy between the simulated and experimentally observed stacking ratios. Qualitative differences were also observed in the late-time steady-state

behavior. It is surmised that more detailed two-dimensional simulations will be required to investigate these discrepancies.

This task on sample stacking was led by Stanford University with Juan Santiago as the principal investigator. Sandia National laboratories (SNL) and Johns Hopkins University (JHU) operated under subcontract to Stanford for this project. The goals of the SNL and JHU contribution were to provide modeling support for the experimental work in Juan Santiago's group. Given the particular focus of the experimental work on ITP and the evident high performance of this sample stacking technique, the modeling studies focused specifically on sample stacking in the context of ITP.

4.2 Formulation

The simulation of isotachopheresis for sample stacking in microfluidic channels requires the resolution of many coupled physical processes. For this purpose, the group leveraged a multiphysics microchannel simulation code that was developed as part of a previous, DARPA-funded project [87]. This code already contained the capabilities to simulate many of the physical phenomena occurring in microchannel flow, and was enhanced as part of this work in order to handle challenges specific to isotachopheresis with high gradients in the field strength.

This section gives an overview of the formulation of the resulting microchannel flow model and highlights the aspects of the model that were added as part of this project.

4.2.1 Flow Field

The flow field is described by the two-dimensional unsteady, constant density, Navier-Stokes equations along with the continuity equation.

$$\begin{aligned} \nabla \cdot \mathbf{u} &= 0 \\ \frac{\partial \mathbf{u}}{\partial t} + \mathbf{u} \cdot \nabla \mathbf{u} &= -\nabla p + \nabla \cdot \left\{ \nu \left[(\nabla \mathbf{u}) + (\nabla \mathbf{u})^T \right] \right\} - \rho_e \nabla \phi \end{aligned} \quad (4.1)$$

In these equations, \mathbf{u} is the velocity vector, p is the pressure (normalized by density), ν is the kinematic viscosity, ρ_e is the free charge density and ϕ is the electric potential. The term $-\rho_e \nabla \phi$ represents the body force exerted by the electric field on free charges in the solution. This physical phenomenon was added to the model as part of this work. For the simulation of electroosmotic flow, a slip wall velocity is used as a boundary condition, with a magnitude predicted by the Helmholtz-Smoluchowski equation:

$$u_w = \frac{\varepsilon \zeta}{\mu} \nabla_t \varphi_w \quad (4.2)$$

where u_w is the wall velocity, ε is the electrical permittivity, μ is the dynamic viscosity, and ζ is the zeta-potential, which is modeled as a function of the local pH and buffer molarity.

4.2.2 Species Transport

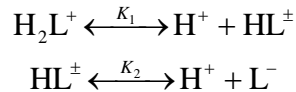
Species transport is governed by the following equations:

$$\begin{aligned} \frac{\partial c_i}{\partial t} + \nabla \cdot [c_i (\mathbf{u} + \mathbf{u}_i^e)] &= \nabla \cdot (D_i \nabla c_i) \\ \mathbf{u}_i^e &= -\beta_i z_i F \nabla \varphi \end{aligned} \quad (3.3)$$

where c_i represents the species concentration and D_i is the diffusion coefficient. The electrophoretic velocity \mathbf{u}_i^e depends on the species mobility β_i , its charge number z_i and the Faraday constant F . The values of the mobility and diffusion coefficient are connected through the Nernst-Einstein relationship, $D_i = RT \beta_i$, where R is the characteristic gas constant.

The species transport equation above is used for all species that do not participate in dissociation reactions, such as the dye (sample) ions, D^- , and the ions Na^+ and Cl^- of the fully dissociated salt NaCl. However, the components of weak acids or salts that make up the electrolyte buffer in microchannels participate in very fast electrochemical dissociation reactions. Because these dissociation reactions are much faster than other transport processes, they are modeled with an equilibrium formulation [88]. Specifically, for the HEPES buffer used in the experiments for this project, the formulation is as follows.

Consider the HEPES buffer consisting of three components, H_2L^+ , HL^\pm , and L^- , which participate in the following dissociation reactions:



Further, define the total buffer molarity $\theta = [\text{H}_2\text{L}^+] + [\text{HL}^\pm] + [\text{L}^-]$. Since the dissociation reactions do not change the value of this total buffer molarity (as those reactions are between the three ions that make up the molarity), this total molarity can be advanced in time using the species transport equation that is used for non-dissociating species. Given the total buffer molarity θ , the relative contributions of each component can then be obtained from:

$$\begin{aligned}
[H_2L^+] &= \alpha_{H_2L^+} \theta & \alpha_{H_2L^+} &= \frac{K_1 K_2}{K_1 K_2 + K_1 [H^+] + [H^+]^2} \\
[HL^\pm] &= \alpha_{HL^\pm} \theta & \alpha_{HL^\pm} &= \frac{K_1 [H^+]}{K_1 K_2 + K_1 [H^+] + [H^+]^2} \\
[L^-] &= \alpha_{L^-} \theta & \alpha_{L^-} &= \frac{[H^+]^2}{K_1 K_2 + K_1 [H^+] + [H^+]^2}
\end{aligned} \tag{4.4}$$

These relationships, however, first require the concentration of H^+ , to be known. This concentration is obtained from the charge conservation equation, $\rho_e = F \sum z_i c_i$, which for the solutions considered in this work translates to:

$$[Na^+] - [Cl^-] - [D^-] + [H^+] - \frac{K_w}{[H^+]} + (\alpha_{H_2L^+} - \alpha_{L^-}) \theta = \frac{\rho_e}{F} \tag{4.5}$$

where K_w is the water dissociation constant. The charge density ρ_e is calculated from the Maxwell equation for the electric potential $\nabla \cdot (\epsilon \nabla \varphi) = -\rho_e$. This charge density is usually very small and can be neglected. However, for the simulation of sample stacking with large gradients in the electrical field strength $E = -\nabla \varphi$, the charge density term can become of the same order of magnitude as some of the other terms in the charge conservation equation.

4.2.3 Electric Potential

The electric potential φ is obtained from the current continuity equation:

$$\begin{aligned}
\nabla \cdot (\sigma \nabla \varphi) &= -F \sum z_i \nabla \cdot (D_i \nabla c_i) + \mathbf{u} \cdot \nabla \rho_e + \frac{\partial \rho_e}{\partial t} \\
\sigma &= F^2 \sum z_i^2 \beta_i c_i
\end{aligned} \tag{4.6}$$

where σ represents the electrical conductivity of the solution, and the summations go over all species in the solution. Note that for the cases studied in this work, the last two terms in the current continuity equation, $\mathbf{u} \cdot \nabla \rho_e + \frac{\partial \rho_e}{\partial t}$, are generally very small and can be left out.

4.2.4 Implementation

This section discusses the implementation of the physics model that was outlined in the previous section. The isotachopheresis (ITP) configuration in the microchannel provides for sample stacking at the interface between a leading electrolyte (LE) region and a trailing electrolyte (TE)

region. The present implementation includes NaCl in the LE, and both HEPES and a fluorescent dye in the LE, where the dye is the sample being stacked.

Algorithms were developed for solving the governing equations in a rectangular, two-dimensional, microchannel geometry, with inflow-outflow boundaries. The construction built on the Sandia group's earlier work in [87], incorporating necessary extensions for the additional physical details in the present context, particularly: (1) the discontinuous HEPES buffer-NaCl configuration, and (2) non-electroneutral effects. Highlights of the algorithmic construction are given in the following. The presentation involves discussions of both two-dimensional (2D) and one-dimensional (1D) constructions. The 1D implementation was found to be useful in algorithmic development and testing. It was also used for most of the results reported further below, given its computational efficiency and robustness.

The incompressible Navier-Stokes equations are solved using a projection scheme, where the convective terms are integrated using 3rd order ADAMS-BASHFORTH (AB3) time integration, while the dissipation terms are solved using fractional stepping with 2nd order RUNGE-KUTTA (RK2) time integration. The pressure field is solved for using a fast-fourier transform (FFT) direct solver. The velocity field and the electrostatic body force term, in addition to the wall zeta-potential driven velocity boundary condition, provide the two-way coupling between the momentum solution with Navier-Stokes and the species equations.

The species equations are solved using a strategy that involves specialized handling for species dependent on fast (equilibrated) reactions, as described above. The solution strategy is intimately coupled with both the charge conservation constraint and the electrostatic field solution [73]. Time integration of these equations is shown schematically in Figure 4.1, using an RK2 construction. The team has also implemented an AB3 construction for these same equations, not shown in this schematic. It has also implemented both centered difference and Godunov upwind discretizations of the convective terms. Diffusive terms were discretized using centered difference constructions.

The top row in Figure 4.1 shows the state variables associated with each mesh cell. These variables include:

- **Solute concentrations** Strongly dissociated ion concentrations are stored explicitly at each grid cell. This includes the Alexa-Fluor 488 dye [D^-], Sodium and Chloride ions [Na^+] and [Cl^-]. Hydrogen [H^+] and hydroxide [OH^-] concentrations are also stored explicitly. In contrast, weakly dissociated ions are represented by a single concentration of the total molarity of all dissociation states in a given cell ($[HL]$ in the current case) plus the α -coefficients described above.
- **Electric potential** The electric potential Φ is computed at each grid cell. For the 1D case, a direct numerical solution is implemented. For the 2D case, a multigrid solver (mg2d) was used.

- Bulk Flow** The bulk flow velocity is found from the above Navier-Stokes solver for the 2D case. In the 1D case, it is simply specified, as it is dictated by boundary conditions on the domain.

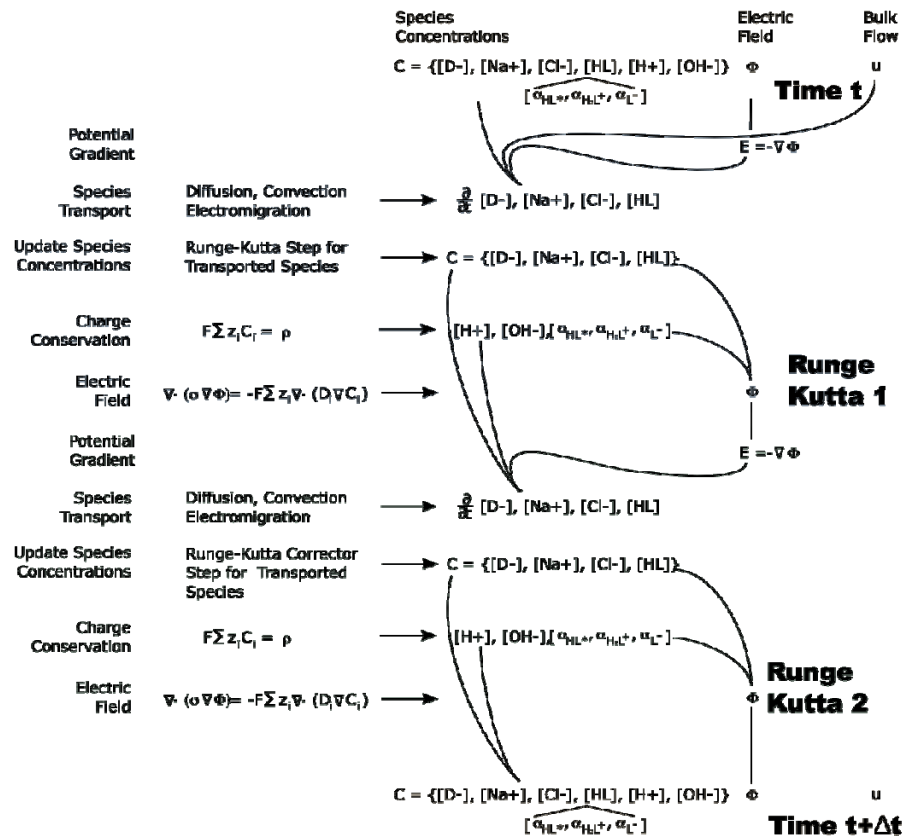


Figure 4.80: The state and equations used to advance the simulation in time for an RK2 integrator.

As Figure 4.1 shows, the electric field is derived from the electric potential by a simple gradient calculation. The electric field and bulk flow velocity are then used to compute the rate of change of each transported solute concentration. Three effects are modeled: electromigration of charged species, diffusion, and bulk flow. Because water is the solvent in which the solutes are transported – which effectively removes any upper limits on $[H^+]$ and $[OH^-]$ – and because the reaction kinetics of hydrogen and hydroxide ions are much faster than the integration time scale, these species are handled separately. Also, note that while $[19]$ is transported, the concentration coefficients are dependent on the pH of the solution and must be solved for in tandem with $[H^+]$ and $[OH^-]$ by applying a charge conservation to each cell of the grid. This leaves us with a quartic equation in terms of $[H^+]$. Once this equation is solved, the species concentrations can be moved forward in time with an EULER forward step. Derived quantities including the conductivity of the medium and charge diffusivity are recomputed and used to update the electric

potential. This is the final calculation in the first half of the RUNGE-KUTTA integration (“Runge Kutta 1” in Figure 4.1).

A corrector step, repeating all the steps in the previous paragraph using the state of the EULER forward step, is shown in the “Runge Kutta 2” section in Figure 4.1.

Figure 4.2 shows the experimental device schematic with the computational domain highlighted. For computational efficiency, the portion of the chamber where sample stacking occurs is modeled. The electric potential is constrained to match the applied voltage difference with Dirichlet boundary conditions. The concentration of each transported species at the left and right boundaries is modeled with a fixed-concentration condition when that species is flowing into the domain and as a zero-gradient when that species is leaving the domain. The top and bottom grid boundaries have zero-gradient boundary conditions applied to all species concentrations and to the electric potential. Initial conditions are defined based on experimental conditions as well as charge concentration and buffer equilibrium constraints.

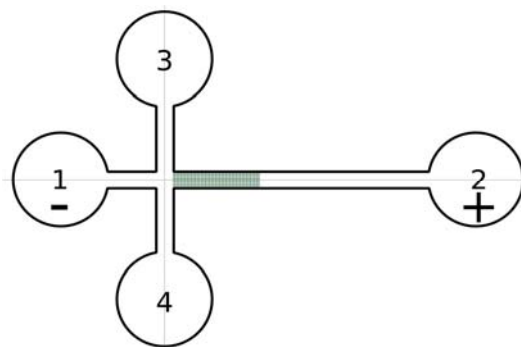


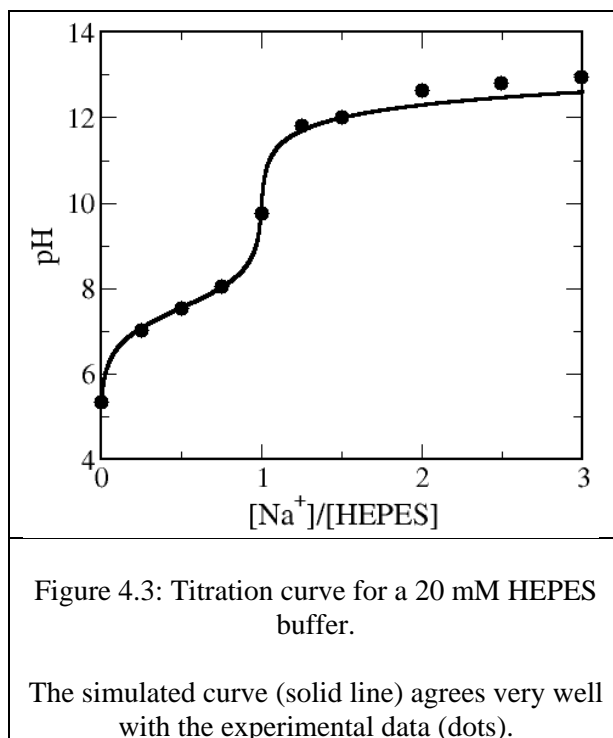
Figure 4.81: The experimental apparatus, with the portion modeled by the simulation shown in green.

4.2.5 Results

In the following, a presentation of the results of the buffer model is followed by 1D and 2D ITP results in the microchannel.

Buffer Titration Curve

As mentioned above, a HEPES buffer was used in the sample stacking experiments. To validate the buffer model in the current simulation code, a comparison was performed between the experimental and simulated titration curve for a 20 mM HEPES buffer. Figure 4.82 shows that the simulated curve agrees very well with the experimental data.



Sample Stacking in 1D at 4 kV/cm

This section gives an overview of the results of a 1D simulation of sample stacking via isotachopheresis (ITP) for a case with nominal field strength of 4 kV/cm in the trailing electrolyte (TE). In this case, the TE was initialized with 5 mM HEPES buffer and 1 nM dye (D^-). The leading electrolyte (LE) was initialized with 1 M Cl^- . The initial pH was set to 7 and the initial Na^+ concentration was calculated in order to achieve electroneutrality. This case was simulated over a 2 cm long domain, with the initial LE and TE zones each taking up 1 cm. An average field strength of 2 kV/cm was prescribed over this domain. However, as the conductivity in the LE zone is significantly higher than in the TE zone, almost the entire potential drop occurs in the TE zone, resulting in a nominal field strength in the TE zone of 4 kV/cm. These case settings correspond closely to the experiments in which stacking ratios of up to 10^6 were observed.

This case was simulated using 4096 grid points, with a time step of 25 μs , over a total of 200 s of simulated time. The convection terms were calculated with the centered difference scheme and time integration was performed with AB3. While the current implementation allows for non-electroneutral conditions in the bulk, as indicated above, parametric studies have been conducted with and without free charges. They showed a relatively minor role of free charges in the 1D context. In the results presented below, no free charges were considered in the bulk

(electroneutrality enforced everywhere). Moreover, with no loss of generality, the bulk velocity was set to zero over the whole domain. Figures 4.4 and 4.5 show the profiles of the Na^+ and Cl^- ion concentrations as a function of the streamwise coordinate, x , at 5 different points in time.

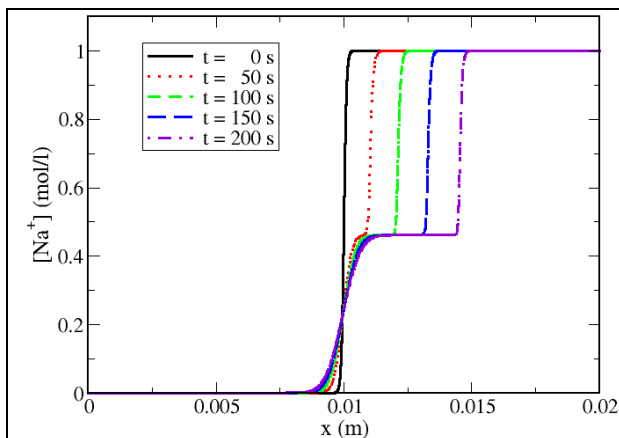


Figure 4.4: Evolution of the Na^+ concentration.

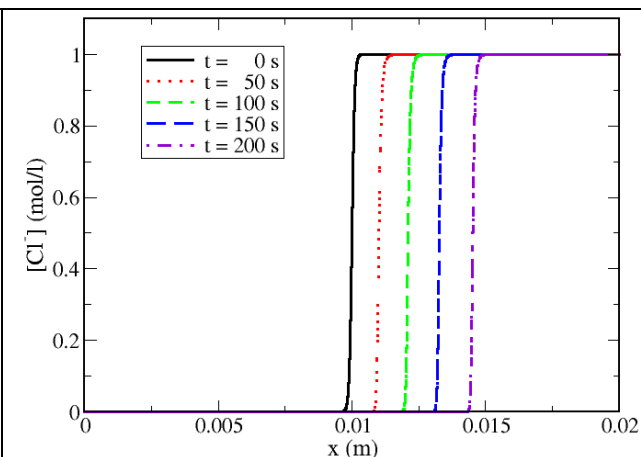


Figure 4.5: Evolution of the Cl^- concentration.

Both the Na^+ and Cl^- ions clearly move downstream in a front. Unlike the Cl^- ion concentration, the Na^+ ion concentration develops a second step in its profile between the initial location of the interface and the leading edge of the front. The level of this intermediate step corresponds to the amount of the HEPES buffer accumulation in this area. As shown in Figure 4.6, even though the total molarity of the HEPES buffer is only 5 mM in the TE, the buffer species tend to accumulate behind the leading ITP front. This is because the buffer in this area consists primarily of negatively charged ions (L^-), as shown in Figure 4.7. The mobility of the L^- ions is smaller than the mobility of the Cl^- ions in the LE as well as the mobility of the dye (D^-) ions. The L^- ions therefore accumulate in this region, and their negative charge contribution is offset by the local Na^+ ions.

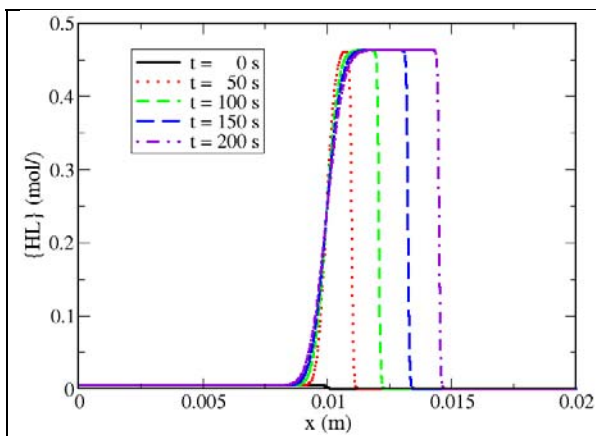


Figure 4.6: Evolution of the total buffer molarity.

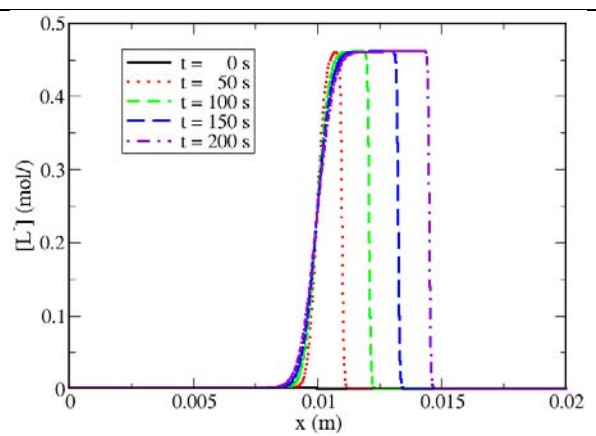


Figure 4.7: Evolution of the L^- concentration.

Figures 4.8 and 4.9 show the evolution of the H^+ concentration and the corresponding pH. Even though the solution started out with a uniform pH of 7, the pH rapidly increases to a value of over 11. This not only affects the composition of the HEPES buffer, it can also influence the fluorescence of the dyes used in the experiments.

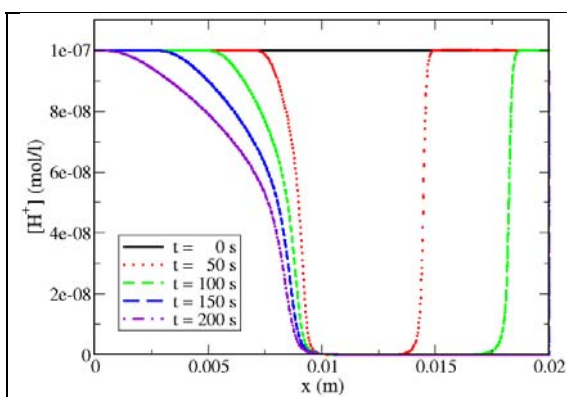


Figure 4.8: Evolution of the H^+ concentration.

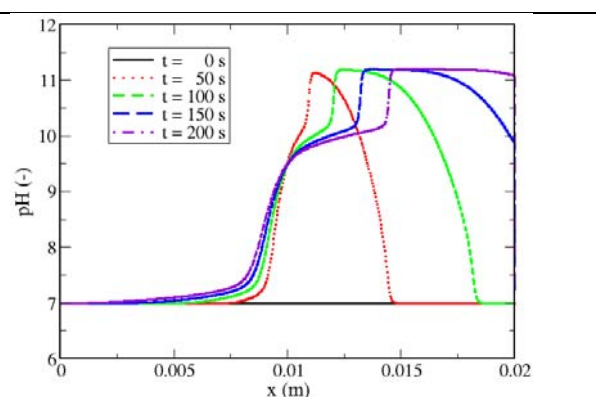


Figure 4.9: Evolution of the pH.

The evolution of the electrical conductivity field is shown in Figure 4.10. As the very mobile Na^+ and Cl^- ions dominate the solution, it is not surprising that the conductivity closely follows their profile, with a double step function. The electric field strength, however, does not show this step function, at least not on the scale of Figure 4.11. This is because the electrical conductivity is so much higher in the LE-stacking zone, as compared to the TE zone, that the potential drop (and corresponding field strength) in the LE-stacking zone are almost negligible. The transport of positive ions (by diffusion and electromigration) into the TE zone does result in a slight increase over time in the conductivity in this area. This results in a decrease of the overall resistance of the channel, with an (amplitude) increase of the field strength (and current) as a consequence. The behavior of the negatively charged dye (D^-) concentration is shown in Figure 4.11.

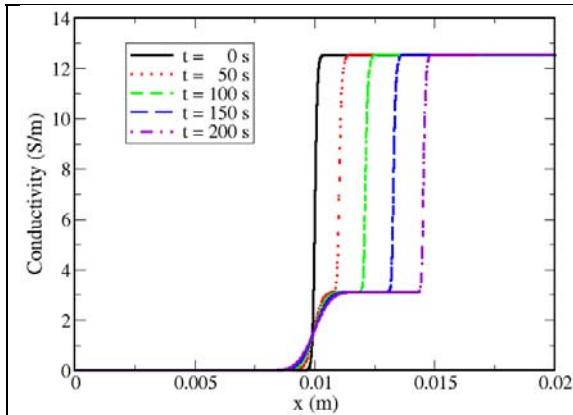


Figure 4.10: Evolution of the conductivity.

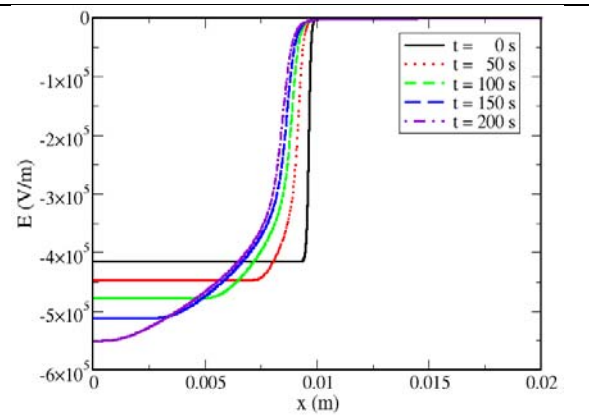
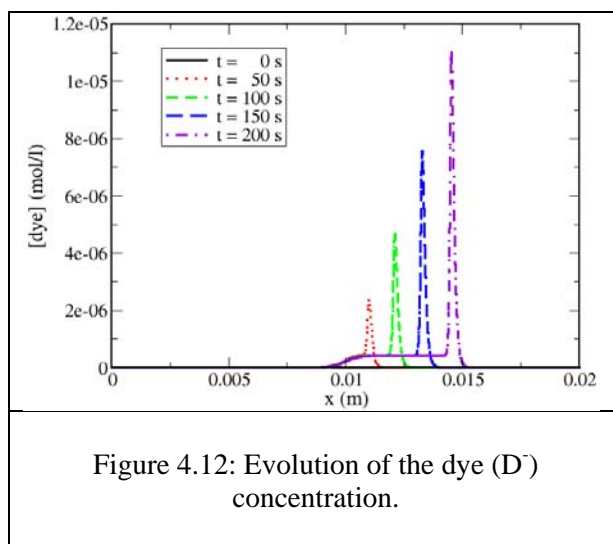


Figure 4.11: Evolution of the electric field strength.



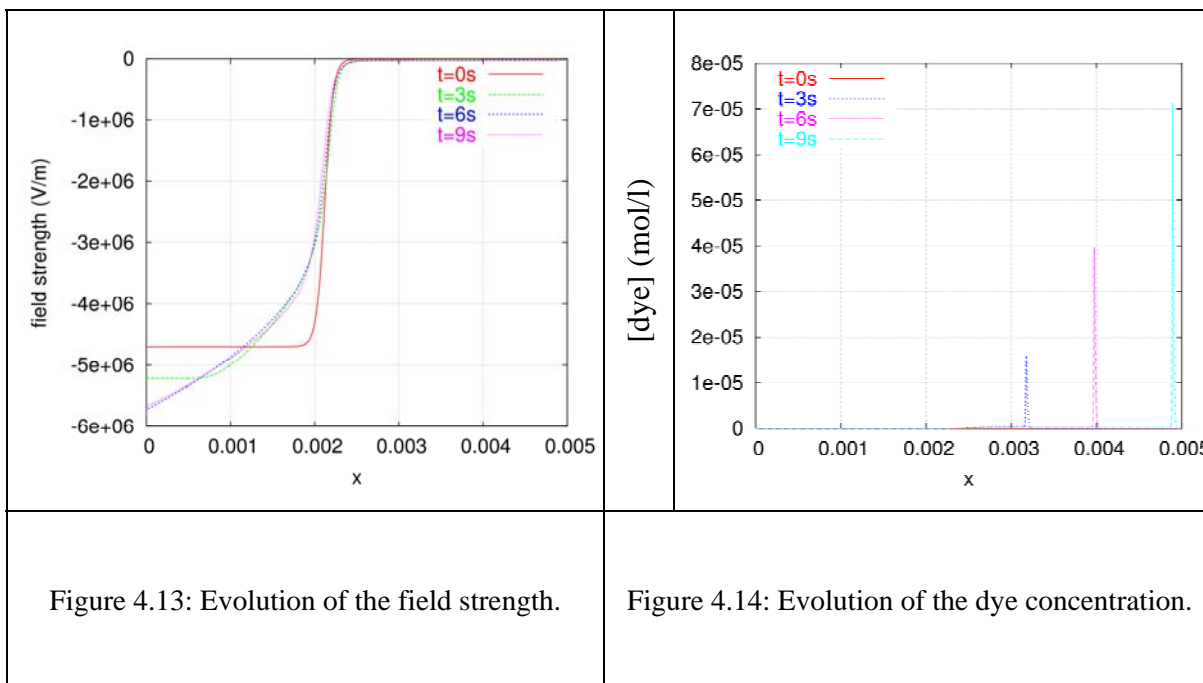
With an initial concentration of just 1 nM, the dye concentration at $t = 0$ s is not visible on this graph. However, as soon as the electric field is applied, the dye starts to stack behind the Cl^- front, and after 50 s, its concentration has already increased 2000-fold. After 200 s, the dye stacking ratio is a little larger than 11,000. Note that even after 200 s, the stacking continues without any sign of leveling off.

The simulated ion concentration profiles for this case compare qualitatively very well with the experimentally observed profiles. Nevertheless, it is clear that quantitatively, the observed stacking ratio of 11,000 for this case is much lower than the experimentally observed ratio of close to 10^6 . One difference with the experimental conditions is that, in the simulation, the initial concentration of the dye was set to 1 nM, while the experiments used an initial concentration of 1 pM in order to achieve such high stacking ratios. However, this is not expected to affect the initial rate of stacking or the empirically based expectation that the dye concentration should level off after ~ 100 s. This simulation shows no sign of such a steady state. To investigate whether the steady state shows up at higher values of the field strength, a case with a ten times higher field strength was simulated, as described in the next section.

Sample Stacking in 1D at 40 kV/cm

The case described in this section is identical to the one in the previous section, except for the fact that the channel was only 5 mm long, and an average field strength of 2 MV/m was described (resulting in a 40kV/cm effective field strength over the 2.5 mm of the domain that has the low conductivity buffer (TE zone)). Using a time step of $1 \mu s$, this case was simulated for a total of 9 seconds.

Figure 4.13 shows the electrical field strength for this case. The field strength starts off at a little over 40kV/cm in the TE zone, and increases to almost 60kV/cm as the resistance of the channel decreases over time. With this higher field strength, the dye concentration increases much faster than in the previous case, as seen in Figure 4.14. The dye begins to stack immediately, and continues to do so in a monotonic fashion. A stacking ratio of about 30,000 after 5 seconds, and about 70,000 after 9 seconds were observed. Note that, after an initial strongly nonlinear stage, stacking occurs at a slightly sublinear pace. Also, after 9 sec, no steady-state is in sight, similar to what was observed in the previous simulations.



Sample Stacking in 2D

The group also conducted ITP sample stacking studies in 2D under limited operating conditions, corresponding to low applied voltage difference and low LE molarity. The results do show stacking of the dye sample. For example, with applied 110 V/cm and a 0.01M NaCl solution, a stacking ratio of 30 after 2 sec, and 200 after 20 sec are found. However, the numerical construction, which is robust in 1D, encountered difficulties as stacking progressed in the 2D context, particularly with high applied voltage difference and salt concentration. The 2D construction is ultimately necessary to capture dispersion effects, and therefore is ultimately necessary to pursue. This is left as a matter for future work.

4.2.6 Conclusions and Future Work

The group has developed and implemented a detailed computational model for fundamental studies of isotachophoretic sample stacking in a microchannel. The construction accounts for fluid flow, electrochemistry, and HEPES buffer physics, including non-electroneutral bulk flow conditions. This construction was used to conduct parametric studies with the flow geometry and mixture conditions relevant in the Stanford experiments.

Sample stacking behavior using 1D studies were observed that is, in many respects, in good agreement with the experimental results. The detailed structure of the field quantities within and outside the stacking zone is generally in agreement with expected behavior. On the other hand, this agreement is mainly qualitative. Moreover, even qualitative agreement is limited to the early phase of stacking. One-dimensional results clearly do not replicate the observed plateau in stacking ratio seen in the experiments. Moreover, a rate of increase of the stacking ratio that is quantitatively less than that observed experimentally were computed.

Given the extent of detail in the physical models implemented, it can be concluded that the above disagreements are mainly due to the 1D nature of these computational results. Long-term 2D stacking studies at the relevant operating conditions remain a challenge, and are a subject for future work.

5.0 SUMMARY OF PROJECT IMPACT

This project had a very significant impact on the microfluidics, lab-on-a-chip and biosensor communities as a whole. In all, the project resulted in over 168 journal and conference papers, three inventions and patents (or patent applications), and trained 10 PhD's, three MS graduates, and helped trained six postdocs. The work funded as part of this project also led to six awards from conferences, national organizations, and the US government. In addition, this project funding and, more importantly, the associated technical accomplishments from this project contributed to the successful promotion to Associate Professor with tenure for two of the co-PIs involved in the effort (Myszka and Santiago). Three of these PhDs and postdocs are now faculty members at major universities and building a career on microfluidics research. Nine others are engineers, researchers, and/or managers concentrating on microfluidics research and development at either companies or national laboratories.

The models produced also resulted in significant technology transfer in the way of commercialized multiphysics code for the microfluidics. Our success in developing the fundamentals to extract accurate information from protein arrays led one of the co-PIs (Myszka) to help establish a micro fluidic-based company in Utah called Wasatch Microfluidics.

This section summarizes each of these accomplishments and ends with a complete listing of the 50 journal papers which resulted from this project.

5.1 Training of Future Leaders in Microfluidics

The following students obtained their MS (as their terminal degree) largely as a result of the work they conducted as part of this project:

MS Graduates from this Project:

- Brian Kidd, M.S. Mech. Eng., Stanford, April 2001 (now a Researcher, Stanford Medical School)
- Bruce P. Mosier, Eng. Deg, Mech. Eng., May 2001 (now a Research Scientist at Sandia National Labs, working on Microfluidics)

PhD Graduates from this Project:

The students below obtained their PhD (as their terminal degree) largely as a result of the work they conducted as part of this project. Also listed here is the PhD thesis title for each student.

- Chuan-Hua Chen, Ph.D., Mech. Eng., Stanford, Jan. 2004, Thesis Title: Microscale Electronkinetic Transport and Stability, Jan. 2004 (now a Research Scientist at Rockwell Scientific working on microfluidics)
- Amy Herr, Ph.D., Mech. Eng, Sept. 2002, Title: Isoelectric Focusing for Multi-Dimensional Separations in Microfluidic Devices, Aug. 2002 (currently a Research Scientist in microfluidics at Sandia National Labs; to start a faculty position at University of California at Berkeley working in Microfluidics)
- Josh I. Molho, , Ph.D. Mech. Eng., Stanford, Dec. 2001, Thesis Title: Electrokinetic Dispersion in Microfluidic Separation Systems (R&D Engineer and Manager at Caliper Technologies; a microfluidics company)
- Shankar Devasenathipathy, Thesis Title: Particle Imaging Diagnostics and Stacking Dynamics in Microfluidic Systems, Dec. 2003 (Researcher Intel Corporation; working on microfluidics for electronics cooling)
- Michael Oddy, Ph.D. Mech. Eng., Stanford, December 2004, Thesis Title: Electrokinetic Transport Phenomena: Mobility Measurement and Electrokinetic Instability, Feb. 2005 (Finance Quantitative Analyst, Barclays Capital)
- Rajiv Bharadwaj, Ph.D. Chem. Eng., Stanford, June 2005, Thesis Title: Microscale Electrokinetic Sample Stacking (currently R&D Engineer, Caliper Technologies; a microfluidics company)

- Shuhuai Yao, Ph.D. Mech. Eng., Stanford, Sept. 2005, Thesis Title: Theory, Design, and Demonstration of Electroosmotic Pump Technologies, Aug. 2005(Postdoctoral researcher at Sandia National Labs working on microfluidic devices for protein folding studies)
- Dahzi Wang, PhD 2003, University of California at Santa Barbara, Thesis,“ Micro PIV Measurements in AC Electrothermal Flow”.

Postdoctoral Researchers from this Project:

- Jim Mikkelsen, Ph.D. Chemistry, Brown Univ., left Stanford June 2002. (Scientist at Caliper Technologies working on microfluidics.)
- Peng Zhou, Ph.D. Mech. Eng., Stanford, left Stanford September 2003. (R&D Engineer, Cooligy, Inc.; a microfluidics company co-founded by Santiago.)
- Hao Lin, Ph.D., University of California at Berkeley, left Stanford June 2005. (Currently a tenure-track professor at Rutgers University working on microfluidics.)
- Jonathan D. Posner, Ph.D., Univ. of California at Irvine, left Stanford September 2005. (Currently a Professor, Arizona State University working on microfluidics.)
- Yasmina Abdiche, Ph.D., Biochemistry Oxford Univ., left Utah March 2005. (Currently a Senior Research Scientist at Pfizer Inc., applying expertise in biosensor technology to drug discovery.)
- Cheryl Baird, Ph.D., Biochemisty Univ. of Utah, left Utah in December 2004 to work on array-based biosensor technology at HTS Biosystems (Boston, MA). Currently works at Pacific Northwest National Laboratory on protein microarrays and novel detection platforms.

As mentioned above, co-PIs Myszka and Santiago also leveraged the technical accomplishments, publications, and funding from this project to earn promotion to Associate Professor with tenure in their respective institutions. Associate Professor and co-PI Meinhart received tenure a few months after notice of this award was given.

5.2 Technology Transfer

During the course of this project, several simulation models have been developed and implemented in CFD-ACE+. Using these models, several physical phenomena have been studied in detailed. These studies directly benefited the project members, as well as academic and industry community at large. These accomplishments are discussed in detail next:

Models Developed (an “M” prefix in the list below indicates a model developed as part of this project):

- M1. Particle dielectrophoresis models that include conventional DEP, traveling wave DEP, and electrorotation [29]
- M2. AC electrohydrodynamic phenomenon of electrothermal flows [16]
- M3. DC electroosmosis in systems with thick double layer [P23]
- M4. Slip boundary models for flow in hydrophobic microchannel systems [33, 34]
- M5. Models for EOF mobility variations as a function of pH for fused silica substrates[35]
- M6. Unit-cell based models for highly concentrated buffer solutions. Models predict following physical properties[P23]:
 - d. Electrophoretic mobility
 - e. Diffusion coefficient
 - f. Electrical conductivity
- M7. Integration of biochemistry models with particle DEP models [P45]
- M8. Joule heating[36]
- M9. Super LU solver for highly non-net neutral system[37]
- M10. Generalized surface chemistry models (beads and surfaces)[38]
- M11. Biochemistry database integrated with electrochemistry
- M12. Hydrogel models for surface biochemistry[30]
- M13. Least square-based engine for extraction of kinetic coefficients[38]
- M14. Rapid ANN based kinetic coefficient extraction algorithm (this has not been published yet)
- M15. Python based scripts to automate geometric generation for proteomic chips (these scripts are available from ESI-CFD, NA, Huntsville, AL)

The above models been validated with following analytical solutions (“S” indicates an analytical solution):

- S1. Joule heating in parallel plate
- S2. Particle DEP in periodic electrode array
- S3. Particle DEP in wedge shaped (conical) electrode system
- S4. Electrothermal flow in periodic electrode array
- S5. Ion transport near charged surface
- S6. EOF flow in arbitrary zeta potential and double layer thickness
- S7. All surface chemistry models

- S8. After validation, the models have been used extensively to study the following phenomena:
- S9. Sample dispersion under non-uniform zeta potential
- S10. Electrothermal flow in various electrode configurations and elucidate relative significance of electrothermal and DEP forces
- S11. Field Amplified Sample Stacking
- S12. Effect of slip at nano-scale on overall pressure drop in microfluidic systems
- S13. Manipulation of particles in AC electric fields using traveling wave DEP
- S14. Influence of double layer thickness, zeta potential and surface charges on EOF at nano-scale
- S15. Transport of analytes in highly concentrated buffer
- S16. Bead based immunoassays
- S17. Mass transport limitations on sensor performance
- S18. Effect of hydrogel layer on proteomic chip performance

5.2.1 Commercialization of Developed Technologies

Based on the knowledge and understanding of above physical phenomena, the team has designed and optimized various microfluidic devices such as:

- D1. Traveling wave DEP based Flow Field Fractionation device
- D2. Sample Stacking device
- D3. Tunable Laser Cavity (TLCC) sensor
- D4. Nanofluidic systems
- D5. HTS proteomic chip
- D6. BIACORE biosensors
- D7. Notional immunoassay based sensors

Design guidelines have been generated for engineers and scientists who work in this field. Besides, the simulation models have been implemented in CFD-ACE+ Version 2002, 2003 and 2004, and have been successfully marketed.

Commercial Release of Developed Software Capabilities: Both the electrokinetic models and the biochemical assay models have also been fully integrated into the commercial CFD-ACE+ code, along with the development of associated GUI, user manuals and tutorial test cases.

Master Classes for Advanced CFD-ACE+ Users: Sample test cases were also included based on these capabilities in the Master Classes (for advanced CFD-ACE+ users) for the Biochemistry

and the electrokinetic modules. These classes were taught at the Annual CFD-ACE+ Users Conference.

Multi-physics Courses: This material (test cases, tutorial examples, etc.) is also included in the following two Biotechnology industry-specific multiphysics courses being developed at CFDRC, which were offered starting November, 2001 in various locations around the country. The two courses offered dealt with: (a) design of biochemical assays in microfluidic systems, and (b) electrokinetic and electrochemistry applications in microfluidic systems. The objective of these courses was to facilitate rapid learning and confidence building in existing and new users of the current software by discussing theoretical background (adequate physical models, data sources, and boundary conditions), optimal computational strategies, model set-up protocols of CFD-ACE+, and expected results (accuracy, speed, uncertainty).

5.2.2 Patents

The following is a list of patents and patent applications resulting from this project. The “I” prefix in the numbers below indicate an invention resulting in a patent application:

- I1. Santiago, J.G., M. Oddy, and J.C. Mikkelsen, 2001. “Electrokinetic Instability Micromixer,” Patent Application No. 20020125134, September 12, 2002.
- I2. Santiago, J.G., and B. Jung, “A Novel Sample Stacking Capillary Electrophoresis Device,” Applied for provisional patent, 2003.
- I3. Santiago J.G., B. Jung, and R. Bharadwaj, "Microfluidic Sample Stacking Method Using Single-Interface Isotachophoresis", Applied for provisional patent, 2006.

5.3 Awards and Honors

The following awards and honors resulted at least in part from the research conducted and inventions produced as part of this project:

- Santiago elected Co-Chair of Gordon Conference on the Physics and Chemistry of Microfluidics, Oxford, England (planning for conference in August, 2007), 2005 (this honor is a general recognition of the success of the current microfluidics work)
- Santiago group: Best Poster in session award, Gordon Conference on the Physics and Chemistry of Microfluidics, Oxford England, 2005 (on electrokinetic instability)
- Santiago: Presidential Early Career Award for Scientist and Engineers (PECASE), 2004 (This is the highest award by the US Government to scientist starting their career; it was awarded for the Santiago group’s work on electrokinetic instabilities and sample stacking)
- Santiago and Huber, Best Poster award Annual Meeting of the American Institute of Chemical Engineering and American Electrophoresis Society, San Francisco, California, 2003 (on sample stacking work)

Santiago's group received a Best Poster award Gordon Conference on the Physics and Chemistry of Microfluidics, Big Sky Montana 2003 (on sample stacking work)

Santiago and M Oddy won a National Inventors Hall of Fame Collegiate Inventors Award, 2001 (on the design of an electrokinetic instability micromixer)

5.4 Complete List of Publications Resulting from this Project

The "P" prefix in the numbered list below indicates a publication (journal paper or conference paper) resulting from this project:

Stanford Publications and Presentations

- P1. Jung, B., Zhu, Y., and J.G. Santiago, "Detection of 100 attomolar Fluorophores Using a High Sensitivity On-Chip CE System and Transient Isotachopheresis," submitted to *Analytical Chemistry*, 2006.
- P2. Jung, B., Bharadwaj, R., Santiago, J.G., "On-Chip Million-Fold Sample Stacking Using Single-Interface Isotachopheresis," Vol. 78, No. 7, *Analytical Chemistry*, pp. 2319-2327, 2006.
- P3. Bharadwaj, R. and J.G. Santiago, "Dynamics of Field Amplified Sample Stacking," *Journal of Fluid Mechanics*, Vol. 543, 57-92, 2005.
- P4. Lin, H., Storey, B., M. Oddy, Chen, C.-H., and J.G. Santiago, "Instability of Electrokinetic Microchannel Flows with Conductivity Gradients," *Physics of Fluids*, Vol. 16, No. 6, 2004
- P5. Alexis-Alexandre, G., B. Mohammadi, J.G. Santiago, and R. Bharadwaj, "Microfluidic Flow Simulations: Stacking One-Dimensional Study," *Houille Blanche-Revue Internationale De Leau*, No. 5, pp. 18-23, 2003.
- P6. Jung, B., R. Bharadwaj, and J.G. Santiago, "Thousand-Fold Signal Increase using Field Amplified Sample Stacking for On-Chip Electrophoresis," *Electrophoresis*, Vol. 24, No. 19-20, pp. 3476-3483, 2003
- P7. Herr, A.E., J.I. Molho, K.A. Drouvalakis, J.C. Mikkelsen, P.J. Utz, J.G. Santiago, and T.W. Kenny, "On-Chip Coupling of Isoelectric Focusing and Free Solution Electrophoresis for Multi-Dimensional Separations," *Analytical Chemistry*, Vol. 75, No. 5, pp. 1180-1187, 2003.
- P8. Devasenathipathy, S., J.G. Santiago, S.T. Wereley, and C.D. Meinhart, "Particle Tracking Techniques for Microfabricated Fluidic Systems," *Experiments in Fluids*, Vol. 34, No. 4, pp. 504-513, 2003
- P9. Chen, C.-H., Lin, H., Lele, S.K. & Santiago, J.G., "Convective and absolute electrokinetic instability with conductivity gradients", *Journal of Fluid Mechanics*, 524, pp. 263 – 303, 2005.
- P10. Bharadwaj, R., J.G. Santiago, and B. Mohammadi, "Design and Optimization of On-Chip Capillary Electrophoresis," *Electrophoresis*, Vol. 23, pp. 2729-2744, 2002
- P11. Mosier, B.P., J.I. Molho, and J.G. Santiago, "Bleached-Fluorescence Imaging of Microflows," *Experiments in Fluids*, Vol. 33, No. 4, pp. 545-554, 2002

- P12. Devasenathipathy, S., J.G. Santiago, and K. Takehara, " Particle Tracking Techniques for Electrokinetic Microchannel Flows," *Analytical Chemistry*, Vol. 74, No. 15, pp. 3704-3713, 2002
- P13. Chen, C.H., and J.G. Santiago, "Electrokinetic Instability in High Concentration Gradient Microflows", ASME International Mechanical Engineering Congress & Exposition, MEMS and Nanotechnology Symposium, November 17-22, 2002, New Orleans.
- P14. Devasenathipathy, S., R. Bharadwaj, and J.G. Santiago, "Investigation of field amplified sample stacking with particle image velocimetry," ASME International Mechanical Engineering Congress & Exposition, MEMS and Nanotechnology Symposium, November 17-22, 2002, New Orleans.
- P15. Bharadwaj, R., J.G. Santiago, and B. Mohammadi, "Design and Optimization of On-Chip Capillary Electrophoresis," *Electrophoresis*, Vol. 23, pp. 2729-2744, 2002.
- P16. Devasenathipathy, S. and J.G. Santiago, "Electrokinetic Flow Diagnostics," in press, *Microdiagnostics*, New York, Springer Verlag, 2002.
- P17. Devasenathipathy, S., J.G. Santiago, and K. Takehara, " Particle Tracking Techniques for Electrokinetic Microchannel Flows," Vol. 74, No. 15, pp. 3704-3713, *Analytical Chemistry*, 2002.
- P18. Mosier, B.M., J.I. Molho, and J.G. Santiago, "Bleached-Fluorescence Imaging of Microflows," in press, *Experiments in Fluids*, 2002.
- P19. Mohammadi, B., J.I. Molho, J.G. Santiago, "Incomplete Sensitivities in the Design of Minimal Dispersion Fluidic Channels," in press, *Computational Methods in Applied Mechanics and Engineering*, 2002.
- P20. Devasenathipathy, S., J.G. Santiago, S.T. Wereley, and C.D. Meinhart, "Particle Tracking Techniques for Microfabricated Fluidic Systems," submitted to the *Experiments in Fluids*, 2001.
- P21. Oddy, M.H., J.G. Santiago, and J.C. Mikkelsen, Jr., "Electrokinetic Instability Micromixing," Vol. 73, *Electrokinetic Instability Micromixing*, pp. 5822-5832, 2001.
- P22. Mohammadi, B., J.G. Santiago, "Simulation and design of extraction and separation fluidic devices", *Mathematical Modelling and Numerical Analysis*, Vol. 35, No. 3, pp. 513-523, 2001.
- P23. Santiago, J.G., "Electroosmotic Flows in Microchannels with Finite Inertial and Pressure Forces," *Analytical Chemistry*, Vol. 73, No. 10, pp. 2353-2365, 2001.
- P24. Bharadwaj, R., B. Mohammadi, and J.G. Santiago, "Incomplete Sensitivities in Design and Control of Fluidic Channels," Center for Turbulence Research, Stanford University, Annual Research Briefs, 2001.
- P25. Bharadwaj, R. and J.G. Santiago, "Dynamics of Field Amplified Sample Stacking," Proceedings of the International Mechanical Engineering Congress and Exposition, Sixth Micro-Fluidic Symposium, New York, New York, 2001.

- P26. Oddy, M.H., J.G. Santiago, and J.C. Mikkelsen, Jr., "An Electrokinetic Instability Micromixer," Proceedings of the International Mechanical Engineering Congress and Exposition, Sixth Micro-Fluidic Symposium, New York, New York, IMECE2001/MEMS-23882, 2001.
- P27. Herr, A.E., J.I. Molho, R. Bharadwaj, J.G. Santiago, and T.W., Kenny, "Miniaturized Isoelectric Focusing as a Component of a Multi-dimensional Separation System," Fifth International Symposium on Micro Total Analysis Systems (μ TAS) Monterey, California, pp. 51-53, 2001.
- P28. Bharadwaj, R. and J.G. Santiago, "Optimization of Field Amplified Sample Stacking on a Microchip," Fifth International Symposium on Micro Total Analysis Systems (μ TAS) Monterey, California, pp. 613-614, 2001.
- P29. Oddy, M.H., J.G. Santiago, and J.C. Mikkelsen, Jr., "Electrokinetic Instability Micromixing," Fifth International Symposium on Micro Total Analysis Systems (μ TAS) Monterey, California, 2001.
- P30. Chen, C.-H., J.C. Mikkelsen, Jr., J.G. Santiago, "Electrophoretic Band Crossing for Measurements of Biomolecular Binding Kinetics," Technical Digest of International Forum on Biochip Technologies, , 2000.Beijing, China, pp. 441-442, Oct 11-14 2000.
- P31. Herr, A.E., J.C. Mikkelsen, Jr., J.G. Santiago, T.W., Kenny, "Electroosmotic Flow Suppression and its Implications for A Miniaturized Full-Field Detection Approach to Capillary Isoelectric Focusing (cIEF)," Proceedings of ASME 2001 Winter Annual Meeting, Fifth Micro-Fluidic Symposium, International Mechanical Engineering Congress and Exposition, Orlando, Florida, MEMS Vol. 2, pp. 513-518, 2000.
- P32. Mosier, B.P., J.C. Mikkelsen, Jr., J.G. Santiago, " A Novel Bleached Fluorescence Imaging Technique for Microfluidics," Fifth Micro-Fluidic Symposium, International Mechanical Engineering Congress and Exposition, Orlando, Florida, 2000.
- P33. Devasenathipathy, S., J.I. Molho, J.C. Mikkelsen Jr., J.G. Santiago, "Electroosmotic Flow Field Measurements with Particle Image Velocity," Fifth Micro-Fluidic Symposium, International Mechanical Engineering Congress and Exposition, Orlando, Florida, 2000.
- P34. Herr, A.E., J.I. Molho, J.G. Santiago, T.W. Kenny, D. A. Borkholder, G.J. Kintz, P. Belgrader, M. A. Northrup, "A Miniaturized Full-Field Array Detection Approach to Protein Separations Using Capillary Isoelectric Focusing (cIEF)," Proceedings of the Micro Total Analysis Systems Symposium, Enschede, The Netherlands, pp. 367-370, 2000.

CFDRC Corporation Publications and Presentations

- P35. Przekwas, A. J. and V. B. Makhijani, "Mixed-Dimensionality, Multi-Physics Simulation Tools for Design Analysis of Microfluidic Devices and Integrated Systems", In: Technical Proc. 4th International Conf. On Modeling and Simulation of Microsystems (MSM 2001), Hilton Head, SC, Laudon, M and Romanowicz, B, (Eds.), Computational Publications, Cambridge, MA, pp. 198-201, 2001.
- P36. V. B. Makhijani and S. Sundaram, "High-fidelity Computational Modeling and Analysis of Sensors for Biowarfare Agent Detection", presented at Lockheed Martin NESS, Manassas, VA, May 2, 2001.
- P37. A. K. Singhal and V. B. Makhijani, "Growing Role of Multi-Physics Simulations for Rapid Development of Micro-Reaction and Bio-Analytical Systems", In Proc. 5th International Conf. on Microreaction Technology (IMRET5), Strasbourg, France, May 27-30, 2001.
- P38. S. Krishnamoorthy, J.J. Feng & V. B. Makhijani, "Full-Scale Computational Study Of Electrophoretic Systems", In. Proc Electrochemical Society 2001 Joint International Meeting San Fransisco, CA, Sept. 4, 2001.
- P39. S. Krishnamoorthy and M. Shariati, "CFD-ACE+: Multi-Physics Simulation Software for Computer-Aided Design and Optimization of Biochip Systems", Presented at Caliper Technologies Corporation, Mountain View, CA, Sept. 5, 2001.
- P40. S. Krishnamoorthy and M. Shariati, "CFD-ACE+: Multi-Physics Simulation Software for Computer-Aided Design and Optimization of Biochip Systems", Presented at Lynx Therapeutics, Inc., Hayward, CA, Sept. 6, 2001.
- P41. J. Feng, S. Krishnamoorthy and V. B. Makhijani, "Simulation of Dielectrophoresis of Particles Near Microelectrodes", In: Proc. Labautomation 2002, Palm Springs, CA, Jan. 27 -29, 2002.
- P42. Feng, J. J., Blosch, E., Krishnamoorthy, S. and Makhijani, V. B., "Computational Analysis of Electrokinetic Transport in Lab-On-a-Chip Systems", In: Proc. IBC's 8th Annual International Microtechnology Event, Chips to Hits '01, San Diego, CA, Oct. 28th – Nov. 1st, 2001.
- P43. Prabhakarandian, B., Jenkins, J., Sundaram, S. and Makhijani, V. B., "Multi-Physics Simulations For The Design of Novel and Optimal Biosensors & Biodiagnostics Systems", In: Proc. IBC's 8th Annual International Microtechnology Event, Chips to Hits '01, San Diego, CA, Oct. 28th – Nov. 1st, 2001.
- P44. Krishnamoorthy, S., Feng, J. J., Chen, Z. J. and Makhijani, V. B., "Numerical and Analytical Studies of AC Electric Field in Dielectrophoretic Electrode Arrays", In: Proc. 5th International Conference on Modeling and Simulation of Microsystems (MSM 2002), San Juan, Puerto Rico, April 22-25, 2002.
- P45. Prabhakarandian, B., Shah, K. B., Sundaram, S. and Makhijani, V. B., "Biochemical Binding in Microspheres-Based Immunoassays", In: Proc. 5th International Conference on Modeling and Simulation of Microsystems (MSM 2002), San Juan, Puerto Rico, April 22-25, 2002. V.B.Makhijani, S.Sundaram, B.P.Pandian, and S. Krishnamoorthy, "Multidisciplinary Simulation Software for Design Analysis and

- Optimization of Microfluidics Devices and Biomolecular Assays BioMEMS 2002 April 25-26 Boston, MA.
- P47. Sigurdson, M., Meinhart, C., Wang, D., Liu, X., Feng, J. J., Krishnamoorthy, S., and Makhijani, V. B., "Transport Enhancement in Tunable Laser Cavity Sensor", ASME IMECE 2002, New Orleans, Louisiana.
- P48. Krishnamoorthy, S., "Multiphysics-Based Simulation Tool for Biochip Design", Presented at NASA-Glenn, June 2002.
- P49. Feng, J.J, Krishnamoorthy, S., and Sundaram, S. "Numerical Simulation of Field Amplified Sample Stacking in Microfluidic Systems", Submitted to 6th International Conference on Modeling and Simulation of Microsystems (MSM 2003), San Francisco, CA.
- P50. Jenkins, J.W. and Sundaram, S. "Applied Metrology using Multiphysics Simulations of Microsystems", Nano And Microsystems Technology And Metrology Conference, Huntsville AL, December 2002.
- P51. Sundaram, S., *CFDRC Biochip and Microfluidics Design Seminar Series*, September 24, (2003) San Diego, CA and September 25, (2003) Sunnyvale, CA.
- P52. Krishnamoorthy, S., *CFDRC Biochip and Microfluidics Design Seminar Series*, October 1, (2003) Boston, MA.
- P53. Feng, J.J et. al, "Simulation of electrokinetic flows in Microsystems" (Paper under preparation).
- P54. S. Sundaram, " Protein Interactions in Flow-based Biosensors," Applied & HTS Biosystems, Bedford MA
- P55. S. Krishnamoorthy, J. J. Feng and S. Sundaram, "Modeling and Simulation of Electrokinetic Transport Phenomena in Lab-on-a-Chip Systems", Small Talk 2003, San Jose, CA (2003).
- P56. S. Sundaram, "Simulation and Modeling for Microfluidic Systems", Course & Pre-conference Workshop, Small Talk 2003, San Jose, CA.
- P57. J. J. Feng, S. Krishnamoorthy, G. R. Wang, and S. Sundaram, "Simulation of Electrokinetic Flow and Analyte Transport in Nano Channels," *Technical Proceedings of the 2006 NSTI Nanotechnology Conference and Trade Show, Volume 2*, vol. 2, pp. 505-508, 2006
- P58. . Krishnamoorthy, A. S. Bedekar, J. J. Feng, and S. Sundaram, "Need for Simulation-Based Design Analysis and Optimization," *JALA - Journal of the Association for Laboratory Automation*, vol. 11, pp. 118, 2006
- P59. J. J. Feng, S. Krishnamoorthy, and S. Sundaram, "Numerical and analytical studies of electrothermally induced flow and its application for mixing and cleaning in microfluidic systems," Boston, MA, United States, 2004
- P60. J. J. Feng, S. Krishnamoorthy, S. Sundaram, R. Bharadwaj, and J. G. Santiago, "Numerical simulation of field amplified sample stacking in microfluidic system," San Francisco, CA, United States, 2003
- P61. M. Sigurdson, C. Meinhart, D. Wang, X. Liu, J. J. Feng, S. Krishnamoorthy, and S. Sundaram, "AC electrokinetics for microfluidic immunosensors," Washington, DC, United States, 2003

- P62. J. J. Feng, S. Krishnamoorthy, Z. J. Chen, and V. B. Makhijani, "Numerical and analytical studies of ac electric field in dielectrophoretic electrode arrays," San Juan, Puerto Rico, 2002
- P63. M. Sigurdson, C. Meinhart, D. Wang, X. Liu, J. J. Feng, S. Krishnamoorthy, and V. B. Makhijani, "Transport enhancement in tunable laser cavity sensor," New Orleans, LO, United States, 2002

ACLARA Publications and Presentations

- P64. *Fabrication and Applications of Highly Parallel Disposable Microfluidic Arrays*, A. J. Ricco, *SmallTalk Conference and Exhibition*, San Diego, 8/27-31/01.
- P65. *Plastic Microfluidic Devices for DNA Sequencing and Protein Separations*, H. Z. Fan, W. Tan, H. Tan, C. X. Qiu, T. D. Boone, P. Kao, A. J. Ricco, M. Desmond, S. Bay, and K. Hennessy, *Fifth International Conference on Miniaturized Chemical and Biochemical Analysis Systems* (μ TAS 2001), Monterey, 10/21-25/01.
- P66. *Multiplexed Microfluidic Analyses for Proteomics using LabCard™ Devices*, H. Salimi-Moosavi, J. Wallweber, H. Tahir, H. Hooper, H. Kirakossian, and S. Singh, *Fifth International Conference on Miniaturized Chemical and Biochemical Analysis Systems* (μ TAS 2001), Monterey, 10/21-25/01.
- P67. *Functional and Efficient Electrode-Integrated Microfluidic Plastic Devices*, M. Zhao, A. J. Ricco, U. Nguyen, R. M. Crooks, and Q. Zhu, *Fifth International Conference on Miniaturized Chemical and Biochemical Analysis Systems* (μ TAS 2001), Monterey, 10/21-25/01.
- P68. *Disposable Plastic Microfluidic Arrays for Applications in Biotechnology* (Invited), A. J. Ricco, *Applications of Microsystems and Nanotechnology to the Life Sciences*, Banff, Canada, 11/11-13/01.
- P69. *Application of Disposable Plastic Microfluidic Device Arrays with Customized Chemistries to Multiplexed Biochemical Assays* (Invited), A. J. Ricco, T. D. Boone, Z. H. Fan, I. Gibbons, T. Matray, S. Singh, H. Tan, T. Tian, and S. J. Williams, *Staying Healthy with Chips Symposium*, December Meeting of the Biochemical Society, University of York, York, UK, 12/17-19/01.
- P70. *Multiplexed Sensing and Genetically Specific Identification of BW Agents on a Plastic BioFLIP*, A. J. Ricco, Z. H. Fan, C. Koh, S. Singh, T. Tian, M. Zhao, Q. Zhu, D. Albagli, R. Anderson, T. Boone, Y. Juang, H. Kirakossian, C. Koh, A. Meng, H. Salimi-Moosavi, H. Nguyen, and W. Tan, *DARPA BioFLIPS/SimBioSys Principal Investigators' Meeting*, Palm Beach, 2/20/02
- P71. *Multiplexed Bioassays using Customized Disposable Microfluidic Systems* (Invited), A. J. Ricco, *The Pittsburgh Conference*, New Orleans, 3/17-22/02.
- P72. *Plastic BioMEMS Microfluidic Device Arrays for Bioassay Applications*, A. J. Ricco, *MRS 2002 Spring Meeting*, San Francisco, 4/1-5/02.

- P73. *Plastic Microfluidic Arrays Manufactured using Microfabrication Technology: Bioassay Applications*, A. J. Ricco, BIOMEMS 2002 - Advances in Medical and Analytical Applications, Cambridge, 4/25-26/02.
- P74. *Multiplexed Recognition and Genetically Specific Identification of Biological Hazards on A Plastic Microfluidic Device* [“open” poster session], A. J. Ricco, Z. H. Fan, W. Tan, M. Zhao, C.-G. Koh, T. D. Boone, J. Wallweber, H. Salimi-Moosavi, T. Matray, and S. Singh, Solid-State Sensor, Actuator, and Microsystems Workshop, Hilton Head Island, 6/3-6/02.
- P75. *Use of “Floating” Electrodes during Stacking to Increase the Sensitivity of Detection: Simulation and Experimental Results*, R. T. Kurnik, A. J. Ricco, T. D. Boone, S. J. Williams, U. Nguyen, and A. Wainright, SmallTalk Conference and Exhibition, Society for Laboratory Automation, San Diego, 7/27-31/02.
- P76. *Plastic Microfluidic Devices for DNA Sequencing and Protein Separations*, H. Z. Fan, W. Tan, H. Tan, C. X. Qiu, T. D. Boone, P. Kao, A. J. Ricco, M. Desmond, S. Bay, and K. Hennessy, *Micro Total Analysis Systems 2001*, Kluwer: Boston (2001); pp. 19-21.
- P77. *Multiplexed Microfluidic Analyses for Proteomics using LabCard™ Devices*, H. Salimi-Moosavi, J. Wallweber, H. Tahir, H. Hooper, H. Kirakossian, and S. Singh, *Micro Total Analysis Systems 2001*, Kluwer: Boston (2001); pp. 483-485.
- P78. *Functional and Efficient Electrode-Integrated Microfluidic Plastic Devices*, M. Zhao, A. J. Ricco, U. Nguyen, R. M. Crooks, and Q. Zhu, *Micro Total Analysis Systems 2001*, Kluwer: Boston (2001); pp. 193-194.
- P79. *Application of Disposable Plastic Microfluidic Device Arrays with Customized Chemistries to Multiplexed Biochemical Assays*, A. J. Ricco, T. D. Boone, Z. H. Fan, I. Gibbons, T. Matray, S. Singh, H. Tan, T. Tian, and S. J. Williams, *Biochem. Soc. Transactions*, 30(2), 73–78 (2002).
- P80. *Plastic Advances Microfluidic Devices*, T. D. Boone, Z. H. Fan, I. Gibbons, A. J. Ricco, H. Tan, S. J. Williams, *Anal. Chem.*, 74, 78A–86A (2002).
- P81. *Use of Floating Electrodes in Transient Isotachophoresis to Increase the Sensitivity of Detection*, R. T. Kurnik, T. D. Boone, U. Nguyen, A. J. Ricco, and S. J. Williams, *Lab Chip*, 3, 86–92 (2003).
- P82.

Follow-up ACLARA publication not supported by DARPA funding:

- P83. *Multiplex mRNA Assay Using Electrophoretic Tags for High-Throughput Gene Expression Analysis*, H. Tian, L. Cao, Y. Tan, S. Williams, L. Chen, T. Matray, A. Chenna, S. Moore, V. Hernandez, V. Xiao, M. Tang, and S. Singh, *Nucleic Acids Research*, 32, e126 (2004).

University of Utah Publications and Presentations

- P84. He X, Coombs D, Myszka DG, Goldstein B. A theoretical and experimental study of competition between solution and surface receptors for ligand in a BIACORE flow cell.
- P85. Bull Math Biol. 2006 Jul;68(5):1125-50.
- P86. Katsamba PS, Navratilova I, Calderon-Cacia M, Fan L, Thornton K, Zhu M, Bos TV, Forte C, Friend D, Laird-Offringa I, Tavares G, Whatley J, Shi E, Widom A, Lindquist KC, Klakamp S, Drake A, Bohmann D, Roell M, Rose L, Dorocke J, Roth B, Luginbuhl B, Myszka DG. Kinetic analysis of a high-affinity antibody/antigen interaction performed by multiple BIACORE users. Anal Biochem. 2006 May 15;352(2):208-21..
- P87. Safsten P, Klakamp SL, Drake AW, Karlsson R, Myszka DG. Screening antibody-antigen interactions in parallel using BIACORE A100. Anal Biochem. 2006 Jun 15;353(2):181-90..
- P88. Karlsson R, Katsamba PS, Nordin H, Pol E, Myszka DG. Analyzing a kinetic titration series using affinity biosensors. Anal Biochem. 2006 Feb 1;349(1):136-47.
- P89. Navratilova I, Eisenstien E, Myszka DG. Measuring long association phases using BIACORE. Anal Biochem. 2005 Sep 15;344(2):295-7.
- P90. Cannon MJ, Papalia GA, Navratilova I, Fisher RJ, Roberts LR, Worthy KM, Stephen AG, Marchesini GR, Collins EJ, Casper D, Qiu H, Satpaev D, Liparoto SF, Rice DA, Gorshkova II, Darling RJ, Bennett DB, Sekar M, Hommema E, Liang AM, Day ES, Inman J, Karlicek SM, Ullrich SJ, Hodges D, Chu T, Sullivan E, Simpson J, Rafique A, Luginbuhl B, Westin SN, Bynum M, Cachia P, Li YJ, Kao D, Neurauter A, Wong M, Swanson M, Myszka DG. Comparative analyses of a small molecule/enzyme interaction by multiple users of BIACORE technology. Anal Biochem. 2004 Jul 1;330(1):98-113.
- P91. Myszka DG. Analysis of small-molecule interactions using BIACORE S51 technology.
- P92. Anal Biochem. 2004 Jun 15;329(2):316-23.
- P93. Myszka DG, Abdiche YN, Arisaka F, Byron O, Eisenstein E, Hensley P, Thomson JA, Lombardo CR, Schwarz F, Stafford W, Doyle ML. The ABRF-MIRG'02 study: assembly state, thermodynamic, and kinetic analysis of an enzyme/inhibitor interaction.
- P94. J Biomol Tech. 2003 Dec;14(4):247-69.
- P95. Cannon, M. J. and Myszka, D. G. (accepted) "Analyzing the binding of low molecular mass compounds using BIACORE S51", *Recent Research Developments in Biophysics and Biochemistry*.
- P96. Myszka, D. G. and Rich, R. L. (2003) "SPR's high impact on drug discovery: resolution, throughput, and versatility", *Drug Discovery World Spring 2003*, 1-5.
- P97. Xu G., Rich, R. L., Steegborn, C., Min, T., Huang, Y., Myszka, D. G., Wu, H. (2003) "Mutational Analyses of the p35/caspase Interaction. A bowstring kinetic model of caspase inhibition by P35", *J. Biol. Chem.* 278, 5455-5461.

- P98. Stenlund, P., Babcock, G. J., Sodroski, J. and Myszka, D. G. (2003) "Capture and reconstitution of G protein-coupled receptors on biosensor surfaces", *Anal. Biochem.* 316, 243-250.
- P99. Long, S. D. and Myszka, D. G. (2003) "Affinity-based optical biosensors", *Affinity Chromatography*. In press.
- P100. Evans-Galea, M. V., Blankman, E., Myszka, D. G., Bird, A. J., Eide, D. J., Winge, D. R. (2003) "Two of the five zinc fingers in the Zap1 transcription factor DNA binding domain dominate site-specific DNA binding", *Biochemistry* 42, 1053-1061.
- P101. Myszka, D. G., "Biosensing in the nth degree" IBC antibody engineering conference.
- P102. Rich, R. L. and Myszka, D. G., (2003) "Spying on HIV with SPR biosensors", *Trends in Microbiology* 11, 124-133.
- P103. Myszka, D. G., "High-resolution screening using BIACORE S51 technology", Society for Biomolecular Screening, The Hague, Netherlands.
- P104. Myszka, D. G., "Advanced application of SPR biosensors", NCI Fredrick, MD.
- P105. Myszka, D. G., "Array-based biosensor technology", HTS Biosystems, Hartford, CT.
- P106. Myszka, D. G., "Advanced biosensor data modeling", Data Analysis Workshop, University of New Hampshire.
- P107. Day Y. S. N. & Myszka D. G. (2003) "Characterizing a drug's primary binding site on albumin", *Journal of Pharmaceutical Science* 92, 333-343.
- P108. Ekstrom, J. L., Pauly, T. A., Carty, M. D., Soeller, W. C., Culp, J., Danley, D. E. Hoover, D. J., Treadway, J. L., Gibbs, E. M., Fletterick, R. J., Day, Y. S. N., Myszka, D. G., and Rath, V. L. (2002) "Structure-activity analysis of the purine-binding site of human liver glycogen phosphorylase", *Chem. Biol.* 9, 915-924.
- P109. Bajji, A. C., Sundaram, M., Myszka, D. G., Davis, D. R. (2002) "An RNA Complex of the HIV-1 A-Loop and tRNA(Lys,3) is Stabilized by Nucleoside Modifications" *J. Am. Chem. Soc.* 124, 14302-14303.
- P110. Baird C. L., Courtenay E. S., & Myszka D. G. (2002) "Surface plasmon resonance characterization of drug/liposome interactions", *Anal. Biochem.* 310, 93-99.
- P111. Myszka, D. G., "Improving biosensor analysis", BIACORE User Group Meeting, Atlanta GA.
- P112. Myszka, D. G., "Independent analysis of a biomolecular interacting system" (in preparation), *Journal of Biomolecular Techniques*.
- P113. Liparoto F. S., Myszka D. G., Wu Z., Goldstein B., Laue T. M. & Ciardelli T. L. (2002) "Analysis of the role of the interleukin-2 receptor gamma chain in ligand binding", *Biochemistry* 41: 2543-2551.
- P114. Rich R. L., Hoth L. R., Geoghegan K. F., Brown T. A., LeMotte P. K., Simons S. P., Hensley P. & Myszka D. G. (2002) "Kinetic analysis of estrogen receptor/ligand interactions", *PNAS*, 99: 8562-8567.
- P115. Myszka, D. G., "Advanced Biosensor Analysis", Protein Science Society of Japan, Nagoya Japan.
- P116. Myszka, D. G., "The Basics of Biosensor Technology", Shanghai Teachers Institute, Shanghai China.
- P117. Rich R. L. & Myszka D. G. (2002) "Survey of the year 2001 commercial optical biosensor literature", *J. Mol. Recog.* 15, 352-376.

- P118. Myszka, D. G., "BIACORE Technology: Past, Present and Future", BIACORE Symposium, Chicago, IL.
- P119. Myszka, D. G., "Biosensors and Drug Discovery", Symposium on Solution Interactions, Antigenics, Boston MA.
- P120. Myszka, D. G. "Optical Biosensor Technology", CDFRC Huntsville AL.
- P121. Myszka, D. G. "The Evolution of Biosensor Technology", MDS Sciex, Toronto, Canada.
- P122. Myszka, D. G., "MIRG 2002: Validation Program for Biomolecular Interactions", Association of Biomolecular Resource Facilities, Austin, TX.
- P123. Myszka, D. G., "Biosensor Technology as a Biophysical Tool", Gordon Conference on Reversible Associations.
- P124. Myszka, D. G. "Improvements in Biosensor Experimental Design", University of Pittsburgh.
- P125. Myszka, D. G. "Fluidic Dynamics in Array Biosensors", SomaLogic Inc. and HTS Biosystems.
- P126. Myszka, D. G. "Validating Rate Constants from SPR Biosensors", *New Approaches to Solution Interactions of Biological Molecules*, Keihanna Plaza, Kyoto, JAPAN, 2002.
- P127. Katsamba, P. S., Bayramyan, M., Haworth, I. S., Myszka, D. G., and Laird-Offringa, I. A. (2002), "Complex role of the $\alpha_2\alpha_3$ loop in the interaction of U1A with U1 hairpin II RNA." *J. Biol. Chem.* 277, 33276-33274.
- P128. Day, Y. S. N., Baird, C. L., Rich, R. L., and Myszka, D. G. (2002), "Direct comparison of equilibrium, thermodynamic, and kinetic rate constants determined by surface- and solution-based biophysical methods", *Protein Sci.* 11, 1017-1025.
- P129. Myszka, D. G., "Biomolecular Interaction Analysis", Rennselear Polytechnical Institute, 2001.
- P130. Homola, J., Yee, S. S., and Myszka DG (2002), "Surface plasmon resonance biosensors", *Optical Biosensors: Present and Future* (Ed. Frances Ligler) pp. 207-251.
- P131. Myszka, D. G., "Advanced Applications of SPR Biosensors", Optical Biosensors, Prague, Czech Republic, 2001.
- P132. Cannon, M. J., Myszka, D. G., Bagnato, J. D., Alpers, D. H., West, F. G., and Grissom, C. B., (2002) "Equilibrium and kinetic analyses of the interactions between vitamin B₁₂ binding proteins and cobalamins by surface plasmon resonance", *Anal. Biochem.* 305, 1-9.
- P133. Myszka, D. G., "Improving Biosensor Analysis", *Biosensor Focus Day*, Eindhoven, Holland, 2001.
- P134. Baird, C. L. and Myszka, D. G. (2001) "Current and emerging optical biosensors", *J. Mol. Recog.* 14, 261-268.
- P135. Myszka, D. G., "Implementing Biosensors in Drug Discovery", SPR Biosensor Analysis, Stevenage, England, 2001.
- P136. Rich, R. L., Day, Y. S. N., Morton, T. A., and Myszka, D. G., (2001) "High-resolution and high-throughput protocols for measuring drug/human serum albumin interactions using BIACORE", *Anal. Biochem.* 296, 197-207.

- P137. Rich, R. L and Myszka, D. G., (2001) "Survey of the year 2000 commercial optical biosensor literature", *J. Mol. Recog.* 14, 273-294.
- P138. Myszka, D. G., "Kinetics, Thermodynamics, and Affinity from SPR Biosensors", *Global Biosensor Meeting*, Puerto Rico, 2001.
- P139. Myszka, D. G., "Experimental Design for Small Molecular Analysis" *Biosensor Workshop*, Fulda, Germany, 2001.
- P140. Rich, R. L. and Myszka, D. G., (2001) "Recent developments in SPR biosensor technology: Application of BIACORE J, *Chemical Sensors 21*, 14-23.
- P141. Myszka, D. G., "Modeling of Optical Biosensor Data", *Biosensor Workshop*, Research Triangle Park, NC, 2001.

Publications from Collaborations between Utah and CFDR

- P142. Jenkins' J. W., Prabhakarpanid, B., Myszka, D. and Sundaram, S. "Reliable Molecular Interaction Analysis Using Array-Based, Fluidics-Enabled Protein Biosensors" *Proc. Labautomation 2003*, CA, 2003.
- P143. Jenkins' J. W., Prabhakarpanid, B., Myszka, D. and Sundaram, S. "Transport-Resolved Simulation-based Molecular Interaction Analysis from a Fluidic Biosensors" In Preparation

University of California at Santa Barbara Publications and Presentations

- P144. Bown, M.R, C. D. Meinhart 2006 AC electroosmotic flow in a DNA concentrator. *Micro and Nanofluidics*, Published online 20 May 2006.
- P145. M. Sigurdson, D. Wang, and C.D. Meinhart.2005 Electrothermal Stirring for Heterogeneous Immunoassay. *Lab on a Chip*. volume 5, issue 12
- P146. L. Zhu, L. Petzold, D. Tretheway & C. D. Meinhart 2005 Simulation of fluid slip at hydrophobic microchannel walls by the Lattice Boltzmann Method, *J. Computational Physics*, Vol. 202, No. 1, Jan. 2005, pp. 181-195.
- P147. Dazhi Wang, Marin Sigurdson & Carl Meinhart 2005 Experimental Analysis of particle and Fluid Motion in AC Electrokinetics, *Exp. in Fluids.*, Vol. 38, No. 1, pp. 1-10.
- P148. F. Bottausci, C. Cardonne, C. Meinhart & I. Mezic 2004 An Actively Controlled Micromixer: 3-D Aspect Micromixer, Microfluidics History, Theory and Applications, Will Zimmerman, Ed., *International Centre for Mechanical Sciences*, Springer-Verlag.
- P149. Dazhi Wang, Marin Sigurdson, Carl Meinhart 2004 Application of Micro PIV to AC Electrokinetic Flows, *Euro-PIV Book*, Springer-Verlag.
- P150. S. T. Wereley & C. D. Meinhart 2004 Electrokinetics in Microdevices, In Complex Systems Science in BioMedicine , eds. Deisboeck, Kresh, Kepler, Kluwer Academic – Plenum Publishers, Boston,.
- P151. F. Bottausci, I. Mezić, C. D. Meinhart & C. Cardonne 2004. Mixing in the shear superposition micromixer: three-dimensional analysis. *Phil. Trans. of the Royal*

- Society of London Series A-Math. Phys. and Eng. Sci.* 362 (1818): 1001-1018 May 15 2004.
- P152. D. Tretheway & C. D. Meinhart 2004. A generating mechanism for fluids slip in a hydrophobic microchannel. *Phys. Fluids Vol. 16, No. 5 pp 1509-1515, May 2004.*
- P153. C. D. Meinhart, D. Wang & K. Turner 2003 Measurement of Ac Electrokinetic Flows. *J. Biomedical Microdevices.* 5(2), 139-145, June.
- P154. C. D. Meinhart & S. T. Wereley 2002. Micron Resolution Particle Image Velocimetry, in Diagnostic Techniques for Microfluidics, Kenny Breuer Ed., Springer-Verlag, Berlin.
- P155. D.C. Tretheway & C. D. Meinhart 2002. Fluid slip near hydrophobic microchannel walls, *Phys. of Fluids*, 14 (3), L9-L12.
- P156. S. W. Stone, C. D. Meinhart, & S. T. Wereley 2002. A Microfluidic-based Nanoscope. In Press *Exp in Fluids*.
- P157. S. T. Wereley, L. Gui & C. D. Meinhart. 2001. Advanced algorithms for microscale particle image velocimetry, *In Press AIAA Journal*.
- P158. D.C. Tretheway and C.D. Meinhart, 2002 Examination of the Slip Boundary Condition by μ -PIV and Lattice Boltzmann Simulations, ASME-IMECE'02, New Orleans, LA, Nov. 17-22.
- P159. C.D. Meinhart, D. Wang & Kimberly Turner, 2002 Measurement of ac electrokinetic flows, *Proceedings of the 10th International Symposium on Flow Visualization*, Kyoto, Japan, Aug. 26 – 29.
- P160. D.C. Tretheway & C.D. Meinhart, 2002 PIV Measurement of Slip Flow in Microchannels, *Proceedings of the 11th International Symposium on Applications of Laser Techniques to Fluid Mechanics*, Lisbon, Portugal.
- P161. D.C. Tretheway & C. D. Meinhart 2001 Velocity measurements of flow over hydrophobic microchannel walls. *ASME – IMECE'01 MEMS Symposium*, New York, NY, Nov. 11–16.
- P162. M. Sigurdson, C. D. Meinhart, K. Turner, L. Coldren, D. Cohen, T. Stultz, & N. Slack 2001 An integrated SGDBR laser-based biosensor, *Proceedings of μ -TAS 2001*, Monterrey, CA.
- P163. C. D. Meinhart, D. Wang 2001 Accurate Measurement of Dielectrophoretic (DEP) Mobility of particles and macromolecules, *Proceedings of μ -TAS 2001*, Monterrey, CA.
- P164. D. Tretheway & C. D. Meinhart 2001 Micron-resolution PIV near a hydrophobic microchannel wall, . *Proceedings of the Forth International Workshop on Particle Image Velocimetry*, Göttingen, Germany, Sept. 17 – 19.
- P165. S. Stone, C. D. Meinhart & S. T. Wereley 2001 Using μ -PIV to probe wall shapes with nanoscope resolution. *Proceedings of the Forth International Workshop on Particle Image Velocimetry*, Göttingen, Germany, Sept. 17 – 19.
- P166. S. T. Wereley, C. D. Meinhart, S. Stone, V. Hohreiter & Jacob Chung 2001 A Microfluidic MEMS Characterization Toolbox. *Proceedings of the International MEMS Workshop*, Singapore, Hong Kong.

Publications from Collaborations between Sandia National Labs and Johns Hopkins University

- P167. Knio, R. Ghanem, A. Matta, H. Najm, B. Debusschere, and O. Le Maître.
Quantitative Uncertainty Assessment and Numerical Simulation of Micro-Fluid Systems. Final technical report for F30602-00-2-0612, AFRL-IF-RS-TR-2005-143, ADA 434355.
- P168. Debusschere, B., Najm, H.N., Matta, A., Knio, O.M., Ghanem, R.G. and Le Maître, O.P., "Protein Labeling Reactions in Electrochemical Microchannel Flow: Numerical Simulation and Uncertainty Propagation"; *Physics of Fluids*, Vol. 15, pp. 2238-2250 (2003); *Virtual Journal of Biological Physics Research*, Vol. 6, July 2003.

6.0 REFERENCES

(For the entire text)

1. Attard, P., *Images of nanobubbles on hydrophobic surfaces and their interactions*. Phys. Rev. Lett., 2001. **87**.
2. Ottino, J.M., *The Kinematics of Mixing* ed. C. Cambridge University Press, UK. 1989.
3. N. Schwesinger, T.F., and H. Wurmus, J. Micromech. Microeng. , 1996. **6**: p. 99-102
4. A. D. Stroock, S.K.D., G. M. Whitesides, A. Ajdari, Anal. Chem., 2002. **74**: p. 5306-5312
5. A. D. Stroock, M.W., D. T. Chiu, W. T. S. Huck, P.J.A. Kenis, R. Ismagilov, G. M. Whitesides, Phys. Rev. Lett. , 2000. **84**: p. 3314-3317
6. Ajdari, A., Phys. Rev. Lett., 1995. **75**: p. 755-758.
7. T.J. Johnson, T.J.D.R., L.E. Locascio, Anal. Chem. , 2002. **74**: p. 45-51.
8. M. H. Oddy, J.G.S., J. C. Mikkelsen, Anal. Chem., 2001. **73**: p. 5822-5832.
9. A. Rida, M.A.M.G., Anal. Chem. , 2004. **76**: p. 6239-6246.
10. J. Evans, D.L., and A. Pisano. in *IEEE-MEMS 97 Conference*. 1997. Nagoya, Japan.
11. P. Garstecki, M.A.F., G. M. Whitesides, Applied Physics Letters, 2005. **86**: p. 1-3.
12. G. G. Yaralioglu, I.O.W., T. C. Marentis, B. T. Khuri-Yakub, Anal. Chem., 2004. **76**: p. 3694-3698
13. Breuer, M.J.K.a.K.S., Physics of Fluids, 2004. **16**: p. 78-81.
14. Locascio, L.E., Analytical and Bioanalytical Chemistry, 2004. **379**: p. 325-327.
15. A. Castellanos, A.R., A. Gonzalez, N. G. Green, H. Morgan, J. Phys. D: Appl. Phys., 2003. **36**: p. 2584-2597.
16. Ramos, A., et al., *AC ELECTROKINETICS - A REVIEW OF FORCES IN MICROELECTRODE STRUCTURES [Review]*. Journal of Physics D-Applied Physics, 1998. **31**(18): p. 2338-2353.
17. Stratton, J.A., *Electromagnetic Theory*. 1941, New York, NY: McGraw-Hill.
18. Anonymous, *CFD-ACE+ Theory Manual*. 2003: CFD Research Corporation.
19. Pohl, H.A., *Dielectrophoresis*. 1978: Cambridge University Press
20. Masuda, S., M. Washizu, and I. Kawabata, *MOVEMENT OF BLOOD CELLS IN LIQUID BY NONUNIFORM TRAVELING FIELD*. IEEE Transactions on Industry Applications, 1988. **24**(2): p. 217.
21. Pethig, R., *Dielectrophoresis: Using Inhomogeneous AC Electrical Fields to Separate and Manipulate Cells*. Critical Reviews in Biotechnology, 1996. **16**(4): p. 331.
22. Voldman, J., et al., *Design and analysis of extruded quadrupolar dielectrophoretic traps*. Journal of Electrostatics, 2003. **57**(1): p. 69.
23. Bhatia, S.N., et al., *Electro-optical platform for the manipulation of live cells*. Langmuir, 2003. **19**(5): p. 1532.
24. Fiedler, S., et al., *Dielectrophoretic sorting of particles and cells in a microsystem*. Analytical Chemistry, 1998. **70**(9): p. 1909.

25. Clague, D.S. and E.K. Wheeler, *Dielectrophoretic manipulation of macromolecules: The electric field*. Physical Review E. Statistical Physics, Plasmas, Fluids, and Related Interdisciplinary Topics, 2001. **64**(2 II): p. 26605-1.
26. Green, N.G., A. Ramos, and H. Morgan, *Numerical solution of the dielectrophoretic and travelling wave forces for interdigitated electrode arrays using the finite element method*. Journal of Electrostatics, 2002. **56**(2): p. 235-254.
27. Feng, J.J., et al. *Numerical and analytical studies of ac electric field in dielectrophoretic electrode arrays*. 2002. San Juan, Puerto Rico: Computational Publications, Cambridge, MA 02139, United States.
28. Jones, T.B., *Basic Theory of Dielectrophoresis and Electrorotation*. IEEE Engineering in Medicine and Biology Magazine, 2003. **22**(6): p. 33-42.
29. Wang, X.B., et al., *Unified theory of dielectrophoresis and travelling wave dielectrophoresis*. Journal of Physics D: Applied Physics, 1994. **27**(7): p. 1571-1574.
30. V. Sikavitsas, J.N., T. Mountziaris, *Biotechnol. Prog.*, 2002. **18**: p. 885-897.
31. J. Giddings, E.K., C. Russel, M. Myers, *J. Phys Chem.*, 1968. **72**: p. 4397-4408.
32. M. Yarmush, D.P., D. Yarmush, *Mol. Immun.*, 1996. **33**: p. 1203-1214.
33. Meinhart, D.T.C.D., *A generating mechanism for fluids slip in a hydrophobic microchannel*. Phys. Fluids, 2004. **16**(5): p. 1509-1515.
34. Zhu, Y.G., S., *Rate-dependent slip of Newtonian fluids at smooth surfaces*. Phys. Rev. Lett. , 2001. **87**.
35. D.E. Yates, S.L., T. W. Healy, *Site-binding model of electrical double layer at the oxide/water interface*. Journal of the Chemical Society, Faraday transaction 1, 1974. **74**: p. 1807-1818.
36. Krishnamoorthy, S., et al. *Analysis of physico-chemical processes in an amperometric oxygen biosensor*. in *Computational Publications*. 2002. San Juan, Puerto Rico.
37. Bedekar, A.S., et al., *System-level simulation of flow-induced dispersion in lab-on-a-chip systems*. IEEE Transactions on Computer-Aided Design of Integrated Circuits and Systems, 2006. **25**(2): p. 294-304.
38. J. Jenkins, S.S., J. Hickman, K. Lenghaus., *Non-Linear Extraction of Kinetic Constants from Experimental Data using Multiphysics Simulations*. Anal Biochem., 2004. **331**: p. 207-215.
39. Lu, C., A. Nadarajah, K. Chittur, *A Comprehensive Model for Protein Adsorption to Surfaces*. J. Coll. Int. Sci., 1995. **168**: p. 152-161.
40. Krishnamoorthy, S., et al., *Simulation-Based Analysis of Fluid Flow and Electrokinetic Phenomena in Microfluidic Devices*. JALA - Journal of the Association for Laboratory Automation, 2006. **11**(3): p. 118.
41. Stenberg, M. and H. Nygren, *Kinetics of antigen-antibody reactions at solid-liquid interfaces*. Journal of Immunological Methods, 1988. **113**: p. 3-15.
42. Northrup, M.A., K.F. Jensen, and D.J. Harrison, eds. *Seventh International Conference on Micro Total Analysis Systems*. 2003. Squaw Valley, CA: Transducers Research Foundation.
43. Bousse, L., et al., *Electrokinetically controlled microfluidic analysis systems [Review]*. Annual Review of Biophysics & Biomolecular Structure, 2000. **29**: p. 155-181.

44. Koh, C.G., et al., *Integrating polymerase chain reaction, valving, and electrophoresis in a plastic device for bacterial detection*. Analytical Chemistry, 2003. **75**(17): p. 4591-4598.
45. Thormann, W., et al., *Advances of capillary electrophoresis in clinical and forensic analysis (1999-2000) [Review]*. Electrophoresis, 2001. **22**(19): p. 4216-4243.
46. Miles, R., et al., *Dielectrophoretic manipulation of particles for use in microfluidic devices*. Proceedings of the ASME International Mechanical Engineering Congress and Exposition, Nashville, TN, 1999. **MEMS-1**.
47. Gascoyne, P.R.C. and J. Vykoukal, *Particle separation by dielectrophoresis [Review]*. Electrophoresis, 2002. **23**(13): p. 1973-1983.
48. Wong, P.K., et al., *Electrokinetics in Micro Devices for Biotechnology Applications*. IEEE / ASME Transactions on Mechatronics, 2004. **9**(2): p. 366-376.
49. Bazant, M.Z. and T.M. Squires, *Induced-Charge Electrokinetic Phenomena: Theory and Microfluidic Applications*. Physical Review Letters, 2004. **92**(6): p. 066101.
50. Ramos, A., et al., *Manipulation of bio-particles in microelectrode structures by means of non-uniform AC electric fields*. Proceedings of the ASME International Mechanical Engineering Congress and Exposition, New Orleans, LA, 2002.
51. Perch-Nielsen, I.R., N.G. Green, and A. Wolff, *Numerical simulation of travelling wave induced electrothermal fluid flow*. Journal of Applied Physics D: Applied Physics, 2004. **37**(Jul 2004): p. 2323-2330.
52. Wang, D., M. Sigurdson, and C. Meinhart, *Experimental analysis of particle and fluid motion in ac electrokinetics*. Experiments in Fluids, 2005. **38**(1).
53. Wang, D.Z., *Investigation of AC Electrokinetics using Micro-PIV (Doctoral Thesis; UC Santa Barbara)*. 2004.
54. Lide, D.R., *CRC Handbook of Chemistry and Physics, 81st Ed.* 2000, New York: CRC Press.
55. Myszka, D.G., et al., *Extending the Range of Rate Constants Available from Biacore - Interpreting Mass Transport-Influenced Binding Data*. Biophysical Journal, 1998. **75**(2): p. 583-594.
56. R. T. Kurnik, T.D.B., U. Nguyen, A. J. Ricco, and S. J. Williams, *Use of Floating Electrodes in Transient Isotachophoresis to Increase the Sensitivity of Detection*. Lab Chip, 2003. **3**: p. 86-92.
57. H. Tian, L.C., Y. Tan, S. Williams, L. Chen, T. Matray, A. Chenna, S. Moore, V. Hernandez, V. Xiao, M. Tang, and S. Singh, *Multiplex mRNA Assay Using Electrophoretic Tags for High-Throughput Gene Expression Analysis*. Nucleic Acids Research, 2004. **32**: p. e126.
58. DG., M., *Analysis of small-molecule interactions using Biacore S51 technology*. Anal Biochem., 2004. **329**(2): p. 316-23.
59. al., C.e., *Comparative analyses of a small molecule/enzyme interaction by multiple users of Biacore technology*. Anal Biochem., 2004. **330**(1): p. 98-113.
60. al., K.e., *Kinetic analysis of a high-affinity antibody/antigen interaction performed by multiple Biacore users*. Anal Biochem., 2006. **352**(2): p. 208-21.
61. al., P.e., *Comparative analysis of ten small molecules binding to carbonic anhydrase II by different investigators using Biacore technology*. Anal. Biochem., 2006.

62. Navratilova et al., . *Thermodynamic analysis of enzyme/inhibitor interactions by multiple users of Biacore technology*. Anal Biochem., 2006.
63. al., S.e., *Screening antibody-antigen interactions in parallel using Biacore A100*. Anal Biochem., 2006. **353**(2): p. 181-90.
64. Karlsson R, K.P., Nordin H, Pol E, Myszka DG., *Analyzing a kinetic titration series using affinity biosensors*. Anal Biochem. , 2006. **349**(1): p. 136-47.
65. al., N.e., *Measuring long association phases using Biacore*. Anal Biochem., 2005. **344**(2): p. 295-7.
66. Hoburg, J.F., and Melcher, J. R., *Internal electrohydrodynamic instability and mixing of fluids with orthogonal field and conductivity gradients*. J. Fluid Mech. , 1976. **73**: p. 333.
67. Baygents, J., and Baldessari, F, *Electrohydrodynamic instability in a thin fluid layer with an electrical conductivity gradient*. Phys. Fluids, 1998. **10**(1): p. 301-311.
68. Chen. C.-H., a.S., J. G. *Electrokinetic instability in high concentration gradient microflows*. in *Proceedings of IMECE-2002*. 2002.
69. Chen, C.-H., Lin, H., Lele, S. K., and Santiago, J. G., *Convective and absolute electrokinetic instability with conductivity gradients*. J. Fluid Mech., 2004.
70. Lin, H., Storey, B. D., Oddy, M. H., Chen, C.-H., and Santiago, J. G., *Instability of electrokinetic microchannel flows with conductivity gradients*. Phys. Fluids 2004. **16**(6): p. 1922-1935.
71. Melcher, J.R., and Taylor, G. I., *Electrohydrodynamics: a review of the role of interfacial stresses*. Annu. Rev. Fluid. Mech., 1969. **1**: p. 111-146.
72. Storey, B.D., Tilley, B. S., Lin, H., and Santiago, J. G., *Electrokinetic instabilities in thin microchannels*. Phys. Fluids, 2004.
73. Probstein, R.F., *Physicochemical Hydrodynamics*, ed. J.W. Sons. 1994, New York.
74. Liu, S., and Masliyah, S. , *Single fluid flow in porous media*. Chem. Eng. Comm., 1996: p. 148-150, 653-732.
75. Oddy, M.H., Santiago, J.G. and Mikkelsen, J.C., *Electrokinetic instability micromixing*. Anal. Chem., 2001. **73**: p. 5822-5832.
76. Oddy, M.H.M., J. C.; Santiago, J. G., *Electrokinetic Instability Micromixing*. Analytical Chemistry, 2001. **73**: p. 5822-5832.
77. Pit, R.H., H.;Leger, L., *Direct experimental evidence of slip in hexadecane: solid interfaces*. Phys. Rev. Lett., 2000. **85**.
78. Boone, T.D., H.H. Hooper, and D.S. Soane. *Integrated Chemical Analysis on Plastic Microfluidic Devices*. in *Solid-State Sensors and Actuators Workshop*. 1998. Hilton Head, SC: Transducers Research Foundation.
79. Herr, A.E., *Isoelectric Focusing for Multi-dimensional Separations in Microfluidic Devices*. 2002, Stanford University.
80. Herr, A.E., J.I. Molho, K.A. Drouvalakis, J.C. Mikkelsen, P.J. Utz, J.G. Santiago, and T.W. Kenny *On-Chip Coupling of Isoelectric Focusing and Free Solution Electrophoresis for Multi-Dimensional Separations*. Analytical Chemistry, 75. **5**: p. 1180-1187.
81. Herr, A.E., J.I. Molho, K.A. Drouvalakis, J.C. Mikkelsen, P.J. Utz, J.G. Santiago, and T.W. Kenny *On-Chip Coupling of Isoelectric Focusing and Free Solution*

- Electrophoresis for Multi-Dimensional Separations*. Analytical Chemistry, 2003. **5**(75): p. 1180-1187.
82. Jung, B., R. Bharadwaj, and J.G. Santiago, *Thousand-Fold Signal Increase using Field Amplified Sample Stacking for On-Chip Electrophoresis*. Electrophoresis, 2003. **24**(21).
 83. Bharadwaj, R.a.J.G.S., *Dynamics of Field Amplified Sample Stacking*. Journal of Fluid Mechanics, 2005. **543**: p. 57-92.
 84. Jung, B., Zhu, Y., and J.G. Santiago, *Detection of 100 attomolar Fluorophores Using a High Sensitivity On-Chip CE System and Transient Isotachophoresis*. submitted to Analytical Chemistry, 2006.
 85. Landers, J.P., *Handbook of Capillary Electrophoresis*. Second Edition ed. 1997, Boca Raton: CRC Press. 894.
 86. Jung, B., Bharadwaj, R., Santiago, J.G., *On-Chip Million-Fold Sample Stacking Using Single-Interface Isotachophoresis*. Analytical Chemistry, 2006. **78**(7): p. 2319-2327.
 87. O. Knio, R.G., A. Matta, H. Najm, B. Debusschere, and O. Le Maître, *Quantitative Uncertainty Assessment and Numerical Simulation of Micro-Fluid Systems*. Final technical report for F30602-00-2-0612, AFRL-IF-RS-TR-2005-143, ADA 434355. .
 88. Debusschere, B., Najm, H.N., Matta, A., Knio, O.M., Ghanem, R.G. and Le Maître, O.P., *Protein Labeling Reactions in Electrochemical Microchannel Flow: Numerical Simulation and Uncertainty Propagation*. Physics of Fluids. , 2003. **15**: p. 2238-2250.